

FIRST DIRECT DOUBLE-BETA DECAY Q -VALUE MEASUREMENT OF THE
NEUTRINOLESS DOUBLE-BETA DECAY CANDIDATE ^{82}Se AND DEVELOPMENT
OF A HIGH-PRECISION MAGNETOMETER

By

David Louis Lincoln

A DISSERTATION

Submitted to
Michigan State University
in partial fulfillment of the requirements
for the degree of

Physics – Doctor of Philosophy

2013

ABSTRACT

FIRST DIRECT DOUBLE-BETA DECAY Q -VALUE MEASUREMENT OF THE NEUTRINOLESS DOUBLE-BETA DECAY CANDIDATE ^{82}Se AND DEVELOPMENT OF A HIGH-PRECISION MAGNETOMETER

By

David Louis Lincoln

The results of recent neutrino oscillation experiments indicate that the mass of the neutrino is nonzero. The mass hierarchy and the absolute mass scale of the neutrino, however, are unknown. Furthermore, the nature of the neutrino is also unknown; is it a Dirac or Majorana particle, i.e. is the neutrino its own antiparticle? If experiments succeed in observing neutrinoless double-beta decay, there would be evidence that the neutrino is a Majorana particle and that conservation of total lepton number is violated – a situation forbidden by the Standard Model of particle physics. In support of understanding the nature of the neutrino, the first direct double-beta decay Q -value measurement of the neutrinoless double-beta decay candidate ^{82}Se was performed [D. L. Lincoln *et al.*, Physical Review Letters **110**, 012501 (2013)]. The measurement was carried out using Penning trap mass spectrometry, which has proven to be the most precise and accurate method for determining atomic masses and therefore, Q -values. The high-precision measurement resulted in a Q -value with nearly an order of magnitude improvement in precision over the literature value. This result is important for the theoretical interpretations of the observations of current and future double-beta decay studies. It is also important for the design of future and next-generation double-beta decay experiments, such as SuperNEMO, which is planned to observe 100 - 200 kg of ^{82}Se for five years.

The high-precision measurement was performed at the Low-Energy Beam and Ion Trap

(LEBIT) facility located at the National Superconducting Cyclotron Laboratory (NSCL). The LEBIT facility was the first Penning trap mass spectrometry facility to utilize rare isotope beams produced via fast fragmentation and has measured nearly 40 rare isotopes since its commissioning in 2005. To further improve the LEBIT facility's performance, technical improvements to the system are being implemented. As part of this work, to increase the precision of measurements and to maximize the use of beam time, a high-precision magnetometer was developed. The magnetometer will monitor drifts in the LEBIT facility's 9.4 T superconducting magnet to a relative precision on the order of 1 part in 10^8 . This will eliminate the need to perform reference measurements during an experiment, thus expanding the LEBIT facility's measurement capabilities and scientific output.

ACKNOWLEDGMENTS

I would first like to thank my advisor, Georg Bollen, for whose guidance I am deeply indebted. I am grateful for the amount of time Georg spent with me brainstorming innovative solutions throughout the design phase and troubleshooting issues during the testing phase of the magnetometer. Georg's persistence, determination, and ingenuity helped me recognize solutions to problems encountered throughout my tutelage as a graduate research assistant. I am also greatly indebted to Matthew Redshaw, the postdoctoral fellow I worked very closely with throughout both the Q -value measurement and the development of the magnetometer. Matt's expertise, hard work, and motivation helped pave the way for my success as a graduate student. I would also like to express my gratitude to my committee members Prof. Dave Morrissey, Prof. Bhanu Mahanti, Prof. Hendrik Schatz, and Prof. Edward Brown as their willingness to provide guidance has been deeply appreciated.

I would also like to thank Stefan Schwarz, a staff scientist of the LEBIT group who taught me how to troubleshoot and repair electronic devices and scientific instrumentation, as well as how to design electronic circuits of my own. I must also thank Ryan Ringle, another staff scientist of the LEBIT group, for all his help and support in not only understanding and maintaining the LEBIT facility's control system and associated electronics, but also for his leadership in relocating and recommissioning the LEBIT facility. I also worked with the previous post-doctoral fellows, Rafael Ferrer and Maxime Brodeur, and would like to express my thanks to them for their help and support. I'd also like to thank the previous graduate students of the LEBIT group that I worked closely with, Josh Savory and Ania Kwiatkowski, as well as the current LEBIT graduate students Scott Bustabad, Sam Novario, and Adrian Valverde for their help and support. A big thanks goes out to the three REU students,

Anne Benjamin, Robert Baker, and Almira Sonea, who were instrumental in developing, fabricating, and testing components utilized by the magnetometer.

I greatly appreciate the time and effort put into designing and manufacturing the magnetometer by the NSCL's Mechanical Engineering department and machine shop. John Puro, Don Lawton, Jack Otterson, and especially Scott Stephens were instrumental during the design phase. Jay Pline helped coordinate the fabrication of the magnetometer and also helped machine ancillary parts as needed. Finally, a big thanks goes to Keith Leslie who fabricated all of the magnetometer electrodes to the tolerances required by the MiniTrap to achieve the required precision.

Last but not least, I am greatly indebted to my family and friends. I am grateful for the unconditional love and support from my parents, Louis and Diane Lincoln, who always allowed me to follow my own path and for painstakingly listening to me expound my ideas concerning science, technology, philosophy, and the meaning of life. I'd like to give my heartfelt thanks to my wife, Ngoc Nguyen and her parents, Chin and Duc Nguyen, and her sister Nga Nguyen for their acceptance, love, and support over the years. A big thanks to my brother, Matt Lincoln, and sister-in-law, Shireen Lincoln, for being great role models and providing me with an example to live up to. Finally, I'd like to thank some of my closest friends, the McIntire's, Colin Bamford, Mike Brayman, Craig Karlson, Alex Gauthier, Shaun Wooden, Matt Cenci, and Jeff Herzog for encouraging me along my journey. A special thanks goes to Patrick Millard, Eric Lawrence, and Pat Brown who constantly remind me to live life to the fullest and appreciate everything life has to offer. I assure all of you that I greatly appreciate your companionship over the years and I am looking forward to many more great times together. I hope this work makes all of you proud.

TABLE OF CONTENTS

LIST OF TABLES	viii
LIST OF FIGURES	ix
Chapter 1 Introduction	1
1.1 Neutrinoless Double-Beta Decay	2
1.2 PTMS at the NSCL and Enhancements	4
Chapter 2 LEBIT Facility	5
2.1 LEBIT I - First Experiments with Rare Isotopes	6
2.2 LEBIT II - Features of Relocated Facility	7
2.3 Basic Components of the LEBIT Facility	9
2.3.1 Ion Sources	10
2.3.2 Cooler and Buncher	13
2.3.3 9.4 T Penning Trap Mass Spectrometer	14
2.4 LEBIT II - Techniques Used at the LEBIT Facility	15
2.4.1 Ion Preparation and Non-Isobaric Beam Purification	15
2.4.2 Penning Trap Mass Spectrometry	17
2.4.3 Reference Measurements	21
Chapter 3 First Direct Double-Beta Decay Q-value Measurement of ^{82}Se	25
3.1 Motivation for Determining the ^{82}Se Double-Beta Decay Q -value	25
3.2 Experimental Setup	28
3.3 Measurements	30
3.4 Data Analysis	32
3.5 Discussion of Results and Conclusion	34
Chapter 4 Development of a High-Precision Magnetometer for the LEBIT Facility	35
4.1 Motivation for a High-Precision Magnetometer	36
4.2 Magnetometer Concept and Design Requirements	38
4.3 Technical Development of the Magnetometer	39
4.3.1 Fourier Transform – Ion Cyclotron Resonance (FT-ICR)	40
4.3.2 Ion Production	45
4.3.3 Testing Ion Production and FT-ICR Techniques in the LEBIT Penning Trap	47
4.4 MiniTrap Magnetometer Design and Fabrication	54
4.4.1 Trap Geometry and Factors Affecting Trap Dimensions	54

4.4.2	Determination of Trap Dimensions	60
4.4.3	Design and Fabrication of the MiniTrap	65
4.5	Testing the MiniTrap Magnetometer	71
4.5.1	Detection of Ion Motion via FT-ICR	73
4.5.1.1	Magnetron Motion	73
4.5.1.2	Reduced Cyclotron Motion	76
4.5.2	True Cyclotron Frequency Determination	83
4.5.2.1	Quadrupole Pickup Detection Method	84
4.5.2.2	Precision of the MiniTrap Magnetometer	88
4.5.2.3	Tracking the B Field Using the True Cyclotron Frequency	92
4.5.2.4	Improving the Precision of the MiniTrap	95
4.5.3	Summary of Results	97
Chapter 5	Summary and Outlook	99
APPENDICES	102
Appendix A:	MiniTrap Electronics	103
Appendix B:	MiniTrap Control System	110
BIBLIOGRAPHY	115

LIST OF TABLES

Table 3.1	Average cyclotron frequency ratios $R_{run} = \nu_c^{int}(^{82}\text{Kr}^+)/\nu_c(^{82}\text{Se}^+)$ with their statistical errors as obtained in four separate runs with N frequency ratio measurements performed in each run. Also given is the final weighted average R_{LEBIT} with its statistical and final uncertainty and the ratio calculated using the mass values from AME2003 [75].	33
Table 4.1	Dimensionless trap parameter ratios and the corresponding physical trap parameters (with $\rho_o = 2.5$ mm) for the optimized (minimized C_4 and C_6) open-ended, electrically compensated, cylindrical trap as determined through Mathematica analysis of SIMION potentials. . .	64
Table 4.2	Electrode voltages and the resulting C_n coefficients for the optimized trap using the dimensions given in Table 4.1. Note that the endcap and ring voltages are scalable (see text).	64
Table 4.3	Optimal excitation parameters identified by a 3-dimensional scan of ρ_- for a range of endcap-to-ring voltage ratios for different cyclotron excitation amplitudes. The magnetron and cyclotron excitation times and frequencies were held constant at 10.25 kHz for ~ 1.5 ms and 5.6428 MHz for ~ 100 μ s, respectively, within a potential well of 7.735 V. *A 10 dB attenuator was used to attenuate the cyclotron excitation.	86
Table B.1	An example of a script string used in the Script tab of the MTCS to control a continuous monitoring process of ten thousand cyclotron frequency measurements of $f_c(\text{H}_3\text{O}^+)$	113

LIST OF FIGURES

Figure 2.1	Basic layout of the rare isotope production technique via projectile fragmentation at the National Superconducting Cyclotron Laboratory’s Coupled Cyclotron Facility. “For interpretation of the references to color in this and all other figures, the reader is referred to the electronic version of this dissertation.”	6
Figure 2.2	Schematic layout of the upgraded beam stopping facility, low-energy area, and reaccelerator.	8
Figure 2.3	Layout of the upgraded LEBIT facility.	9
Figure 2.4	Components of the upgraded beam stopping facility showing (a) a photo of the next-generation linear gas cell, (b) a schematic of the upgraded ion guides, and (c) a photo of the cycstopper being assembled.	11
Figure 2.5	The plasma test ion source assembly shown removed from the vacuum chamber.	12
Figure 2.6	Photos of (a) the cooler and (b) the buncher before insertion into the beam line.	13
Figure 2.7	Photos of (a) LEBIT’s hyperbolic Penning trap and (b) the 9.4 T superconducting magnet.	14
Figure 2.8	Schematic diagram of ion preparation, non-isobaric purification, and ion detection equipment at the LEBIT facility.	15
Figure 2.9	Schematic of a Penning trap. The hyperbolic electrode structure of the Penning trap is used to create a quadrupole potential by applying a voltage, V_o , across the endcap and ring electrodes in a strong magnetic field, B . The size of the trap is characterized by the trap length, z_o , and the trap radius, ρ_o	17

Figure 2.10	Illustration of the eigenmotions executed in a Penning trap in a strong magnetic field: axial oscillations in the direction parallel to the magnetic field, the slower radial magnetron motion due to the $\mathbf{E} \times \mathbf{B}$ drift, and the faster radial reduced cyclotron motion.	19
Figure 2.11	A typical time-of-flight cyclotron resonance curve. A fit of the theoretical line shape to the data is represented by the solid line (red). .	21
Figure 2.12	(a) Magnetic field drift of LEBIT's 9.4 T superconducting magnet during rare isotope measurements of ^{37}Ca and ^{38}Ca . The solid line (red) represents the atmospheric pressure data from a local weather station as reported by Weather Underground (Wunder) and the dashed line represents the pressure data recorded from a high-precision barometer (Setra) located at the NSCL. Note that $(\Delta B/B)/dp = 4.5 \times 10^{-8} \text{ mbar}^{-1}$. (b) Residual non-linear drift after stabilizing the pressure of the liquid helium bath of the superconducting magnet and subtracting out the linear magnetic field decay. (Note the change in scales between the two graphs.)	23
Figure 2.13	Cartoon showing how reference cyclotron frequency measurements (blue dots) are used to interpolate the strength of the magnetic field during a rare isotope cyclotron frequency measurement (red dots). .	23
Figure 3.1	Example of a time-of-flight cyclotron resonance curve for $^{82}\text{Se}^+$. An excitation time of $T_{RF} = 750 \text{ ms}$ was used to obtain a resolving power of 2×10^6 . The results of fitting the theoretical line shape to the data is represented by the solid line (red).	30
Figure 3.2	Difference between the cyclotron frequency ratio of $^{82}\text{Kr}^+$ to $^{82}\text{Se}^+$ and the ratio obtained from literature mass data [75]. The solid lines indicate the weighted average and the 1σ statistical uncertainty band.	31
Figure 4.1	Cartoon showing how two reference cyclotron frequency measurements (blue dots) are used to calibrate a magnetometer that can track short-term fluctuations in the magnetic field allowing for either a longer rare isotope frequency measurement time, or as shown, increase the number of rare isotope frequency measurements (red dots).	37
Figure 4.2	Location of the magnetometer depicted in an image of the Penning trap along with injection and ejection optics shown removed from the bore of LEBIT's solenoidal 9.4 T superconducting magnet.	39

Figure 4.3	Schematic representation of the basic FT-ICR technique where ions are driven by excitation electrodes (white) and induce an image current in the detection electrodes (green), which is then amplified and detected through FFT Fourier analysis. (Note that the endcap electrodes of the Penning trap that provide axial confinement in the direction of the magnetic field are not shown.)	41
Figure 4.4	Schematic representation of the narrow-band FT-ICR technique which includes a variable capacitor (blue) and inductor coil (dark green) to create a resonant circuit. The pickup coil (light green) is used to decouple the resonant circuit to reduce parasitic capacitance. Again, the endcap electrodes of the Penning trap are not shown. (In practice, the primary inductor coil is center-tapped and grounded to alleviate charge build-up on the detection electrodes.)	42
Figure 4.5	Images of a field emission point fabricated at the National Superconducting Cyclotron Laboratory as imaged by (a) an optical microscope, (b) a Scanning Electron Microscope (SEM) at $1800\times$ magnification, and (c) an SEM at $37,000\times$ magnification.	46
Figure 4.6	Schematic of the ion production test setup using the LEBIT 9.4 T superconducting magnet. The electron beam created by the FEP passes through a beam steerer that can block the electron beam from passing through the Penning trap and being collected on a Faraday plate. (The turbo and roughing pumps located on the ejection side of the magnet are not shown in the figure.)	47
Figure 4.7	An FFT resonance of self-excited magnetron motion with trapped ions in a 40 V potential well.	50
Figure 4.8	FFT resonances of two different ion species in the trap using the broadband axial detection method. Both ions were excited simultaneously using a sweep excitation applied to one endcap, while the image current was picked up on the other endcap. The peak on the left was identified as H_3O^+ and the peak on the right was identified as HO_2^+	51
Figure 4.9	An FFT resonance of reduced cyclotron motion of an H_3O^+ ion bunch composed of ~ 2000 ions. The resonance has a full-width half-maximum of 5 Hz and a signal to noise ratio greater than 20.	52

Figure 4.10	Results of the FT-ICR reduced cyclotron frequency monitoring process in the LEBIT magnet showing the average $f_+(\text{H}_3\text{O}^+)$ measurements and fit residuals as a function of time recorded during the course of ~ 9 hours. Each data point is the average of 10 frequency measurements where the error bars correspond to the 1σ uncertainty associated with the distribution of those 10 measurements. The solid lines (red) are the best linear fits to the data. The standard deviation of the fit residuals was determined to be 0.35 Hz corresponding to a relative precision of $\sim 5 \times 10^{-8}$ for the entire data set.	52
Figure 4.11	Results of the precision obtained during the reduced cyclotron frequency monitoring process in the LEBIT hyperbolic trap where in (a) the standard deviation of the entire data set is given when each frequency measurement is the average of a given number of measurements and (b) is a plot of the same data but indicates the measurement time necessary to achieve a given relative precision (assuming 10 seconds per measurement). The solid line (red) in each graph is the best fit to a square root power law which illustrates the statistical behavior of increasing the precision by the square root of the number of individual measurements averaged for a frequency measurement.	53
Figure 4.12	Cylindrical open-ended Penning trap electrode structure and dimensional nomenclature (see text). The compensation electrodes each have four-fold segmentation where the detection electrodes are shown in green and the excitation electrodes are shown in white.	60
Figure 4.13	(a) The normalized radius vs normalized height necessary to orthogonalize a cylindrical trap with negligible gaps and infinite endcaps. (b) Variation of the coefficients, C_6 (in blue) and C_8 (in red), are shown with respect to normalized height for an orthogonalized trap tuned for $C_4 = 0$	61
Figure 4.14	(a) A cross-sectional side view of the orthogonalized cylindrical, electrically compensated, open-ended configuration with grounding electrodes on either side created in SIMION, where the solid black lines represent equipotential lines. (b) A plot of the trapping potential along the z-axis in the trapping region where the dotted line is the on-axis potential extracted from SIMION when the electrode voltages are set to make $C_4 = 0$. The solid line (red) is the best quadratic fit to that potential in a trapping region of length z_o	63
Figure 4.15	Screenshot of the Google SketchUp rendering of the MiniTrap assembly concept pointing out the various components. (Note that the outside of the enclosure is not shown.)	65

Figure 4.16	Isometric view of the copper electrodes utilized to extract the electron beam.	66
Figure 4.17	Isometric view of one (a) four-fold segmented correction electrode and (b) a kapton spacer.	67
Figure 4.18	Isometric view of the MiniTrap assembly designed in SolidWorks. (Note that the top of the enclosure has been removed.)	69
Figure 4.19	(a) Image of the extraction and trapping electrodes (before gold plating and without the correction rings) before assembly. (b) Image of the fully assembled MiniTrap with the top half of the annular enclosure removed before wiring the electrodes. (Note the difference in scale between the two images.)	70
Figure 4.20	Image of the SIPT magnet before the beam line components for testing the MiniTrap had been installed.	71
Figure 4.21	Image of the MiniTrap assembly fully wired (with the top of the enclosure removed and shown near the traps), ready to be mounted and inserted into the SIPT magnet. The two separate wires are of a larger gauge for supplying current to the thermionic emitter.	72
Figure 4.22	A LabVIEW screenshot of an FFT resonance of self-excited magnetron motion of trapped ions of unknown species in a 6.8 V potential well in the MiniTrap.	74
Figure 4.23	Results of trap tuning scans with the MiniTrap showing f_- versus the drive amplitude (proportional to ρ_-) for seven different endcap-to-ring voltage ratios for a 6 V potential well depth (the ring, by convention, is always negative). Note that the solid lines show polynomial fits (using only the first five even terms) to the data, where the error bars are shown, but are too small to be resolved in this image.	76
Figure 4.24	Example from the dipole cleaning technique utilized to determine the ion species in the MiniTrap. Each data point is the average of 25 magnetron excitation and detection measurements when the trap was first cleaned by applying a RF dipole electric field at 5 Vpp for 100 μ s at the cleaning frequency, f_{RF} . The Lorentzian fit to the data is represented by the solid line (red) where the fit results indicate $f_+ = 5.645(1)$ MHz.	77

Figure 4.25	A LabVIEW screenshot of an FFT resonance of reduced cyclotron motion of H_3O^+ ions in a 6 V potential well in the MiniTrap using broadband FT-ICR detection. The faint solid yellow line represents the best Lorentzian fit produced by the LabVIEW program.	78
Figure 4.26	Results of trap tuning scans with the MiniTrap showing f_+ as a function of the drive amplitude (proportional to ρ_+) for five different endcap-to-ring voltage ratios for an 8 V potential well depth (the ring, by convention, is always negative). Note that the solid lines show the results of polynomial fits (using only the first five even terms) to the data, where the error bars are shown, but are too small to be resolved in this image.	79
Figure 4.27	Results of the MiniTrap reduced cyclotron frequency monitoring process showing the average $f_+(\text{H}_3\text{O}^+)$ measurements and the average FFT amplitudes as a function of time recorded over a period of ~ 17 hours. Each data point is the average of 120 frequency measurements (requiring 10 minutes) where the error bars correspond to the 1σ uncertainty associated with the distribution of those 120 measurements. The average slope of the entire data set corresponds to a magnetic field decay rate of $-5.82(4) \times 10^{-8} \text{ hr}^{-1}$	80
Figure 4.28	Results of the precision obtainable from the $f_+(\text{H}_3\text{O}^+)$ monitoring process with 10780 measurements. (a) The standard deviation of the data set is given when each frequency measurement is an average of a given number of measurements and (b) the measurement time necessary to achieve a given relative precision from the same data. The solid line (red) in each graph is the best fit to a square root power law. (Note that the time required for an individual measurement was ~ 6 seconds.)	81
Figure 4.29	Average reduced cyclotron frequency as a function of average FFT amplitude from the f_+ monitoring process of H_3O^+ . Each data point represents one average measurement of 120 individual f_+ measurements. The solid line (red) is the best linear fit to the data and has a slope of $-1371(80) \text{ Hz/a.u.}$	82
Figure 4.30	Results of the pressure scan showing (a) the average reduced cyclotron frequency of H_3O^+ and (b) the average FFT amplitude as a function of pressure, and (c) the average reduced cyclotron frequency as a function of the average FFT amplitude. Each data point represents the average of 20 individual f_+ measurements. The solid lines (red) are the best linear fits to the data. The fit results of (c) give a slope of $-1336(108) \text{ Hz/a.u.}$	82

Figure 4.31	A LabVIEW screenshot of FFT resonances of both reduced cyclotron motion (left) and true cyclotron motion (right) of H_3O^+ ions in a 7.73 V potential well in the MiniTrap using the broadband FT-ICR quadrupole detection configuration.	85
Figure 4.32	Results from the electron beam current scan of f_c and f_+ for H_3O^+ using the optimized parameters. Each data point is the average of 100 measurements where the error bars represent the standard deviation of the individual measurements (some of which cannot be resolved). (Note the difference between the frequency shift of f_c and f_+ as a function of electron beam current, especially at lower electron beam currents – the scales are equivalent).	87
Figure 4.33	Results of the trap depth scan of f_c and f_+ of H_3O^+ . Each data point is an average of 30 measurements where the error bars represent the standard deviation of those measurements (the error bars in the plot of f_+ are too small to be resolved). The linear best fit of $\langle f_+(\text{H}_3\text{O}^+) \rangle$ as a function of trapping potential (solid red line) resulted in a slope of -1350(3) Hz/V. (Note the change in vertical scales between the plot of f_c and f_+).	88
Figure 4.34	Results from the true cyclotron frequency monitoring process while ramping the current in the coil (wrapped around the MiniTrap enclosure) to produce changes in the total magnetic field. Each data point is an average of 100 measurements with the error bars representing the standard deviation of those measurements. The solid line (red) represents the variation of the current supplied by the power supply (values given on the right axis).	89
Figure 4.35	Results of the true cyclotron frequency monitor while alternating every five measurements between a B field scan current and a B field reference current of 10 mA to produce relative changes in the magnetic field. Each data point represents 4000 f_c measurements where the error bars represent the standard deviation of those measurements (see text). The solid red line is the linear best fit to the data and the solid black line is the zero-shift reference. The linear best fit resulted in a slope of 0.080(3) Hz/mA.	90
Figure 4.36	Illustration of the precision obtained from the alternating B field scan where (a) the standard deviation of the data is given when each frequency measurement was an average of a given number of measurements and (b) the measurement time necessary to achieve a given relative precision from the same data. The solid line (red) in each graph is the best fit to a square root power law fit.	91

Figure 4.37	An FFT spectrum showing the resonances from the reduced cyclotron motion (left), the reference signal (middle), and the true cyclotron motion (right) from an individual measurement of H_3O^+ in the MiniTrap. (The height of the f_{Ref} resonance peak has been truncated to clearly show the f_+ and f_c resonance peaks.)	93
Figure 4.38	Results of the long-term MiniTrap monitoring process showing the $\langle f_c(\text{H}_3\text{O}^+) \rangle$ and associated $\langle f_+(\text{H}_3\text{O}^+) \rangle$ measurements over the course of ~ 11 days and 9 hours. Each data point is the average of 100 frequency measurements (10 minutes each) where the error bars correspond to the 1σ uncertainty associated with the distribution of those 100 measurements. The linear best fit of the f_c data (shown in red) corresponds to a magnetic field decay rate of $-3.3(2) \times 10^{-10} \text{ hr}^{-1}$. (Note that the difference in scales between the two graphs is \sim a factor of four.)	93
Figure 4.39	Frequency correlation with FFT amplitude from the long-term monitoring process for (a) $\langle f_c(\text{H}_3\text{O}^+) \rangle$ and (b) $\langle f_+(\text{H}_3\text{O}^+) \rangle$. Each data point represents an average of 100 individual measurements. The linear best fits to the data (solid red lines) for (a) and (b) resulted in slopes of $20(3) \text{ Hz/a.u.}$ and $-156(2) \text{ Hz/a.u.}$, respectively.	95
Figure A.1	Schematic of the RF switch used to eliminate leakage output from the function generator.	108
Figure B.1	Screenshot of the MiniTrap control system (MTCS) front panel (with text removed to conform to thesis submission guidelines).	111

Chapter 1

Introduction

One of the driving forces behind the work presented in this dissertation is to support the evolution of the scientific understanding of neutrino physics by directly measuring the double-beta decay Q -value of the neutrinoless double-beta decay candidate ^{82}Se . In addition, I have developed a device, a high-precision magnetometer, to enhance the mass measurement program at the Low-Energy Beam and Ion Trap (LEBIT) facility at the National Superconducting Cyclotron Laboratory (NSCL).

In nuclear physics, the Q -value corresponds to the energy change in a nuclear reaction or decay and is defined as the difference between the total mass-energy of the reactants or mother nucleus and the total mass-energy of the products or daughter nucleus. Therefore, to determine a Q -value to high-precision, these masses need to be known to high-precision. Many Penning Trap Mass Spectrometry (PTMS) facilities throughout the world have been used to perform mass measurements on stable and short-lived isotopes in recent years to investigate nuclear shell structure [1, 2, 3], halo nuclei [4, 5], nuclear astrophysics [6, 7, 8], tests of the Isobaric Multiplet Mass Equation (IMME) [9, 10] and fundamental interactions [11, 12], in addition to determining beta decay Q -values [13]. PTMS facilities have achieved

mass measurement fractional precisions as small as 7 parts in 10^{-12} for stable isotopes [12] and less than 10^{-8} for unstable isotopes [14, 15]. Short-lived isotopes with half-lives on the order of 10 ms have been measured [4], but generally at a sacrificed precision. Because of the success of PTMS over the years, it is now considered to be the most precise and accurate method for determining atomic masses and, therefore, beta decay Q -values [16].

1.1 Neutrinoless Double-Beta Decay

Of the four fundamental forces, the weak force is responsible for beta decay (β decay). β decay occurs either when, in the nucleus of an atom, a neutron decays into a proton and emits an electron and an electron antineutrino or when a proton decays into a neutron and emits a positron and an electron neutrino, in processes referred to as β^- decay and β^+ decay, respectively. Nuclei also undergo double-beta decay ($\beta\beta$ decay) where the atomic number is changed by two units in a one-step process. Both single β decay and $\beta\beta$ decay can only occur when energetically allowed, i.e. the decaying nucleus must have a smaller binding energy than the final nucleus. It is theoretically possible that during $\beta\beta$ decay the neutrino could be exchanged as a virtual particle between the decaying nucleons resulting in no neutrinos being emitted, in a process called neutrinoless double-beta decay ($0\nu\beta\beta$ decay). $0\nu\beta\beta$ decay can only occur if the neutrino has mass and is its own antiparticle (a Majorana particle), but $0\nu\beta\beta$ decay has yet to be experimentally observed. Many nuclei are allowed to undergo $\beta\beta$ decay; $\beta\beta$ decay is highly suppressed, however, compared to single β decay. In order to experimentally observe $0\nu\beta\beta$ decay it is therefore necessary to search for $\beta\beta$ decay in nuclei that are energetically forbidden to undergo single β decay.

The neutrino was first proposed by Wolfgang Pauli in 1930 in an effort to resolve the

missing energy observed in β^- decay as required by the laws of conservation of energy, momentum, and angular momentum [17]. In 1956, Clyde Cowan and Frederick Reines published an article in Science [18] confirming the existence of the neutrino through β decay experiments performed near nuclear reactors. Since their monumental work, three different neutrino flavors, corresponding to the three types of leptons, have been experimentally verified. More recently, the results of neutrino oscillation experiments indicate that the mass of the neutrino is non-zero [19, 20, 21]. The mass hierarchy (mass ordering of the three mass eigenstates) and the absolute mass scale of the neutrino, however, are unknown. Furthermore, the nature of the neutrino is also unknown; is it a Dirac or Majorana particle, i.e. is the neutrino its own antiparticle or not? This is a pressing question in physics since verification of the Majorana nature of the neutrino would indicate new physics beyond the Standard Model. At present the only known practical method for determining the nature of the neutrino is through $0\nu\beta\beta$ decay measurements [22]. These experiments rely on precise and accurate $\beta\beta$ decay Q -values not only for their design, but also for the theoretical interpretations of the observations.

In some cases $\beta\beta$ decay Q -values determined prior to direct Penning trap measurements were found to vary by more than 10 keV [23]. The Q -values for a number of $0\nu\beta\beta$ decay candidates have been determined via PTMS [23, 24, 25, 26, 27, 28, 29, 30, 31, 32, 33]. Of all the $0\nu\beta\beta$ decay candidates currently employed in $0\nu\beta\beta$ decay experiments, ^{82}Se is the only one whose Q -value has not been measured directly through high-precision PTMS. In anticipation of $0\nu\beta\beta$ decay experiments with ^{82}Se , the first direct $0\nu\beta\beta$ decay Q -value measurement of ^{82}Se that was performed at the LEBIT PTMS facility is presented.

1.2 PTMS at the NSCL and Enhancements

The LEBIT facility began performing high-precision mass measurements at the NSCL with a pilot experiment in 2005 [14]. Since the LEBIT facility's first mass measurement, the masses of nearly forty other isotopes of various elements have been measured with fractional precisions ranging from a few parts in 10^7 [34, 35] to better than 5 parts in 10^9 [36]. Even though the techniques utilized in performing mass measurements at the LEBIT facility have been refined, enhancements can be made to further improve sensitivity, increase precision, and boost efficiency to maximize the use of beam time and expand scientific output.

Two enhancements that have recently been installed and commissioned are the Stored Wave Inverse Fourier Transform (SWIFT) cleaning technique [37] and a Laser Ablation ion Source (LAS). The SWIFT cleaning technique increases the LEBIT facility's operational efficiency by eliminating the need to identify contaminant ions in the trap while increasing beam purity to reduce systematic effects. The LAS will increase the precision of the LEBIT mass spectrometer by facilitating tests for mass-dependent systematic effects with mass measurements of carbon clusters that provide exact mass intervals. The LAS will also expand science opportunities by producing stable and long-lived isotopes for mass measurements. Another enhancement is the development of single ion sensitivity with a Single Ion Penning Trap (SIPT) to measure the masses of exotic rare isotopes available only at very low yields [38]. Finally, the development project presented in this work will increase the precision and sensitivity of mass measurements performed at the LEBIT facility while expanding scientific output by increasing measurement efficiency. To accomplish this goal, a high-precision magnetic field monitoring device was developed to continuously monitor short-term magnetic field strength fluctuations of the LEBIT facility's 9.4 T superconducting magnet.

Chapter 2

LEBIT Facility

Located at the NSCL on the campus of Michigan State University, the LEBIT PTMS facility was the first PTMS facility to perform high-precision mass measurements on isotopes produced via projectile fragmentation [14]. To produce rare isotopes at the NSCL, a high-energy (~ 140 MeV/u) heavy ion beam, from the Coupled Cyclotron Facility (CCF), impinges on a thin target of a light element, e.g. beryllium, as shown in Fig. 2.1. A plethora of fragments exit the target and are separated in-flight by their mass-to-charge ratio in the A1900 fragment separator [39]. What separates this rare isotope production technique from the others is that it is chemically independent, it is fast so the rare isotope beam experiences minimal decay losses, and it produces a wide variety of rare isotopes far from stability. A beam stopping facility then manipulates the high-energy beam to provide a pure, low-energy beam with low emittance as required by low-energy experiments, such as high-precision mass measurements [40, 41]. The beam is then accelerated and delivered to the LEBIT facility where it is cooled and bunched before it is injected into the high-precision 9.4 T Penning trap mass spectrometer [42].

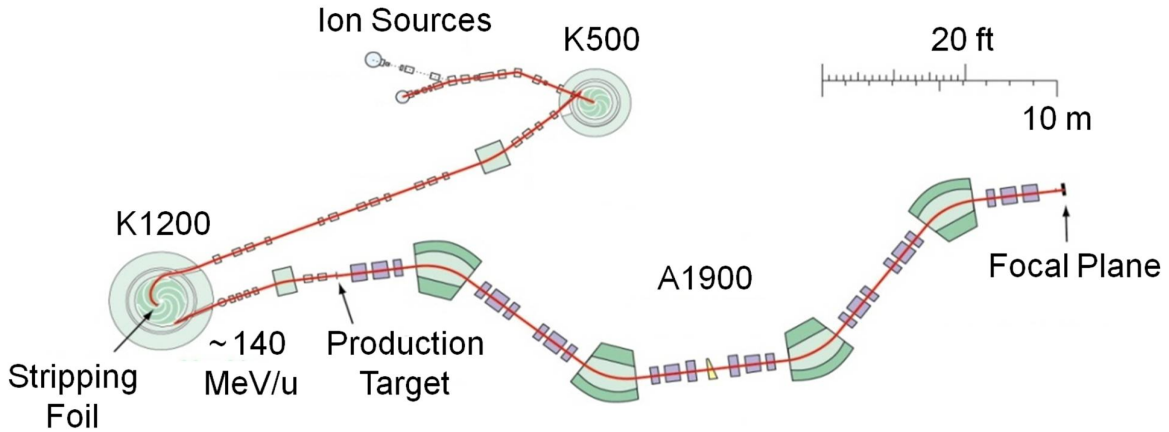


Figure 2.1: Basic layout of the rare isotope production technique via projectile fragmentation at the National Superconducting Cyclotron Laboratory’s Coupled Cyclotron Facility. “For interpretation of the references to color in this and all other figures, the reader is referred to the electronic version of this dissertation.”

2.1 LEBIT I - First Experiments with Rare Isotopes

Since 2005, the LEBIT facility has made numerous contributions to many fields of physics. In 2006, the first article reporting a mass measurement using the LEBIT facility was with a high-precision mass measurement of ^{38}Ca , a superallowed β emitter [14]. This measurement together with a high-precision mass measurement of ^{37}Ca provided data to test the vector current conservation hypothesis and confirm the IMME [15]. The shortest lived isotope LEBIT has measured so far is ^{66}As [43], with a half-life 96 ms. This measurement was part of a series of high-precision mass measurements near $N = Z = 33$ investigating the rp process for nuclear astrophysics and neutron-proton pairing energies for nuclear structure studies. In 2008, the LEBIT group discovered a nuclear isomer in ^{65}Fe [34]. The LEBIT group again made contributions to understanding the rp process in nuclear astrophysics with mass measurements of the $N \approx Z \approx 34$ nuclides [44]. In 2009, a result was published on the validity of the IMME for the $A = 32$, $T = 2$ quintet, but this time indicated a breakdown of the model [36]. Another noteworthy publication reported mass measurements

of the neutron-rich Fe and Co isotopes around $N = 40$ with implications in nuclear shell structure, and included the confirmation of an isomeric state of ^{67}Co [35].

In 2009, owing to the success of the LEBIT PTMS facility in conjunction with the beam stopping techniques developed at the NSCL, the original beam stopping and LEBIT facilities were decommissioned to make way for the next-generation of low-energy precision experiments at the NSCL. The next-generation beam stopping program includes upgrades to expand its reach to the most exotic rare isotopes and to not only deliver low-energy rare isotope beams to the upgraded LEBIT facility, but also for reacceleration with a new linear accelerator (ReA3) and to a recently commissioned laser spectroscopy facility (BECOLA). In addition, the enhancements being made to the LEBIT facility will allow a greater reach to isotopes further from the valley of stability, enhance sensitivity, increase precision, and improve efficiency to maximize the use of beam time and increase scientific output.

2.2 LEBIT II - Features of Relocated Facility

To make room for the upgrades to the beam stopping facility, the expansion of the low-energy experimental area, and the installation of ReA3, the entire LEBIT beam line had to be relocated to a new low-energy experimental area. A schematic layout of the upgraded facilities is shown in Fig. 2.2. The relocation required all of the vacuum components, beam line components, electronics, and wiring to be completely dismantled and reassembled. Much of the time required to upgrade the beam stopping facility was devoted to rebuilding the LEBIT beam line and bringing the LEBIT facility back on-line. To provide efficient transport of the beam while leaving the transport beam line on ground potential, the beam stopping components, the low-energy high-precision experiments, as well as the reaccelerator have to

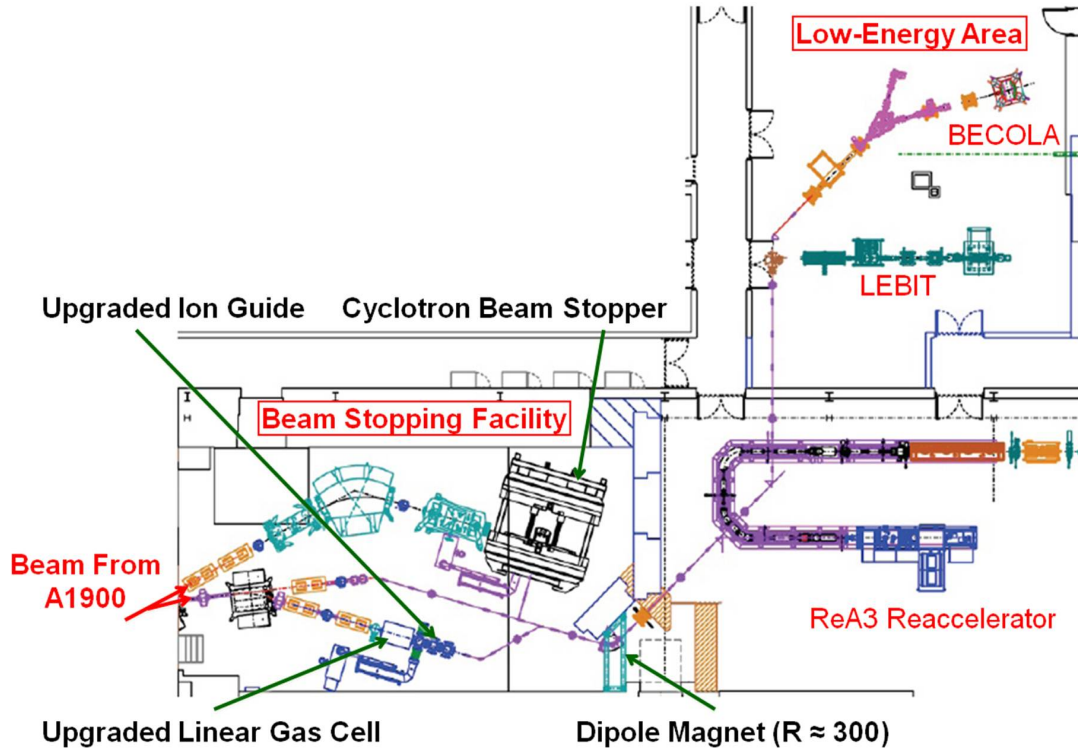


Figure 2.2: Schematic layout of the upgraded beam stopping facility, low-energy area, and reaccelerator.

operate at 60 kV. To achieve this, the LEBIT beam line was retrofitted with 60 kV insulators and a high voltage isolation transformer was installed to power the LEBIT facility's beam line electronics.

The LEBIT facility was recommissioned during the spring of 2012 with a high-precision mass measurement of ^{48}Ca that utilized an off-line ion source. Together with a recent ^{48}Ti mass measurement [45], a more precise $\beta\beta$ decay Q -value of ^{48}Ca was obtained [46]. More recently, a direct double-electron capture Q -value measurement of ^{78}Kr [47] and the direct $\beta\beta$ decay Q -value measurements of ^{48}Ca [48] and ^{96}Zr [49] have been performed. In the spring of 2013, the upgraded LEBIT facility received its first rare isotope beam from the NSCL's CCF together with the upgraded beam stopping facility and successfully performed a high-precision mass measurement of ^{63}Co , with a half-life of 26.9 seconds.

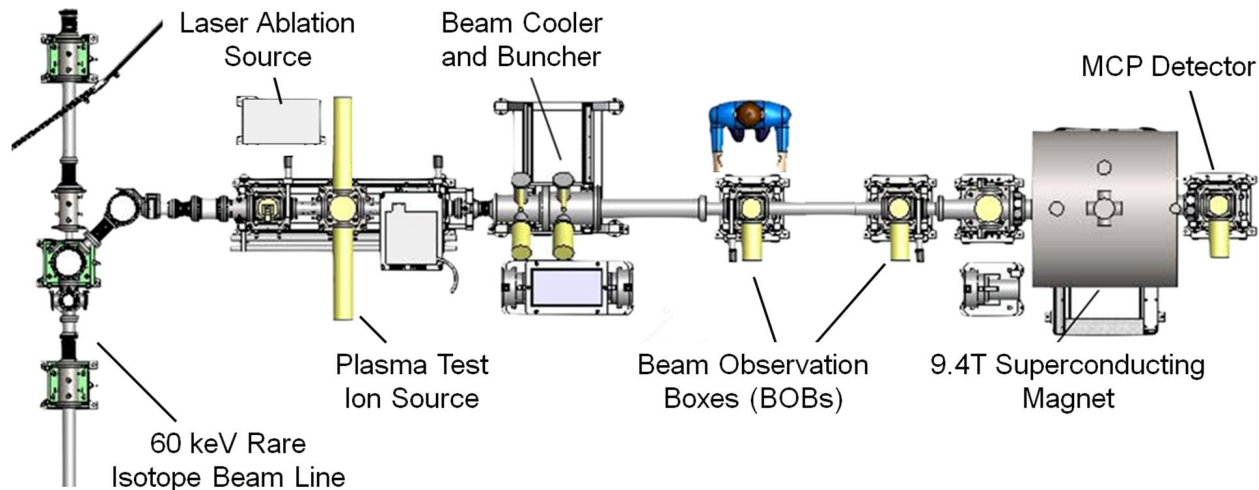


Figure 2.3: Layout of the upgraded LEBIT facility.

2.3 Basic Components of the LEBIT Facility

The main components that comprise the LEBIT facility are shown in Fig. 2.3. First, the vacuum system allows all of the components of the LEBIT facility to be maintained at Ultra-High Vacuum (UHV). Gate valves are located throughout the facility to separate various sections of the UHV system for maintenance purposes. To transport the beam, the UHV beam line sections of the facility are fitted with electrostatic lenses and deflectors [50]. Two off-line ion sources are connected to the beam line: an off-line plasma Test Ion Source (TIS) and the recently commissioned LAS. Another main component of the LEBIT facility is the beam cooler and buncher which prepares the ions for a high-precision mass measurement. The LEBIT facility houses a high-precision measurement Penning trap in a 9.4 T superconducting magnet to provide the strong and very uniform magnetic field necessary for PTMS. Finally, Beam Observation Boxes (BOBs) fitted with Multi-Channel Plate (MCP) detectors, silicon detectors, and Faraday cups are used to characterize the beam and detect ionized isotopes.

The LEBIT facility is controlled remotely via LabVIEW software on a server machine

that is interfaced to a programmable logic controller. This allows convenient remote control of all turbo pumps, gate valves, electrode voltages, detectors, and associated electronics needed to perform a mass measurement. Not only is remote control over the entire system convenient, but it is also necessary since the beam line must be held at 60 kV above ground potential to accept beam from the recently upgraded beam stopping facility. Even when operating the beam line at ground potential, remote control of the beam line components is required as two sections of the beam line operate at -5 kV and -2 kV with respect to the rest of the beam line for efficient beam transport.

2.3.1 Ion Sources

Before a measurement can be performed, an ionized isotope of interest needs to be produced. The LEBIT facility now has three ion sources capable of providing ionized isotopes: one on-line source and two off-line sources. The on-line ion source consists of the CCF and beam stopping facility that delivers exotic rare isotopes. The two off-line ion sources are the TIS and the recently commissioned LAS.

The rare isotopes provided by projectile fragmentation from NSCL's CCF are transported by the high-energy beam lines to a gas cell in the beam stopping facility. The high-energy beam passes through the gas cell where the ions are stopped and thermalized through collisions in ultra-high purity helium at a pressure of up to 100 mbar. The thermalized ions, with a significant fraction in the 1+ charge state, are extracted and delivered into high vacuum through a Radio-Frequency Quadrupole (RFQ) ion guide (shown in Fig. 2.4(b)), then accelerated to 60 keV into a beam line system which transports them efficiently to a dipole magnet where the rare isotopes are separated by their mass-to-charge ratio, or m/q , with a resolving power of ~ 300 (the location of the dipole magnet can be seen in the stopped

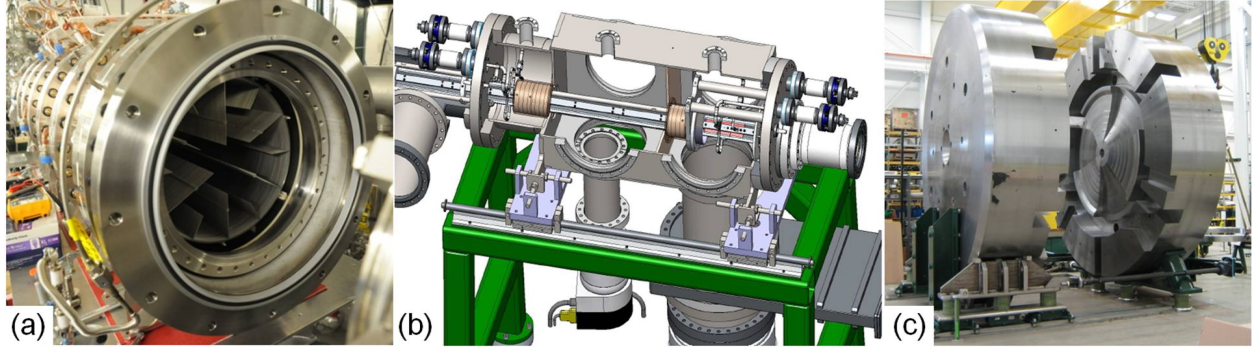


Figure 2.4: Components of the upgraded beam stopping facility showing (a) a photo of the next-generation linear gas cell, (b) a schematic of the upgraded ion guides, and (c) a photo of the cycstopper being assembled.

beam facility layout of Fig. 2.2). Thus, a beam free from non-isobaric contamination can be provided for high-precision mass measurements.

To provide rare isotope beams of greater intensity, the beam stopping facility has commissioned a next-generation gas cell (shown in Fig. 2.4(a)) to increase beam stopping efficiencies. The beam stopping facility is also developing a cyclotron beam stopping device (shown in Fig. 2.4(c)) to increase stopping efficiencies for lighter rare isotopes. These upgrades will allow the LEBIT facility to take advantage of more pure beams and shorter-lived rare isotopes that were previously out of reach. Looking further into the future, the construction of the Facility for Rare Isotope Beams (FRIB) is underway [51] and will provide beam intensities many orders of magnitude greater than what is currently being delivered, allowing for studies of isotopes even further from the valley of stability.

Both off-line ion sources are located adjacent to the beam line, just upstream from the cooler and buncher (as shown in Fig. 2.3). The TIS (shown in Fig. 2.5) was purchased from Colutron Research Corporation and has been operational since LEBIT's start in 2005. The TIS allows for off-line tuning and optimization of the system without the need of CCF beam time. The TIS also provides reference masses to calibrate the magnetic field during rare

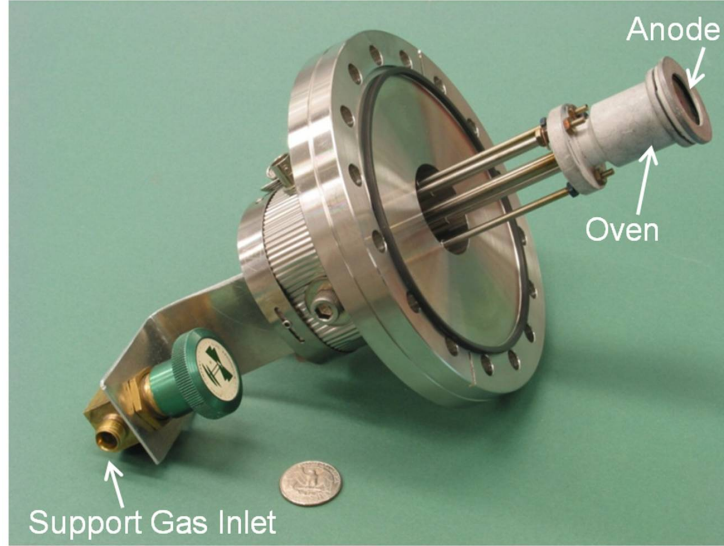


Figure 2.5: The plasma test ion source assembly shown removed from the vacuum chamber.

isotope measurements.

The TIS is able to produce stable alkali ions (Na, K, Rb, and Cs) as well as ionized noble gases (Ne, Ar, and Kr) depending on which mode the TIS is utilized. In surface ionization mode, a tungsten filament is heated by passing a current through the filament, positively biased to ~ 100 V, inside a boron nitride oven operated at temperatures up to 2000 degrees Celsius. When the filament is heated, alkali ions (as impurities in the filament) are created through surface ionization and are extracted through a pin hole in the anode at the end of the chamber. Alternatively, ionized noble gases can be produced by feeding a neutral gas into the ion source chamber through a support gas inlet in the back of the ion source. The filament is then reversed biased until a discharge is created. The shower of electrons created from the discharge bombards the gas molecules and ionizes the gas through electron-impact ionization. The TIS is located perpendicular to the beam line, therefore, an electrostatic quadrupole steering element is utilized to deflect the beam either upstream to the beam stopping facility or downstream through the beam cooler and buncher to the 9.4 T Penning trap mass spectrometer.

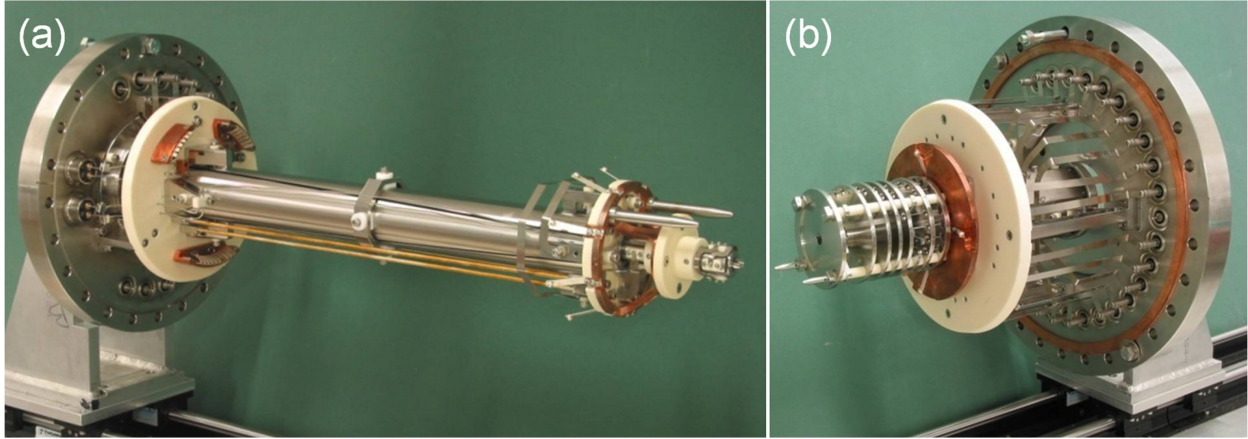


Figure 2.6: Photos of (a) the cooler and (b) the buncher before insertion into the beam line.

One of the upgrades recently made to the LEBIT facility was the construction of the LAS by Scott Bustabad. The LAS is located opposite from the TIS on the other side of the beam line. The LAS produces ions by focusing a laser beam, produced by a high power ~ 2 W Nd:YAG laser, onto a metallic target. When a pulse from the laser strikes the target ionized material is ejected, extracted, and transported to the electrostatic quadrupole steering element that deflects the beam either upstream or downstream.

2.3.2 Cooler and Buncher

The cooler and buncher [52] are located just downstream of the off-line ion sources and the components are shown, removed from the beam line, in Fig. 2.6. The cooler and buncher transform the continuous beam into the low-emittance pulses with low-energy spread required for high-precision Penning trap mass measurements. The cooler and buncher are composed of a gas-filled RFQ in conjunction with a linear Paul trap, a standard tool used to produce low-emittance pulsed ion beams [42].

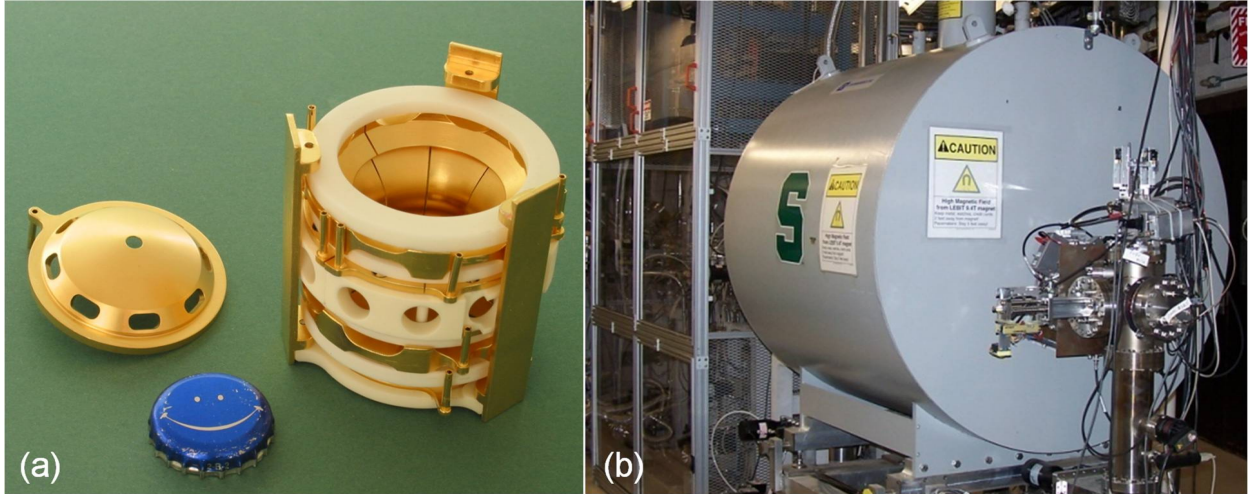


Figure 2.7: Photos of (a) LEBIT's hyperbolic Penning trap and (b) the 9.4 T superconducting magnet.

2.3.3 9.4 T Penning Trap Mass Spectrometer

After the continuous beam has been cooled and bunched, it is transported to the 9.4 T superconducting Penning trap mass spectrometer. The LEBIT mass spectrometer employs a persistent superconducting magnet with a horizontal bore (shown in Fig. 2.7(b)) to produce a highly uniform magnetic field with a strength of 9.4 T. The Penning trap, shown in Fig. 2.7(a), consists of two hyperbolic endcaps and an eightfold segmented ring used to create an electric quadrupole trapping potential with a cylindrical symmetry. The Penning trap electrode structure resides in the center of the bore of the magnet and can be held at room temperature or cooled with Liquid Nitrogen (LN₂). To reduce the influence of external fields affecting the homogeneity of the magnetic field, the magnet is actively shielded through the implementation of Gabrielse coils [53].

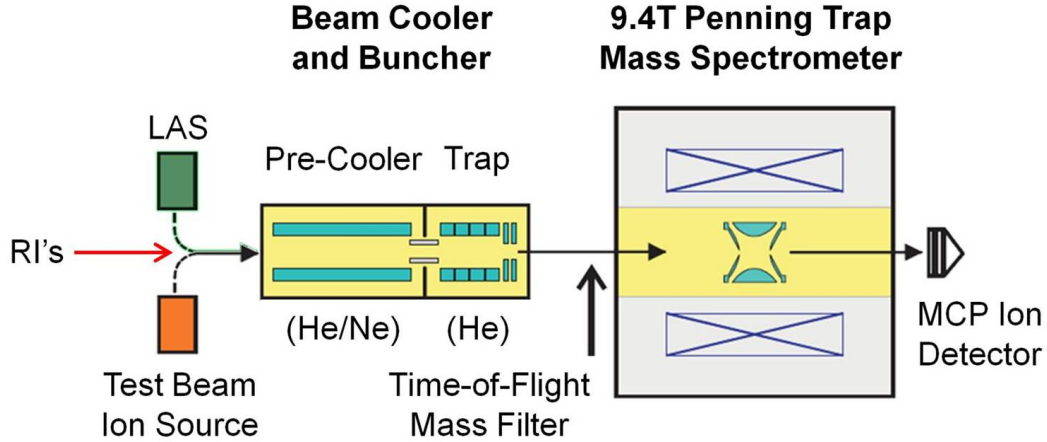


Figure 2.8: Schematic diagram of ion preparation, non-isobaric purification, and ion detection equipment at the LEBIT facility.

2.4 LEBIT II - Techniques Used at the LEBIT Facility

2.4.1 Ion Preparation and Non-Isobaric Beam Purification

A basic schematic diagram of the equipment used to prepare, purify, and detect ions at the LEBIT facility is shown in Fig. 2.8. Before the rare isotope beam enters into the cooler, it is slowed down to ~ 10 eV using a set of electrostatic deceleration electrodes. (Alternatively, ions can be sent to the cooler from either the TIS or the LAS.) The ions then enter the cooler section of the cooler and buncher where slowing and transverse cooling of the ions is performed through buffer-gas cooling. The RFQ ion guide structure in the cooler provides radial confinement of the ions [54] through a set of four rodlike electrodes. A Radio-Frequency (RF) signal at a given phase, amplitude, and frequency is applied to two electrodes opposite one another. The same signal is applied to the other two rods, but 180 degrees out of phase. The application of these signals to the rods creates a pseudopotential that radially confines the ions [55, 56].

The RFQ structure in the cooler implements a novel design where the four ion guide

electrodes are located inside a cylindrical electrode which is split lengthwise into four wedge-shaped electrodes to provide a field gradient that drags the ions through the buffer-gas [50]. The cooler is usually filled with ultra-pure helium gas at a pressure of a few 10^{-2} mbar and is regulated by an electromagnetic solenoid valve controlled by a Proportional-Integral-Derivative (PID) loop [57].

A micro-RFQ (μ RFQ) separates the cooler and buncher sections to allow for differential pumping and for efficient transport from the cooler to the buncher. In the μ RFQ, a helium background is maintained at a pressure of 10^{-4} mbar. The buncher electrode configuration consists of a conventional RFQ ion guide located inside seven ring electrodes. The ion guide provides the radial confinement of the ions and the seven ring electrodes are used to produce an axial electrostatic field. In continuous mode, the beam's emittance and energy spread is lowered in the cooler, then the beam is transported through the μ RFQ and passes through the buncher. Alternatively, the seven ring segments can be biased to create an axial potential well where the ions can be accumulated and further cooled, usually for about 30 ms. The cooled ion bunch is ejected from the buncher by lowering the potential on the final ring electrode to deliver a low-emittance bunch with a sub- μ s pulse width [57].

The low-emittance pulse of ions ejected from the buncher is accelerated to 2 keV, focused, and transported to the high-precision Penning trap located inside the horizontal bore of the 9.4 T superconducting solenoid magnet. During transport to the magnet, the ions pass through a pulsed drift tube that adjusts the kinetic energy of the ion bunches for optimal injection into the Penning trap [58]. Before injection into the magnet, any non-isobaric contaminants present in the pulse of ions from the buncher can be separated by their A/Q value using a Time-Of-Flight (TOF) mass filter with a resolving power of ~ 200 [57]. The ions are then slowed inside the injection optics, located in the first half of the magnet, leading

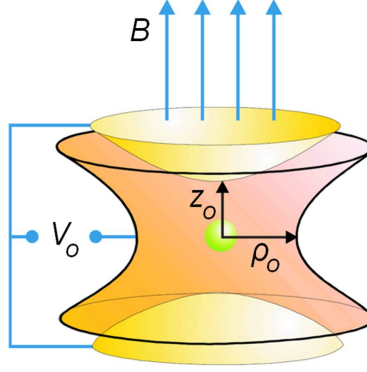


Figure 2.9: Schematic of a Penning trap. The hyperbolic electrode structure of the Penning trap is used to create a quadrupole potential by applying a voltage, V_o , across the endcap and ring electrodes in a strong magnetic field, B . The size of the trap is characterized by the trap length, z_o , and the trap radius, ρ_o .

to the Penning trap. Before the ions enter the Penning trap, a Lorentz steerer is used to quickly prepare the ions for a mass measurement [59].

2.4.2 Penning Trap Mass Spectrometry

PTMS relies on the fundamental motion of charged particles trapped in a strong magnetic field. To achieve 3-D confinement of charged particles, an axial quadrupole electric field is superimposed on top of a strong, homogeneous axial magnetic field as shown in Fig. 2.9. The strong magnetic field confines the ions radially, while the quadrupole electric field confines the ions in the axial direction. The quadrupole electric field at the LEBIT facility is created by two hyperbolic endcap electrodes and one hyperbolic ring electrode that has been segmented eight-fold for the application of various RF electromagnetic fields. To allow the injection and ejection of ions into and out of the trap there is a small hole in the center of each of the endcaps. The size of the Penning trap can be described by the characteristic trap parameter, d , given by:

$$d = \sqrt{\frac{\rho_o^2}{4} + \frac{z_o^2}{2}}, \quad (2.1)$$

where ρ_o corresponds to the trap radius, and z_o corresponds to the trap length. The LEBIT Penning trap, for example, has a d of 10.23 mm.

The hyperbolic electrode structure is the most desirable Penning trap geometry, because higher order components of the quadrupole electric field are minimized. Imperfections in the trapping potential due to the segmented ring electrodes and the holes in the endcaps, however, distort the perfect quadrupole potential and introduce anharmonic terms to the pure quadrupole potential. Machining imperfections also contribute to anharmonicities in the trapping potential. Therefore, additional correction electrodes between the endcaps and ring electrodes and at the entrance and exit holes of the endcaps (not shown in Fig. 2.9), surround the trap and are tuned to minimize the effects of these trap imperfections on the ion motion [58].

Charged particles in the presence of a magnetic field undergo cyclotron motion, a radial motion about the magnetic field as described by the Lorentz force, at a frequency that depends only on the charge, q , and mass, m , of the particles together with the strength of the magnetic field, B , at the position of the particles, and is given by the expression:

$$\omega_c = \frac{q}{m} B. \quad (2.2)$$

When charged particles are also axially confined inside a Penning trap, by superimposing the quadrupole electric field on top of the magnetic field, they undergo the three basic eigenmotions, or normal-mode oscillations, shown in Fig. 2.10: one in the axial direction at a frequency, ω_z , and two in the radial direction at frequencies ω_- and ω_+ . The eigenmotion associated with frequency ω_- , known as magnetron motion, is resultant of the $\mathbf{E} \times \mathbf{B}$ drift motion and is typically much slower than the reduced cyclotron motion at the modified

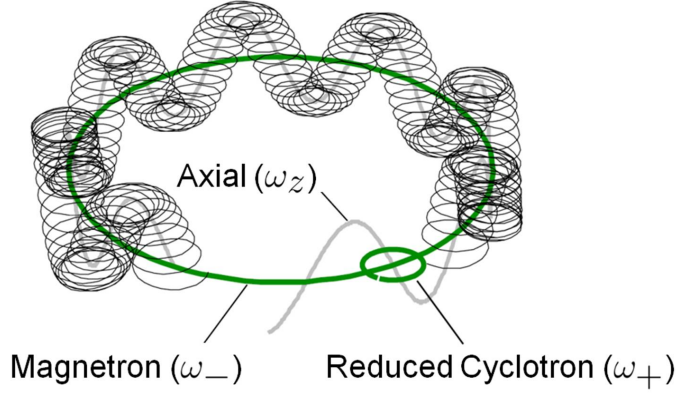


Figure 2.10: Illustration of the eigenmotions executed in a Penning trap in a strong magnetic field: axial oscillations in the direction parallel to the magnetic field, the slower radial magnetron motion due to the $\mathbf{E} \times \mathbf{B}$ drift, and the faster radial reduced cyclotron motion.

frequency of ω_+ .

For particles in a Penning trap with a pure electric quadrupole potential, the radial frequencies of the eigenmotions are related to the true cyclotron frequency and the axial oscillation frequency by the expression:

$$\omega_{\pm} = \frac{\omega_c}{2} \pm \sqrt{\frac{\omega_c^2}{4} - \frac{\omega_z^2}{2}}. \quad (2.3)$$

The axial oscillation frequency, ω_z , can be found through the relation:

$$\omega_z = \sqrt{\frac{qV_0}{md^2}}, \quad (2.4)$$

where V_0 is the potential difference between the endcaps and the ring electrode and d is the characteristic trap parameter. Two other important equations that relate the frequencies of the radial motions of ions confined in a Penning trap are:

$$\omega_+ + \omega_- = \omega_c \quad (2.5)$$

and

$$\omega_+\omega_- = \frac{\omega_z^2}{2}. \quad (2.6)$$

At the LEBIT facility, the true cyclotron frequency, $\nu_c = \omega_c/2\pi$, of an ion is measured using the TOF – Ion Cyclotron Resonance (TOF-ICR) detection technique [60, 61]. First, the ions are given an initial kick off-center with the Lorentz steerer [62] prior to entering the trap to prepare them with some initial magnetron motion. The ions are then dynamically captured in the Penning trap such that the ions’ axially energy in the trap is minimized by setting the pulsed drift tube potential. Potential isobaric contaminants are then removed from the Penning trap by driving them to large radial orbits with a resonant RF azimuthal dipole field. Then, to measure ν_c , the trapped ions are exposed to an azimuthal quadrupole RF field at a frequency ν_{RF} near their cyclotron frequency with the appropriate RF amplitude and excitation time which fully converts the ions’ initial magnetron motion into cyclotron motion [60, 61].

After ejection from the trap, the ions travel through the inhomogeneous section of the magnetic field, where the ions’ radial energy is transferred into axial energy [63]. An ion’s TOF is then determined by detecting the ion with the MCP located just downstream of the superconducting magnet. In resonance, i.e., $\nu_{RF} = \nu_c$, the energy pickup of an ion’s radial motion is maximized and results in a shorter TOF to the MCP [61]. For a cyclotron frequency determination, this cycle of trapping, excitation, ejection, and TOF measurement is repeated for different frequencies near the cyclotron frequency of the ion of interest. Through this process cyclotron resonance curves, as shown in Fig. 2.11, with a centroid at ν_c are obtained.

The mass resolving power, defined as $m/\Delta m$ of a cyclotron frequency measurement, is linearly proportional to the RF excitation time, T_{RF} , and the cyclotron frequency, ω_c , and

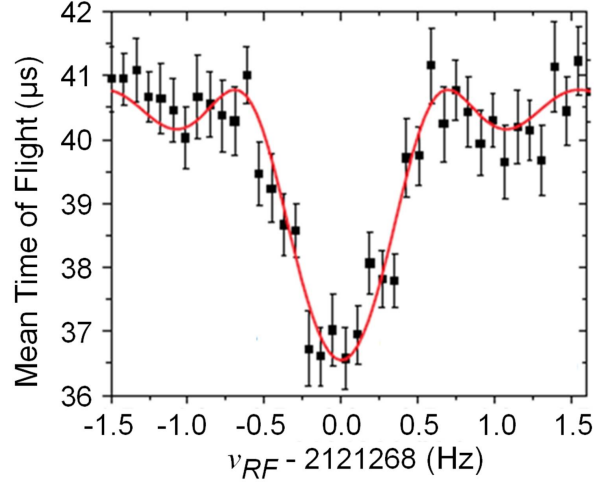


Figure 2.11: A typical time-of-flight cyclotron resonance curve. A fit of the theoretical line shape to the data is represented by the solid line (red).

can be written as:

$$R \equiv \frac{m}{\Delta m} = T_{RF} \cdot \nu_c. \quad (2.7)$$

It is therefore desirable to use excitation times as long as possible, the limits of which are set by damping due to collisions with background gas and the lifetime of the isotope being measured. Increased precision of the cyclotron frequency measurement isn't enough to extract an ion's mass since the mass also depends on the strength of the magnetic field, which needs to be known to a precision comparable to the precision of the cyclotron frequency measurement. To determine the strength of the magnetic field, interleaving calibration (or reference) measurements on an ion species with a well-known mass (and known charge state) must be performed.

2.4.3 Reference Measurements

In a perfect world, the magnetic field would only need to be calibrated once; the magnetic field strength of LEBIT's persistent 9.4 T superconducting magnet, however, slowly decays

over time. The magnetic field is persistent, meaning it is only energized once, and as the electrons encounter a small resistance while flowing through splices in the superconducting wire of the magnet the current slowly decreases [64]. Thankfully, the resistance is so small that the relative change in the magnetic field is on the order of $(dB/B)/dt \approx -8 \times 10^{-8} \text{ hr}^{-1}$ [65], but it can still have an effect on a high-precision measurement that might extend over the course of an hour or so and result in a broadening of the cyclotron resonance curve. To mitigate broadening of cyclotron frequency resonances due to the magnetic field decay, a small current is passed through room-temperature compensation coils, composed of a pair of insulated copper wires wound around the bore tube of the magnet, that is ramped at a steady rate to stabilize the drift of the resulting total magnetic field. Thus, if the magnetic field drift of the superconducting magnet is linear with a constant rate of decay, there would be minimal need for reference measurements (except for initial calibration measurements when the power supply of the magnetic field compensation coils is reset). Unfortunately, non-negligible changes in the magnetic field are known to be caused by pressure fluctuations in a pressure unregulated cryostat of a superconducting magnet containing Liquid Helium (LHe) [66] and can be just as important as those caused by magnetic field decay.

During the LEBIT facility's pilot experiment, significant changes in the magnetic field were found to be correlated to variations in the atmospheric pressure as shown in Fig. 2.12(a) [65]. To eliminate the effects of atmospheric pressure affecting the internal pressure of the LHe bath in the cryostat, an electromagnetic flow regulating valve together with a high-precision barometer (Setra), used to measure the cryostat's pressure, and a LabVIEW controlled PID loop were implemented to regulate the cryostat's pressure to within 10 ppm [65]. Fig. 2.12(b) shows that even with a pressure stabilized cryostat, noticeable non-linear changes in the magnetic field were still present on the scale of a few hours. It was therefore

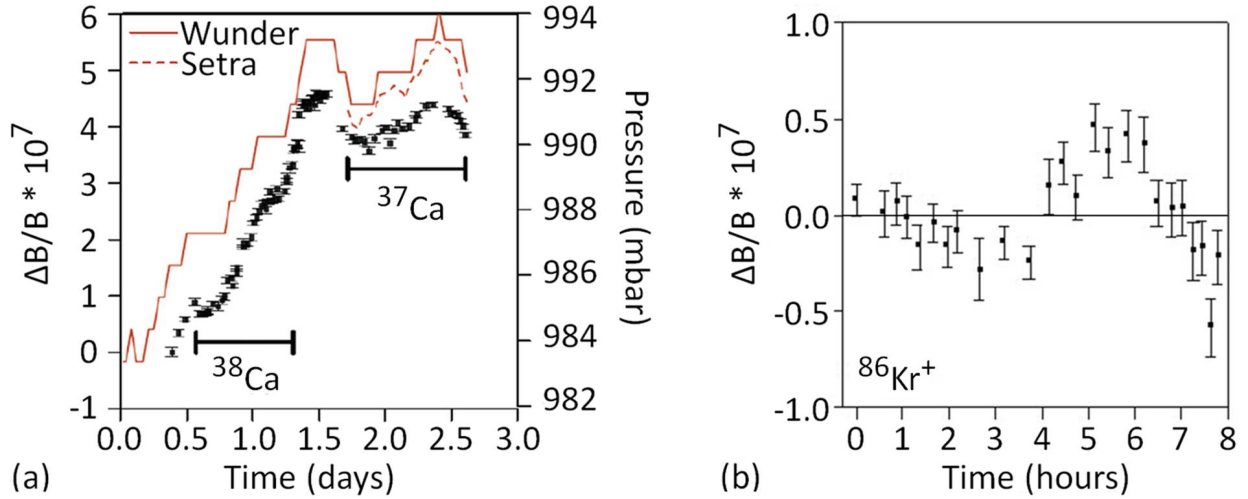


Figure 2.12: (a) Magnetic field drift of LEBIT's 9.4 T superconducting magnet during rare isotope measurements of ^{37}Ca and ^{38}Ca . The solid line (red) represents the atmospheric pressure data from a local weather station as reported by Weather Underground (Wunder) and the dashed line represents the pressure data recorded from a high-precision barometer (Setra) located at the NSCL. Note that $(\Delta B/B)/dp = 4.5 \times 10^{-8} \text{ mbar}^{-1}$. (b) Residual non-linear drift after stabilizing the pressure of the liquid helium bath of the superconducting magnet and subtracting out the linear magnetic field decay. (Note the change in scales between the two graphs.)

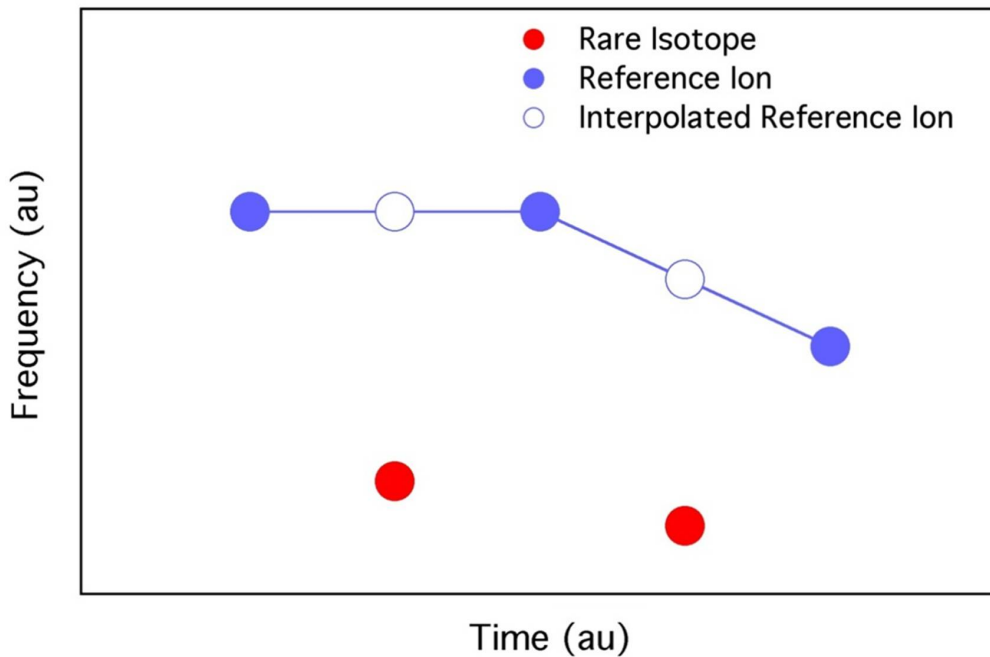


Figure 2.13: Cartoon showing how reference cyclotron frequency measurements (blue dots) are used to interpolate the strength of the magnetic field during a rare isotope cyclotron frequency measurement (red dots).

decided that high-precision mass measurements require a cyclotron frequency measurement with a reference ion (a well-known mass) be performed prior to and following a cyclotron frequency measurement of the ion of interest, no more than an hour apart from one another. In this scenario, the magnetic field can be interpolated from the reference measurements to the time when the cyclotron frequency of the ion of interest was measured as depicted in Fig. 2.13.

Chapter 3

First Direct Double-Beta Decay

Q -value Measurement of ^{82}Se

3.1 Motivation for Determining the ^{82}Se Double-Beta Decay Q -value

Interest in $\beta\beta$ decay has been increasing since the laboratory verification of the weak, but allowed, two-neutrino double-beta decay ($2\nu\beta\beta$ decay) of ^{82}Se [67]. Including laboratory, geochemical, and radiochemical experiments, twelve isotopes have been observed to undergo $2\nu\beta\beta$ decay: ^{48}Ca , ^{76}Ge , ^{82}Se , ^{96}Zr , ^{100}Mo , ^{116}Cd , ^{128}Te , ^{130}Te , ^{136}Xe , ^{150}Nd , ^{238}U , and double-electron capture in ^{130}Ba [68, 69]. With the exception of the unconfirmed claim in Ref. [70] for ^{76}Ge , $0\nu\beta\beta$ decay has yet to be observed. If $0\nu\beta\beta$ decay is confirmed, there would be evidence that the neutrino is a Majorana particle and that conservation of total lepton number is violated – a situation forbidden by the Standard Model of particle physics. It is therefore not surprising that there are a number of groups currently building large scale detectors all vying to be the first to unambiguously observe $0\nu\beta\beta$ decay.

The defining observable of $0\nu\beta\beta$ decay is a single peak in the electron sum-energy spectrum at the $\beta\beta$ decay Q -value, $Q_{\beta\beta}$. Hence, it is crucial to have an accurate and precise determination of $Q_{\beta\beta}$. The Q -value is also required to calculate the Phase Space Factor (PSF) of the decay. The effective Majorana neutrino mass, together with the corresponding PSF and Nuclear Matrix Element (NME) for a $0\nu\beta\beta$ decay candidate provide the necessary information to determine the $0\nu\beta\beta$ decay half-life, which is given by:

$$(T_{1/2}^{0\nu})^{-1} = G_{0\nu}(Q_{\beta\beta}^5, Z)|M_{0\nu}|^2(\langle m_{\beta\beta} \rangle/m_e)^2, \quad (3.1)$$

where $M_{0\nu}$ is the relevant NME, $\langle m_{\beta\beta} \rangle$ is the effective Majorana neutrino mass, m_e is the mass of the electron, and $G_{0\nu}$ is the PSF for the $0\nu\beta\beta$ decay, which is a function of $Q_{\beta\beta}^5$ and the nuclear charge, Z . Thus, to obtain an accurate estimation of the half-life sensitivity required to detect a given $\langle m_{\beta\beta} \rangle$, or conversely, to determine $\langle m_{\beta\beta} \rangle$ if the half-life is measured, the NME and especially the Q -value need to be known with sufficient precision.

An extensive campaign is currently underway to develop next-generation experiments to detect $0\nu\beta\beta$ decay in a number of candidate isotopes (see Ref. [71] for a recent review of planned experiments). The seven most developed and promising projects aimed to detect $0\nu\beta\beta$ decay include the GERmanium Detector Array (GERDA) and Majorana experiments which will probe for $0\nu\beta\beta$ decay with ^{76}Ge , the Super Neutrino Ettore Majorana Observatory (SuperNEMO) with ^{82}Se , the Cryogenic Underground Observatory for Rare Events (CUORE) with ^{130}Te , the Enriched Xenon Observatory (EXO) and the Kamioka Liquid scintillator AntiNeutrino Detector (KamLAND-Xe) with ^{136}Xe , and the Sudbury Neutrino Observatory (SNO+) with ^{150}Nd [71]. The SuperNEMO experiment is expected to provide an increase in sensitivity of three orders of magnitude over its predecessor, NEMO-III, and

is projected to reach a half-life sensitivity at the 90% confidence level of $1 - 2 \times 10^{26}$ years by observing 100-200 kg of ^{82}Se for five years [71, 72]. These experiments are currently, or are planning to reach sensitivities of an effective neutrino mass of tens of meV. At this sensitivity, not only does the probability increase for detecting $0\nu\beta\beta$ decay, but these experiments may also allow identification of the mass hierarchy of the three neutrino mass eigenstates [22].

To experimentally resolve the single $0\nu\beta\beta$ decay peak in the electron sum-energy spectrum above the tail of the $2\nu\beta\beta$ decay electron sum-energy distribution, a $Q_{\beta\beta}$ greater than 2 MeV is desired. In 2012, the LEBIT facility began a measurement campaign to determine the Q -values of the four (of the eleven) $0\nu\beta\beta$ decay candidates with Q -values greater than 2 MeV [22] that have not been measured via PTMS. The seven $0\nu\beta\beta$ decay candidates (with Q -values greater than 2 MeV) previously determined through measurements at PTMS facilities include: ^{76}Ge [24, 25, 26], ^{100}Mo [25], ^{110}Pd [23, 27], ^{116}Cd [28], ^{130}Te [28, 29, 30], ^{136}Xe [31, 32], and ^{150}Nd [33]. The LEBIT facility's $0\nu\beta\beta$ decay Q -value measurement campaign began with a new determination of the $\beta\beta$ decay Q -value of ^{48}Ca [46] and the first direct $\beta\beta$ decay Q -value measurement of ^{82}Se [73] (as part of this work) and ended with the $\beta\beta$ decay Q -value determination of ^{96}Zr [49]. During this time, the $\beta\beta$ decay Q -value of ^{124}Sn was determined directly via PTMS at SHIPTRAP [74].

The previous literature value for the $\beta\beta$ decay Q -value of ^{82}Se was published by the 2003 Atomic Mass Evaluation (AME2003) [75]. In the AME2003, the mass of each isotope was determined by evaluating the results of various experiments and a weighted average was calculated to obtain the respective mass values (the reader is referred to Ref. [75] for details). The mass of ^{82}Se was evaluated using the results of two high resolution mass spectrometer measurements [76, 77] and a $^{82}\text{Se}(p,t)^{80}\text{Se}$ reaction Q -value measurement [78]. The mass of ^{82}Kr was evaluated using the results of a PTMS measurement [79], the high

resolution mass spectrometer measurement from [76], and an experiment which reported the β decay scheme of ^{82}Br as determined through coincidence and direct measurements from an intermediate-image spectrometer and a conventional gamma-gamma coincidence scintillation spectrometer [80]. Using these mass data, AME2003 determined the $\beta\beta$ decay Q -value to be $Q_{\beta\beta} = 2996(2)$ keV. This level of precision is sufficiently precise for SuperNEMO which will rely on plastic scintillators to determine the energy of the emitted electrons with a resolution of $\Delta E/E \sim 8\text{-}10\%$ (FWHM) at $E = 1$ MeV [71]. Future experiments searching for $0\nu\beta\beta$ decay with ^{82}Se could improve energy resolution by utilizing large mass ZnSe bolometers which can currently achieve an energy resolution on the keV level [81]. If these detectors are utilized to search for $0\nu\beta\beta$ decay of ^{82}Se , a sub-keV uncertainty in the Q -value would be required to ensure that the detected peak is resultant from $0\nu\beta\beta$ decay and not background events. In addition, an improvement in the precision of the Q -value by an order of magnitude would further constrain the mass of the neutrino if $0\nu\beta\beta$ decay of ^{82}Se is observed.

3.2 Experimental Setup

The direct $Q_{\beta\beta}$ measurement of ^{82}Se was carried out at the NSCL using the LEBIT facility where the TIS was used as a source of the measured isotopes. One of the benefits of the TIS is that not only can stable noble and alkali ions be produced, but elements with high enough vapor pressures can be heated inside the oven, vaporized, and ionized with a discharge in noble gas mode. In this technique, a ceramic charge holder is filled with the desired element of interest and secured on both ends with a bit of glass wool before being inserted into the ion source chamber. Glass wool is convenient since it is rigid enough to contain

the desired element, but also porous enough to allow the vaporized element to escape into the ion source chamber. The vapor is then ionized in noble gas mode, and a buffer gas is utilized to facilitate multiplication of electrons from the filament. Using this technique, mass measurements can be performed on long-lived rare isotopes off-line, depending on the natural abundances of the isotopes of the element placed in the charge holder. This method was previously utilized to perform a mass measurement on ^{48}Ca [46], with a natural abundance of 0.187%, but it becomes more difficult to produce rare isotopes with smaller natural abundances using this method without obtaining isotopically enriched samples. This method was well suited for producing ^{82}Se and ^{82}Kr isotopes with natural abundances of 8.73% and 11.58%, respectively.

The plasma TIS was used to simultaneously produce ions of ^{82}Se and of the $\beta\beta$ decay daughter, ^{82}Kr . To produce the ions, the ceramic charge holder was filled with ~ 200 mg of granulated selenium and inserted into the oven of the TIS. The granulated selenium was then vaporized and some fraction was ionized. A helium support gas for the source was mixed with the proper amount of krypton to maintain a balance in the ratio of the number of ^{82}Kr and ^{82}Se ions produced within a factor of three. The extracted ion beam was guided through a RFQ mass filter to suppress the strong accompanying helium current before being deflected downstream by the quadrupole steerer to the beam cooler and buncher. The short low-emittance ion bunches produced by the beam cooler and buncher were then sent to the Penning trap [42]. On their path the ions were purified further by using the TOF mass filter [82], allowing only ion species with an $A/Q = 82$ to be dynamically captured in the trap.

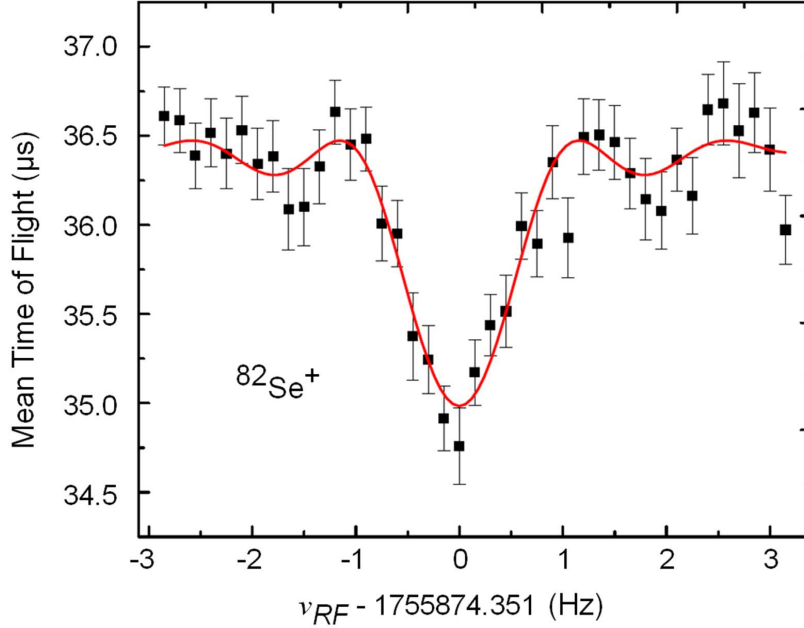


Figure 3.1: Example of a time-of-flight cyclotron resonance curve for $^{82}\text{Se}^+$. An excitation time of $T_{RF} = 750$ ms was used to obtain a resolving power of 2×10^6 . The results of fitting the theoretical line shape to the data is represented by the solid line (red).

3.3 Measurements

The measurement process for the determination of $Q_{\beta\beta}(^{82}\text{Se})$ consisted of alternating cyclotron frequency measurements of $^{82}\text{Kr}^+$ and $^{82}\text{Se}^+$. These measurements were performed in a series of four runs. The first run consisted of measurements using $T_{RF} = 500$ ms, but for increased precision, a $T_{RF} = 750$ ms was used for the final three runs. Each TOF resonance was the average of 25 to 40 scans over the respective frequency range with 41 trapping cycles per scan. A TOF resonance of $^{82}\text{Se}^+$ with $T_{RF} = 750$ ms is shown in Fig. 3.1. During the measurement process the number of ions in each pulse ejected from the buncher was limited using the appropriate accumulation time such that only an average of 2 ions per trapping cycle were recorded by the MCP, corresponding to < 7 ions in the trap at one time (assuming 30% detector efficiency). This was done to limit the number of contaminant ions produced via charge-exchange reactions with residual gas in the trap. Each resonance

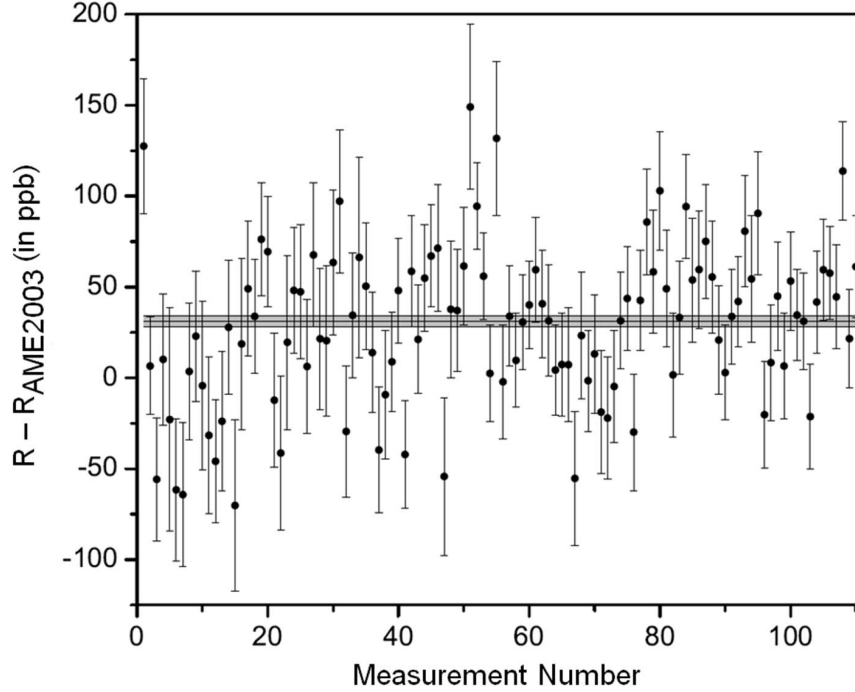


Figure 3.2: Difference between the cyclotron frequency ratio of $^{82}\text{Kr}^+$ to $^{82}\text{Se}^+$ and the ratio obtained from literature mass data [75]. The solid lines indicate the weighted average and the 1σ statistical uncertainty band.

consisted of ~ 500 - 3000 detected ions, depending on the number of scans per resonance and the beam current from the ion source. To determine ν_c , each resonance was fitted using the theoretical line shape described in Ref. [61]. The standard deviation of ν_c for each resonance was ~ 30 ppb (parts per billion).

Drifts in the magnetic field during the frequency ratio determination of $^{82}\text{Kr}^+$ to $^{82}\text{Se}^+$ were accounted for by linearly interpolating between the two cyclotron frequency measurements of $^{82}\text{Kr}^+$ bracketing each $^{82}\text{Se}^+$ measurement to obtain $\nu_c^{int}(^{82}\text{Kr}^+)$. This interpolated cyclotron frequency was used to obtain the frequency ratio $R = \nu_c^{int}(^{82}\text{Kr}^+)/\nu_c(^{82}\text{Se}^+)$. The values obtained from a total of 110 ratio determinations and their weighted average are shown in Fig. 3.2. The difference to the reference ratio, R_{AME2003} , was calculated using $R_{\text{AME2003}} = [m(^{82}\text{Kr}) - m_e]/[m(^{82}\text{Se}) - m_e]$ with the mass values from AME2003 [75].

3.4 Data Analysis

In preparation for, and during the measurement process, great care was taken to minimize possible systematic effects. By measuring mass doublets, contributions to the measurement uncertainty arising from mass dependent systematic effects due to frequency shifts, for example caused by field imperfections, are essentially removed. Nevertheless, prior to the measurements, imperfections of the trapping potential were carefully minimized by tuning the correction electrodes of the hyperbolic Penning trap according to the tuning procedure described in Ref. [83].

Any effect from non-linear magnetic field drifts are not accounted for in this data evaluation and are not mitigated by using a mass doublet. Therefore, the cyclotron frequency measurements of $^{82}\text{Kr}^+$ and $^{82}\text{Se}^+$ were alternated with a period of no greater than 1 hour. Based on an earlier study [15], this should lead to residual systematic effects of the cyclotron frequency ratio no greater than 1 ppb. This uncertainty was further minimized as the pressure in the cryostat was stabilized to 10 ppm (parts per million) during the measurements [65], resulting in an uncertainty well below 1 ppb. In addition, simultaneously trapped ions with a different m/q value can cause frequency shifts [84]. This effect was minimized by verifying that contaminant ions were never present at a level exceeding a few percent, low enough to not lead to a significant shift at the desired precision.

The weighted average of the ratios for the individual runs and the corresponding statistical uncertainty are listed in Table 3.1 together with the weighted average R_{LEBIT} of all results and the value R_{AME2003} calculated using the mass values of ^{82}Kr and ^{82}Se from AME2003 [75]. Through evaluation of the entire data set, with statistical errors as obtained from fitting the theoretical lineshapes to the measured cyclotron resonance curves, a Birge

Table 3.1: Average cyclotron frequency ratios $R_{run} = \nu_c^{int}(^{82}\text{Kr}^+)/\nu_c(^{82}\text{Se}^+)$ with their statistical errors as obtained in four separate runs with N frequency ratio measurements performed in each run. Also given is the final weighted average R_{LEBIT} with its statistical and final uncertainty and the ratio calculated using the mass values from AME2003 [75].

Run	N	R_{run}
1	53	1.000 039 285(5)
2	2	1.000 039 30(2)
3	7	1.000 039 29(1)
4	48	1.000 039 290(4)
R_{LEBIT}		1.000 039 290(4)(5)
R_{AME2003}		1.000 039 26(3)

ratio [85] of 1.27(5) was determined. While close to unity, the significant deviation from unity indicates the presence of residual systematic effects at the 0.8 ppb level not discovered in the individual measurements or in the tests for systematic effects performed. Therefore, to account for these non-statistical contributions, the statistical uncertainty of the weighted average R_{LEBIT} for all data was multiplied by the value of the Birge ratio. Both the statistical and total uncertainty for R_{LEBIT} are given in Table 3.1.

The $\beta\beta$ decay Q -value was determined from the mass difference between the mother nuclide of mass m_m and daughter nuclide of mass m_d through:

$$\frac{Q_{\beta\beta}}{c^2} = m_m - m_d = (R - 1)(m_d - m_e), \quad (3.2)$$

where R is the cyclotron frequency ratio between the singly charged ions of the daughter and mother nuclides, c is the speed of light, and m_e accounts for the missing electron mass of singly charged ions used in the measurement. Using the final frequency ratio R_{LEBIT} and the AME2003 mass for ^{82}Kr , the Q -value was calculated to be $Q_{\beta\beta} = 2\,997.9(3)$ keV. The new LEBIT Q -value is nearly an order of magnitude more precise than the previous value published in AME2003 [75] and is a dramatic improvement to one of the ingredients needed

for a better determination of the half-life limit for $0\nu\beta\beta$ decay in ^{82}Se .

3.5 Discussion of Results and Conclusion

By using Penning trap mass spectrometry, the first direct Q -value measurement of ^{82}Se $\beta\beta$ decay was performed by measuring the cyclotron frequency ratio between singly charged ions of ^{82}Se and the $\beta\beta$ decay daughter, ^{82}Kr . The result, $Q_{\beta\beta} = 2997.9(3)$ keV, is nearly an order of magnitude more precise than the previous value published in AME2003 [75]. Following the procedure in Ref. [86] and using the new Q -value, the PSF for the $0\nu\beta\beta$ decay mode of ^{82}Se was calculated to be $G_{0\nu} = 2.848(1) \times 10^{-14} \text{ yr}^{-1}$, where the uncertainty has also been improved by nearly an order of magnitude. With a corrected shell model NME calculation [73] and the current upper limits of $\langle m_{\beta\beta} \rangle = 140 - 380$ meV from the EXO-200 experiment [87] a lower limit range for the ^{82}Se $0\nu\beta\beta$ decay half-life of $5.0 \times 10^{24} - 3.7 \times 10^{25}$ years was obtained. Assuming SuperNEMO achieves its projected sensitivity at the 90% confidence level of $1 - 2 \times 10^{26}$ years, an effective neutrino mass as low as 60-85 meV could be detected.

Chapter 4

Development of a High-Precision

Magnetometer for the LEBIT Facility

To increase the precision of high-precision mass measurements at the LEBIT facility (and other PTMS facilities) changes in the magnetic field need to be measured to a precision better than the mass measurements, which can be better than 1 part in 10^8 . A commercial Nuclear Magnetic Resonance (NMR) magnetometer could be installed, but they are currently limited to resolutions of about 1 part in 10^7 . It is also advantageous to develop a magnetometer that is radiation hard for high-precision magnetic field monitoring in the presence of high levels of ionizing radiation where NMR probes cannot be used.

The development of the magnetometer required a multi-disciplinary approach including ion trap physics, mechanical and electrical engineering, software development, chemistry, and advanced microscopy. The main component of the magnetometer, a Penning trap, needed to be optimized not only to achieve high-precision, but also engineered for ease of assembly and installation. In addition, the magnetometer had to be installed in a superconducting

magnet to demonstrate that it could indeed detect changes in the magnetic field strength to a relative precision of 1 part in 10^8 .

4.1 Motivation for a High-Precision Magnetometer

The LEBIT facility, and similar PTMS facilities, rely on mass measurements of a well-known ion species to calibrate the magnetic field before and after each rare isotope cyclotron frequency TOF resonance. This technique has worked well, but there are a couple drawbacks to the reference measurement interpolation method. First, valuable beam time is wasted on performing reference measurements. Second, this method does not account for non-linear fluctuations in the magnetic field strength of the superconducting magnet that may occur on time scales shorter than the time required to perform a TOF cyclotron frequency measurement, which is typically on the order of 10 minutes for a reference measurement. For a cyclotron frequency measurement of rare isotopes, however, the time required to obtain a TOF resonance is determined by the rate at which the rare isotope is delivered to the Penning trap. If non-linear magnetic field fluctuations are present, a broadening and shifting of the TOF resonance curve could occur for the cyclotron frequency measurements of the more exotic rare isotopes with longer measurement times. The non-linearity of the magnetic field thus presents a limitation on the precision and feasibility of a measurement when pushing the limits of mass measurements to extremely rare isotopes. If the strength of the magnetic field could be determined by some other method simultaneous to a rare isotope frequency measurement, more precise mass measurements of the most exotic rare isotopes measurable by PTMS could be obtained.

Measuring short-term fluctuations of the magnetic field without performing reference

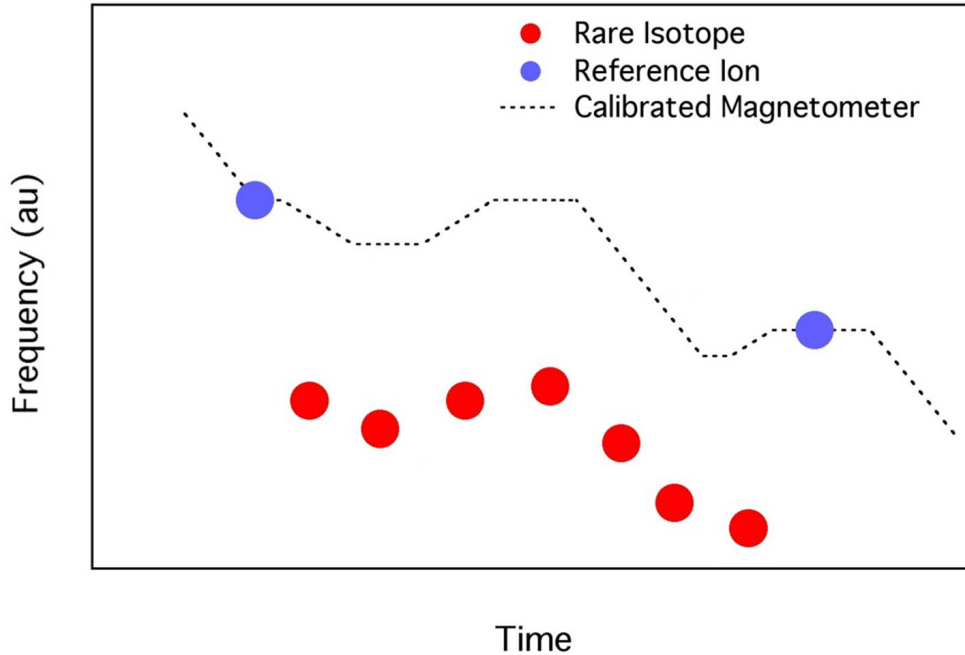


Figure 4.1: Cartoon showing how two reference cyclotron frequency measurements (blue dots) are used to calibrate a magnetometer that can track short-term fluctuations in the magnetic field allowing for either a longer rare isotope frequency measurement time, or as shown, increase the number of rare isotope frequency measurements (red dots).

measurements between (or during) rare isotope measurements (as depicted in Fig. 4.1) would allow the LEBIT facility, and similar PTMS facilities, to increase efficiency. For less exotic rare isotopes, more measurements could be performed resulting in a reduced uncertainty in the measurement with increased statistics. With a greater efficiency, less time would be necessary to reach a given precision and measurements of more rare isotope species could be performed during a given beam time, increasing the LEBIT facility's scientific output. Finally, by continuously monitoring the magnetic field, the precision of measurements of extremely rare isotopes could be improved. Therefore, a novel high-precision magnetometer was designed, built, and tested that will be installed in the LEBIT facility's 9.4 T superconducting magnet.

4.2 Magnetometer Concept and Design Requirements

The idea behind the high-precision magnetometer is to continuously monitor magnetic field fluctuations by monitoring the cyclotron frequency of a reference ion in a miniature Penning trap (MiniTrap) installed adjacent to the LEBIT facility's high-precision measurement trap in the bore of the 9.4 T superconducting magnet. Ideally, the magnetic field would be measured by the magnetometer at both the same time and location as the rare isotope measurement, however, this was not thought to be possible. The time requirement can be satisfied to within a second or two, however it would be impossible to physically locate the magnetometer at the center of the Penning trap for obvious reasons. Therefore, the magnetometer needs to be located as close as possible to the measurement trap since changes in the magnetic field should be consistent throughout the homogeneous region of the magnetic field. In this scenario, a simultaneous measurement of a reference ion in the measurement trap can be used to calibrate the magnetometer, then the magnetometer will track global changes in the magnetic field (as shown in Fig. 4.1).

The main requirement that, in part, makes the design of the MiniTrap difficult is the location requirement – the magnetometer needs to be installed directly adjacent to the measurement trap where it must fit within the existing electrode structure in the bore of the magnet. A small annular region located adjacent to and just downstream of the hyperbolic measurement trap, as shown in Fig. 4.2, is available for installation of the magnetometer. The annular region measures 8.9 cm in length and has inner and outer diameters of 2.4 cm and 7.3 cm, respectively. The MiniTrap electrode structures must fit within an enclosure no larger than that annular region.

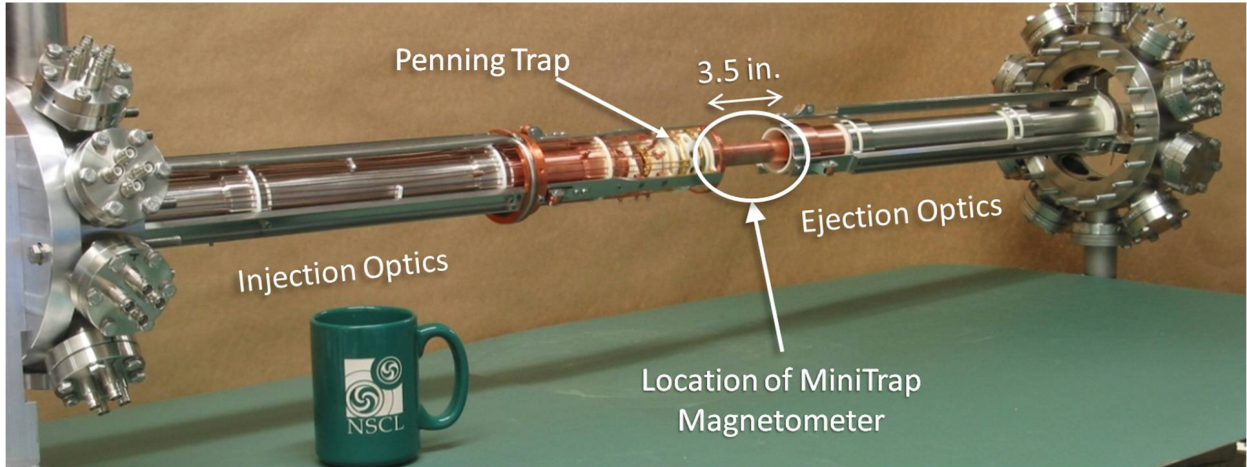


Figure 4.2: Location of the magnetometer depicted in an image of the Penning trap along with injection and ejection optics shown removed from the bore of LEBIT’s solenoidal 9.4 T superconducting magnet.

4.3 Technical Development of the Magnetometer

Two methods are used in PTMS to determine cyclotron frequencies, and thus masses, of ions in a Penning trap. The first is the TOF-ICR method, a destructive technique, and is utilized at the LEBIT facility to perform high-precision mass measurements as previously discussed. The second method is called the Fourier Transform – Ion Cyclotron Resonance (FT-ICR) technique, a non-destructive technique. Instead of detecting ions ejected from the trap with an MCP detector and recording their TOF, the FT-ICR technique can be implemented to determine the cyclotron frequency directly in the Penning trap by picking up a signal induced by the ions’ motion on detection electrodes. The latter method was chosen for the MiniTrap since it allows the magnetometer to be self-contained. Because the FT-ICR technique had never been utilized at the LEBIT facility, initial tests required development work to demonstrate this technique with the LEBIT hyperbolic trap.

Another aspect of the MiniTrap that required technical development was the production method of the reference ions for which the cyclotron frequency would be measured. It was

determined that electron-impact ionization of background gas would be the most convenient technique. In this method an electron beam is used to remove an electron from an atom or molecule, thus ionizing it, so that the ion can be trapped and manipulated with the electromagnetic fields in the MiniTrap.

4.3.1 Fourier Transform – Ion Cyclotron Resonance (FT-ICR)

The FT-ICR technique has been utilized for many years and is very well understood (see ref. [88] for a review of FT-ICR principles), therefore, I will only cover the basics necessary for the development of the MiniTrap. FT-ICR operates on the principle of electrostatic induction where a charge located near the surface of a conductor creates an image charge on the conductor. When an ion oscillates near the surface of the conductor, the image charge also oscillates creating an oscillating image current. A schematic representation of the technique is shown in Fig. 4.3. To detect the image current, ions first need to be confined by a Penning trap in the presence of a strong magnetic field. Once confined, the radial motions of the ions need to be excited, thus coalescing the trapped ions into a bunch [60], by applying an azimuthal RF dipole electromagnetic field. This is accomplished by applying two RF signals at the same frequency near the frequency of the ions' radial motion, but 180 degrees out of phase, to two excitation electrodes opposite one another (shown in Fig. 4.3). The ion bunch, as it undergoes its radial motion in the plane perpendicular to the magnetic field, induces an image current on pickup electrodes, usually located on the ring segments of the Penning trap. The induced image current from two detection electrodes, located opposite one another, is then amplified by a low noise differential amplifier and subsequently analyzed with a Fast Fourier Transform (FFT) algorithm to transform the amplified time domain signal into a frequency domain signal, resulting in a single peak at the frequency of the radial motion.

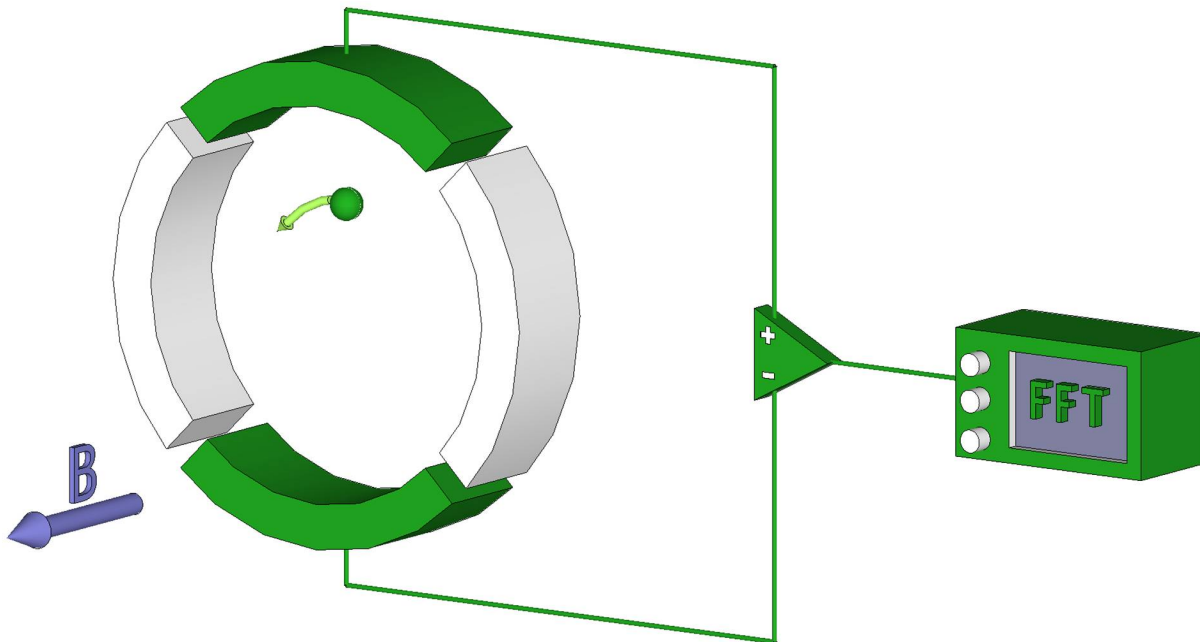


Figure 4.3: Schematic representation of the basic FT-ICR technique where ions are driven by excitation electrodes (white) and induce an image current in the detection electrodes (green), which is then amplified and detected through FFT Fourier analysis. (Note that the endcap electrodes of the Penning trap that provide axial confinement in the direction of the magnetic field are not shown.)

This technique, known as broadband FT-ICR, is widely used in analytical chemistry and allows a wide range of masses to be detected [88]. One limitation to this technique, however, is that it requires many moving ions in order to produce a signal large enough to detect above the background noise created by surrounding electronic equipment and the thermal noise of the electronics necessary to transfer and amplify the signal [60].

To achieve the greatest precision, the number of trapped ions should actually be minimized. This is necessary to keep the ion bunch coherent and to minimize shifts of the cyclotron frequency due to image charges [89] and shot-to-shot variations in the number of trapped ions [84]. With fewer numbers of trapped ions, the image current induced on the detection electrodes is reduced to the point where the ion's signal cannot be detected above background noise. In addition, a large peak in the frequency spectrum of the FFT results

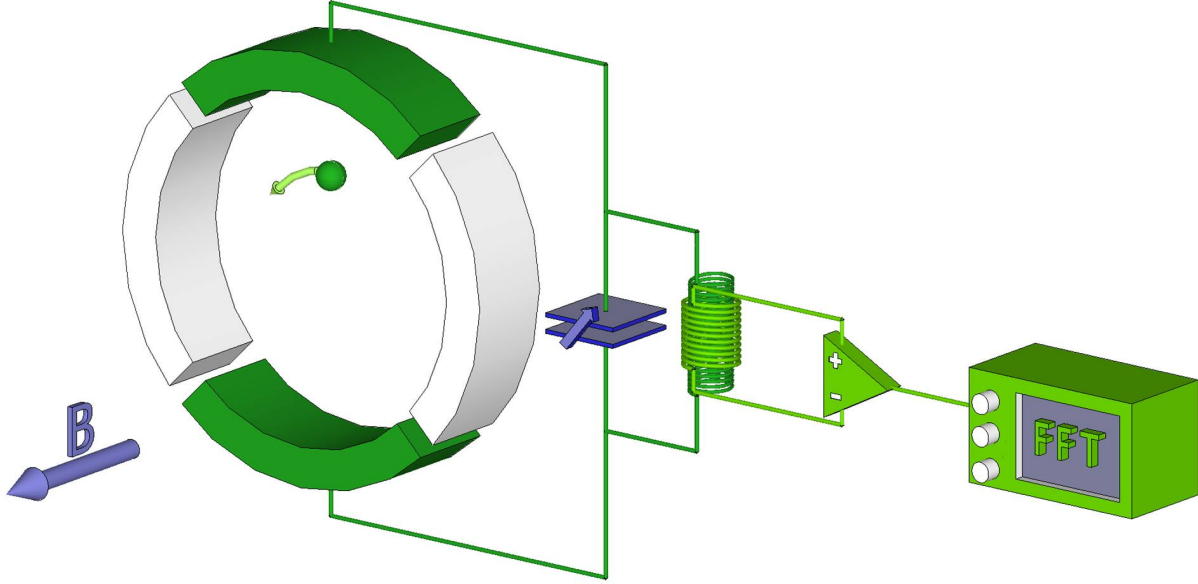


Figure 4.4: Schematic representation of the narrow-band FT-ICR technique which includes a variable capacitor (blue) and inductor coil (dark green) to create a resonant circuit. The pickup coil (light green) is used to decouple the resonant circuit to reduce parasitic capacitance. Again, the endcap electrodes of the Penning trap are not shown. (In practice, the primary inductor coil is center-tapped and grounded to alleviate charge build-up on the detection electrodes.)

in a better fit and thus a lower uncertainty in the center frequency of the resonance peak. It is thus beneficial to maximize the voltage signal delivered to the pre-amplifier by utilizing a narrow-band FT-ICR detection method depicted in Fig. 4.4. The narrow-band FT-ICR detection method requires the installation of an inductor, with inductance L_{coil} , and a variable capacitor in parallel to the detection electrodes to create an LCR resonant circuit, with a resonant frequency, ω_o , equal to the radial frequency of the ion's motion. This allows the voltage signal produced by the image current to be amplified by the magnitude of the total impedance of the LCR circuit in resonance, R_o , which is given by:

$$R_o = \frac{Q}{\omega_o C} = Q\omega_o L, \quad (4.1)$$

where Q is the quality factor, or Q factor, of the resonant circuit and is defined by:

$$Q \equiv \frac{\omega_o}{\Delta\omega}, \quad (4.2)$$

and of course,

$$\omega_o = \frac{1}{\sqrt{LC}}. \quad (4.3)$$

Note that $\Delta\omega$ corresponds to the frequency width of the resonance where the amplitude is equal to $1/\sqrt{2}$ of the maximum, L denotes the value of L_{coil} plus the parasitic inductance of the circuit, and C denotes the total capacitance of the circuit (including parasitic capacitance). It is important to maximize the Q factor of the circuit to maximize the amplification of the signal, which leads to an increase of the signal-to-noise ratio by \sqrt{Q} [90].

To maximize the Q factor of the resonant circuit, several things need to be optimized. First, a larger circuit capacitance generally leads to a reduction of the Q factor. It is thus important to build the trap electrodes such that capacitance between the electrodes is minimized. Second, wiring of the trap electrodes to the resonant circuit must be done to not only minimize capacitance, but also to minimize the background noise picked up by the wires. Also, the inductor should be fabricated with an inductance only slightly smaller than that needed such a that minimal capacitance is required by the variable capacitor used to tune the resonant frequency of the circuit to match the cyclotron frequency of the ions' radial motion. Finally, to further minimize parasitic capacitance, a pickup coil wrapped around the primary inductor should be used to decouple the resonant circuit from the pre-amplifier. (When using the pickup coil, the primary coil should have a center-tap at ground to eliminate charge buildup on the detection electrodes.) The resonant circuit and the pre-amplifier should be placed as close as possible to the detection electrodes (ideally adjacent

to the trap in the bore of the superconducting magnet) to reduce the pick-up of background noise and minimize parasitic capacitance.

It is also important to carefully choose the mass of the reference ion to increase the precision of the magnetometer. Consider that the MiniTrap measures an ion's cyclotron frequency, which is proportional to the magnetic field strength, therefore:

$$\left. \frac{\Delta\omega_c}{\omega_c} \right|_{\Delta B} = \frac{\Delta B}{B}. \quad (4.4)$$

This expression indicates that for a given frequency resolution, to decrease the uncertainty in a magnetic field measurement, one should measure an ion with as large a cyclotron frequency as possible, i.e. lighter masses. However, there is a practical limit to how high in frequency, and thus how light an ion, one can measure. The main limitation comes from the LCR circuit required for narrow-band detection, where the resonant frequency of the circuit is limited by the total capacitance and parasitic inductance of the detection circuit. In addition, to obtain a reasonable Q factor, L_{coil} should be non-negligible.

For the implementation of the MiniTrap, the variable capacitor, primary and secondary inductor, along with the pre-amplifier were located outside of the superconducting magnet for simplicity and ease of testing. Unfortunately, this configuration increases the total capacitance and parasitic inductance of the detection circuit. Even with this limitation, an ion species with a mass as small as 2 u, such as H_2^+ (corresponding to a frequency of ~ 72 MHz in a 9.4 T magnetic field), should be within reach.

4.3.2 Ion Production

A convenient way to ionize atoms and molecules in a small volume, as required by the space constraints of the MiniTrap, is to use either a Field Emission Point (FEP), or a thermionic emitter. FEPs are composed of a rod of conducting material that has been electrochemically etched to produce a sharp tip with a radius as small as a few tens of nanometers. The application of a large potential to the tip of an FEP results in a large local electric field that enables electrons in the conduction band to overcome the potential barrier at the surface of the tip and be emitted into vacuum (for a full theoretical description of field emission, see Ref. [91]). One of the advantages of using an FEP is that it is a cold emitter, i.e. heat is not needed to produce the electron beam. A thermionic emitter is composed of a metallic filament that is heated by passing a current through it, thus imparting thermal energy to the conduction electrons enabling them to overcome the potential barrier. Initially it was determined that the low operating temperatures of FEPs was an advantage over thermionic emitters, therefore, considerable effort was required to develop a fabrication technique for producing FEPs at the NSCL for the MiniTrap.

A variety of techniques have been used over the years to produce FEPs (see ref. [92] for a basic review of the various techniques). Ultimately, a variation of the lamella drop-off technique [93, 94] and the floating layer technique [95, 96] was developed by the LEBIT team and implemented as described in detail in ref. [97]. In Fig. 4.5 an optical image and two Scanning Electron Microscope (SEM) images at different magnifications of an FEP produced by the LEBIT team are shown. The imaging was found to be necessary to determine the likelihood of a tip being “good” before testing, since the testing procedure ranged in time from several hours to several days for each FEP.

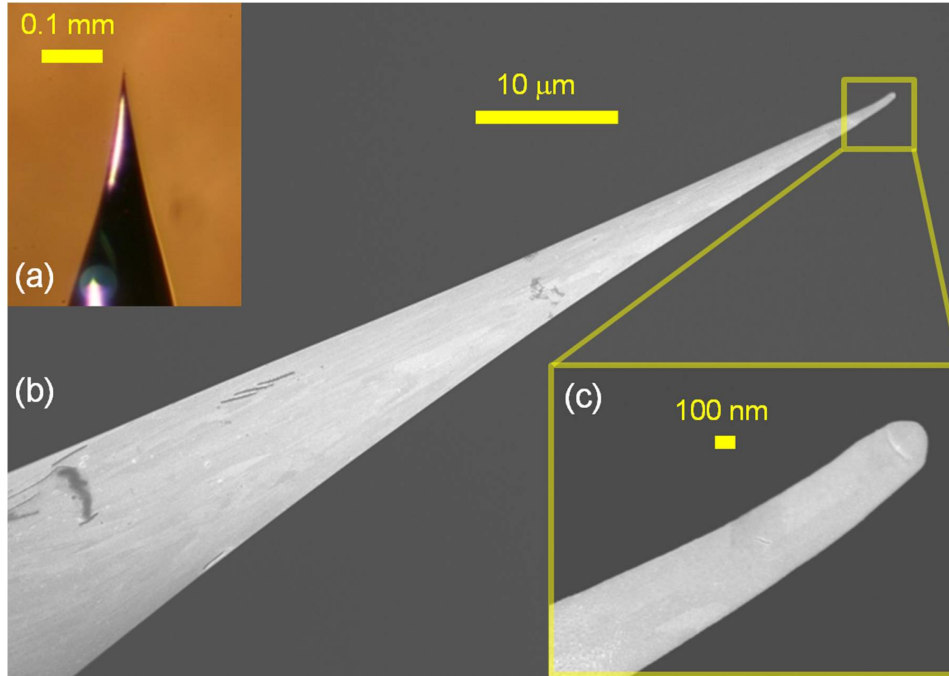


Figure 4.5: Images of a field emission point fabricated at the National Superconducting Cyclotron Laboratory as imaged by (a) an optical microscope, (b) a Scanning Electron Microscope (SEM) at $1800\times$ magnification, and (c) an SEM at $37,000\times$ magnification.

After testing nearly one hundred FEPs, only a handful were found to emit an electron beam current stable enough (within 10% of the nominal current) to be used in the MiniTrap. Tungsten filament thermionic emitters from Kimball Physics Inc. (model number ES-020) were tested to compare electron beam stability to the FEPs and to determine if thermionic emitters would heat the vacuum chamber enough to cause problems when producing several nanoamps of electron beam current. The thermionic emitters outperformed the FEPs with regards to electron beam current stability with fluctuations of only 5% of the nominal current. Also, tests of the thermionic emitters indicated that the ambient temperature increased by no more than 10 degrees Celsius (at several nanoamps of electron beam current) and could be tolerated by the MiniTrap. For testing FT-ICR with the LEBIT trap, FEPs were experimented with to ionize background gas, but ultimately, it was decided that the stability of the thermionic emitters was more beneficial to the precision and reliability of the MiniTrap.

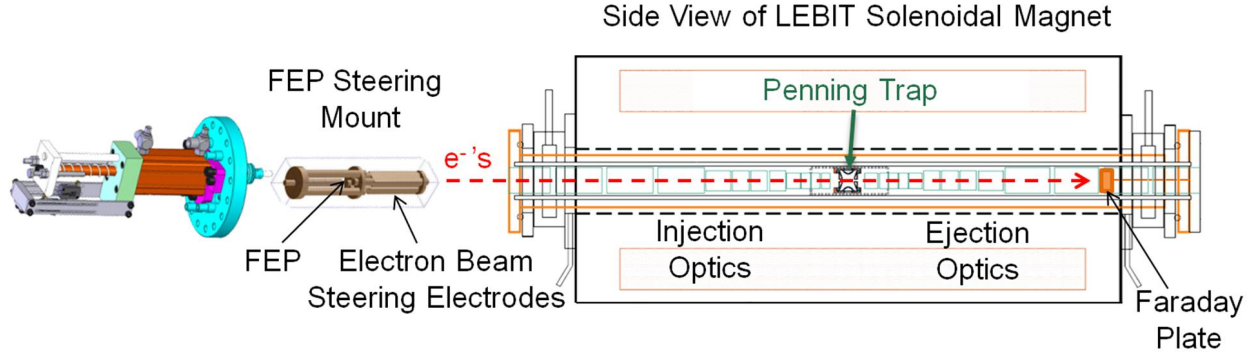


Figure 4.6: Schematic of the ion production test setup using the LEBIT 9.4 T superconducting magnet. The electron beam created by the FEP passes through a beam steerer that can block the electron beam from passing through the Penning trap and being collected on a Faraday plate. (The turbo and roughing pumps located on the ejection side of the magnet are not shown in the figure.)

4.3.3 Testing Ion Production and FT-ICR Techniques in the LEBIT Penning Trap

Once a good FEP tip was fabricated and found to provide a reproducible electron beam current, the ion production method was tested in the LEBIT 9.4 T superconducting magnet. This was convenient at the time, since the LEBIT beam line had yet to be assembled after the move to the new stopped beam area leaving the LEBIT magnet available. The setup consisted of the superconducting magnet which was pumped down to a pressure below a few 10^{-7} mbar using a turbo pump coupled to a roughing pump. On the ejection side of the magnet, a Faraday plate was mounted to measure the current of the electron beam emitted from the FEP that was produced on the far side of the magnet after passing through the Penning trap. To support and locate the FEP on the injection side of the magnet I designed, optimized (with simulations in SIMION), and fabricated an FEP steering mount which also allowed the electron beam to be blocked during a cyclotron frequency measurement. A schematic of the setup for testing ion production in the LEBIT magnet is shown in Fig. 4.6.

When installing the FEP, care had to be taken, as it needed to be aligned with a 1 mm hole in the extraction electrode through which electrons could pass to the steering section. The steering section was used to direct the beam away from or through a small slit at the end of the steering section to allow the beam to be either blocked or sent through to the Penning trap while keeping the FEP in a constant emitting mode. To produce the electron beam the FEP was first biased to -100 V and an extraction electrode, located just a few mm downstream of the FEP, was adjusted to a potential large enough to produce electron field emission. The voltage of the extraction electrode was adjusted with a LabVIEW controlled PID loop to stabilize the electron beam current. When the beam was blocked, the electron beam current was picked up by the electrodes forming the slit at the end of the steering section and measured by a Keithley picoammeter. The Faraday plate on the ejection side of the Penning trap measured the electron beam current that had successfully passed through the FEP steerer mount and the Penning trap. This provided both verification that the electron beam was properly aligned and measurement of the actual electron beam current required to ionize the background gas.

The sequence of events for performing an FT-ICR measurement in the LEBIT trap consisted of first allowing the electron beam, at a stabilized current and at an energy of 100 eV, to pass through the closed Penning trap (with between a few to 40 V on the endcaps and the ring segments held at ground potential) for a given period of time (generally 1 second for an electron beam current of several nanoamps). As the electron beam passed through the beam line some of the background gas became ionized through electron-impact ionization and ions created within the potential well of the Penning trap were confined. Once confined, excitation and detection of the trapped ions was performed.

Before trying to excite radial ion motion, self-excited magnetron motion was detected in

the LEBIT hyperbolic Penning trap using the broadband FT-ICR detection scheme. (Here, the self-excited magnetron motion is referred to as the phenomenon of a random cloud of ions in a Penning trap coalescing themselves into a bunch through electromagnetic interactions between the ions and the induced image charges on the ring segments of the Penning trap.) In order to produce a self-excited magnetron signal, the LEBIT magnet bore was first pumped down to below 5×10^{-7} mbar. The FEP steerer was then used to allow an electron beam current of a few nanoamps to pass through the Penning trap for 1 second. After waiting several seconds, the signal from the pre-amplifier was then acquired and analyzed using the LabVIEW-based MiniTrap Control System (MTCS) which allowed for the automation of an FT-ICR measurement and is described in Appendix B. Because the magnetron motion of ions in a Penning trap is unbound [98], the ions migrate outward from the center of the trap closer to the detection electrodes where an increased image current will be induced. Waiting several seconds after ionizing the background gas was, therefore, necessary to obtain a strong FFT signal. An FFT resonance of self-excited magnetron motion is shown in Fig. 4.7.

Detection of the reduced cyclotron motion at ω_+ , the largest frequency of the three eigenmotions, is necessary since it is the only eigenfrequency largely proportional to the magnetic field. Before detecting reduced cyclotron motion, the methods of exciting magnetron motion with both sweep and pulsed excitations (see [88] for technical details) were investigated. Testing both excitation methods was necessary because reduced cyclotron motion does not self-cohere similar to magnetron motion, not to mention ω_+ is highly mass dependent and it was unclear what residual gas species were being ionized and detected in the Penning trap through their magnetron motion. Experimenting with not only excitations of a fixed frequency and amplitude to drive the magnetron motion, but also with a frequency sweep signal at a fixed amplitude, enabled a broad frequency range to be probed to search for and

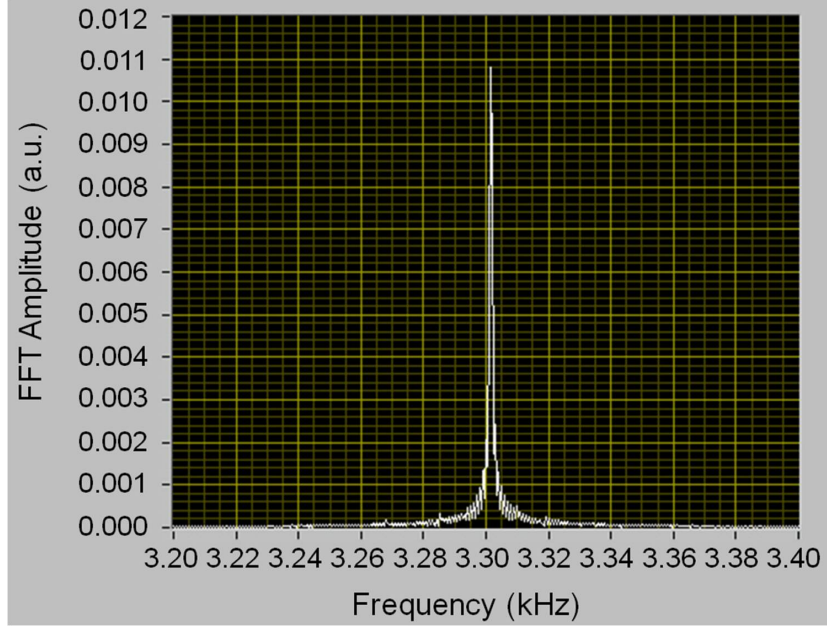


Figure 4.7: An FFT resonance of self-excited magnetron motion with trapped ions in a 40 V potential well.

identify ion species confined in the trap.

The frequency sweep excitation was used to identify ion species in the Penning trap using the axial detection method of FT-ICR. Since the axial frequency is related to an ion's mass through Eqn. 2.4, this method allowed identification of the mass of the ion species by determining ω_z . (Note that this method was convenient, since the frequency range to probe the axial motion of the ions is generally an order of magnitude smaller than that for cyclotron motion.) To probe for axial motion, the ions axial motion was excited with a sweep signal applied to the one of the endcaps of the hyperbolic trap while the pre-amplifier was connected directly to the other endcap (the broadband FT-ICR axial detection configuration). The ring and correction electrodes were then negatively biased to create the proper trapping potential (with the endcap electrodes at ground potential). Using a trapping potential of 40 V, two resonances were observed and are shown in Fig. 4.8. Analysis of the peaks indicated that the peak on the left resulted from the axial motion of H_3O^+ , while the peak on the right

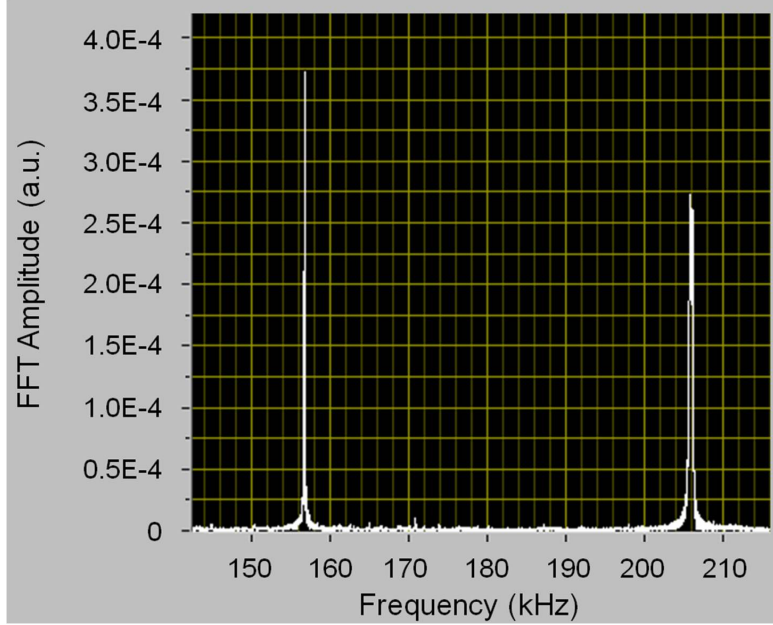


Figure 4.8: FFT resonances of two different ion species in the trap using the broadband axial detection method. Both ions were excited simultaneously using a sweep excitation applied to one endcap, while the image current was picked up on the other endcap. The peak on the left was identified as H_3O^+ and the peak on the right was identified as HO_2^+ .

resulted from the axial motion of HO_2^+ , at masses of 19 u and 33 u, respectively. Once the ion species were identified, it was fairly easy to obtain the resonance shown in Fig. 4.9 for the reduced cyclotron motion of H_3O^+ .

After successfully exciting and detecting ω_+ using the LEBIT hyperbolic trap, the MTCS was set up to monitor the magnetic field by performing ω_+ measurements repeatedly with a cycle time of ~ 10 seconds. The reduced cyclotron frequency was monitored for ~ 9 hours to determine the drift of the magnetic field and an approximate relative precision that could be obtained. The results of this monitoring process using the LEBIT trap are shown in Fig. 4.10 where each data point is the average of 10 reduced cyclotron frequency measurements, and the error bars represent the 1σ uncertainty in the distribution of those 10 data points.

The monitoring process revealed a drift in the magnetic field with a decay rate of $(\Delta B/B)/dt = -2.5(1) \times 10^{-8} \text{ hr}^{-1}$ which is close to the value of the drift obtained previ-

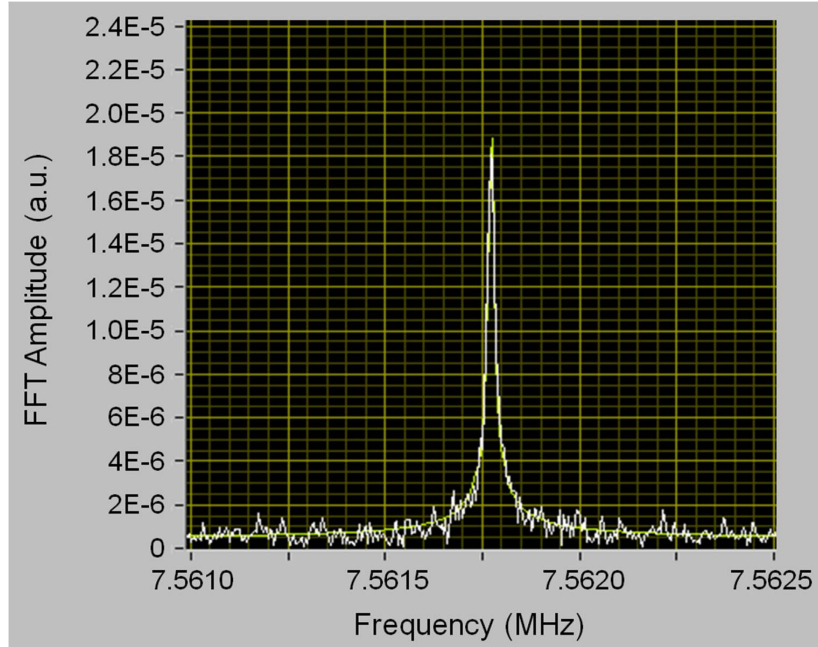


Figure 4.9: An FFT resonance of reduced cyclotron motion of an H_3O^+ ion bunch composed of ~ 2000 ions. The resonance has a full-width half-maximum of 5 Hz and a signal to noise ratio greater than 20.

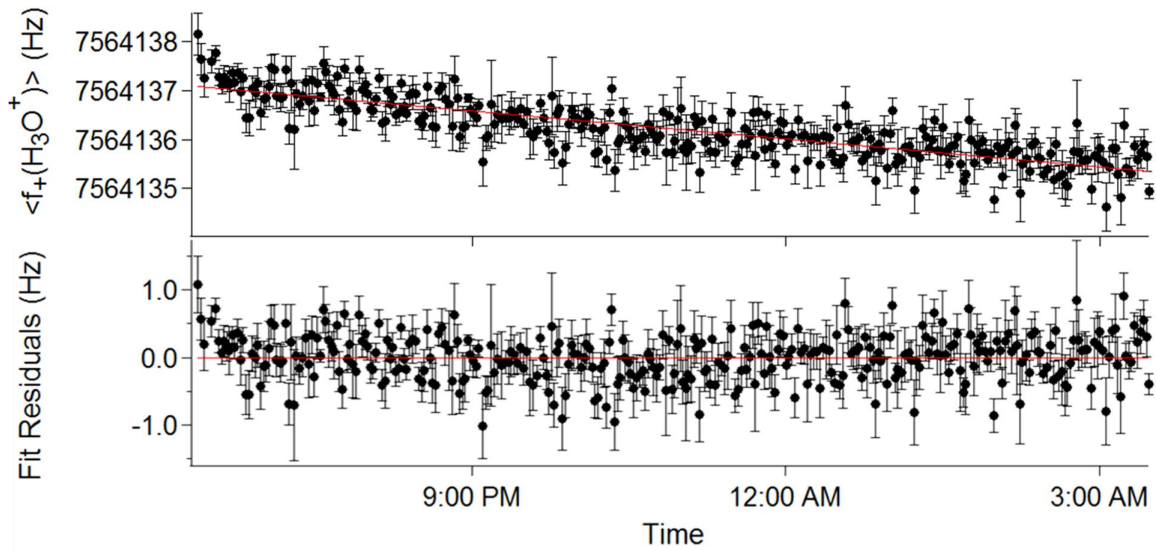


Figure 4.10: Results of the FT-ICR reduced cyclotron frequency monitoring process in the LEBIT magnet showing the average $f_+(\text{H}_3\text{O}^+)$ measurements and fit residuals as a function of time recorded during the course of ~ 9 hours. Each data point is the average of 10 frequency measurements where the error bars correspond to the 1σ uncertainty associated with the distribution of those 10 measurements. The solid lines (red) are the best linear fits to the data. The standard deviation of the fit residuals was determined to be 0.35 Hz corresponding to a relative precision of $\sim 5 \times 10^{-8}$ for the entire data set.

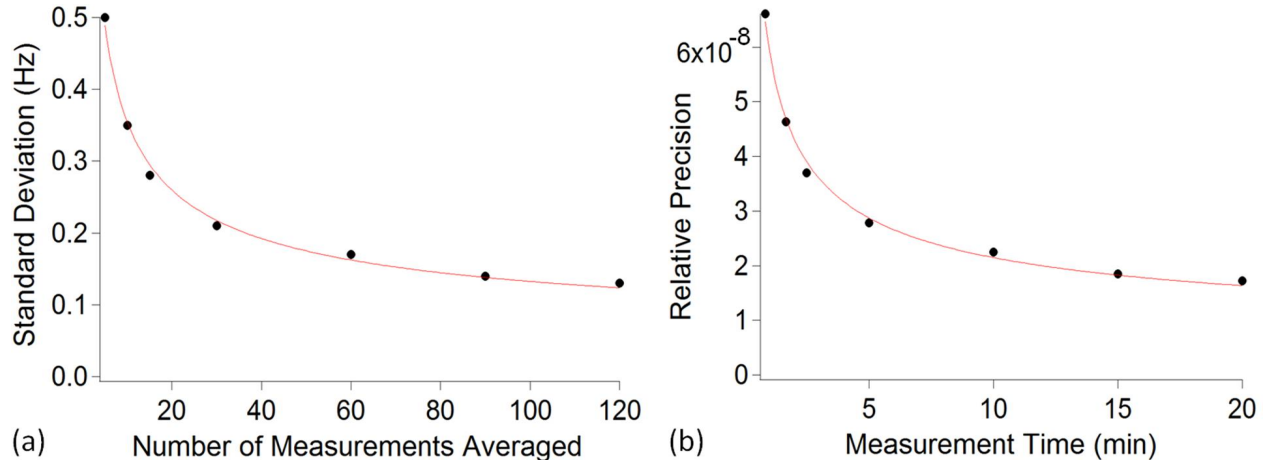


Figure 4.11: Results of the precision obtained during the reduced cyclotron frequency monitoring process in the LEBIT hyperbolic trap where in (a) the standard deviation of the entire data set is given when each frequency measurement is the average of a given number of measurements and (b) is a plot of the same data but indicates the measurement time necessary to achieve a given relative precision (assuming 10 seconds per measurement). The solid line (red) in each graph is the best fit to a square root power law which illustrates the statistical behavior of increasing the precision by the square root of the number of individual measurements averaged for a frequency measurement.

ously of $(\Delta B/B)/dt \approx -8 \times 10^{-8} \text{ hr}^{-1}$ through TOF-ICR measurements [65]. The standard deviation of the fit residuals suggests that the relative precision of the monitor is $\sim 5 \times 10^{-8}$ when averaging 10 individual measurements per each frequency measurement. To improve the precision of a frequency measurement, a greater number of individual measurements could be averaged, where the standard deviation should decrease by the square root of the number of measurements. This increase in precision is illustrated in Fig. 4.11 where both the standard deviation as a function of the number of measurements averaged to make up a frequency measurement and the relative precision that was attained for varying lengths of measurement times (assuming 10 seconds per measurement) are shown. Note that these figures were produced by summing the data for the reduced cyclotron frequency monitoring process in the LEBIT magnet shown in Fig. 4.10.

As can be seen from Fig. 4.11, averaging 60 individual measurements, which required

~ 10 minutes (about the same amount of time required to perform a reference measurement using the TOF-ICR method), resulted in a relative precision of almost 2×10^{-8} . Similarly, a relative precision using the FT-ICR method could reach nearly 1.5×10^{-8} by doubling the measurement time to 20 min. In addition, the measurement cycle could be optimized and, in principle, could be shorter than 2 seconds. The resolution could also be increased if a lighter ion was identified and monitored. Therefore, given these results, a precision of 1×10^{-8} should be attainable by the MiniTrap utilizing the FT-ICR technique within a reasonable measurement time.

4.4 MiniTrap Magnetometer Design and Fabrication

The design and fabrication process of the MiniTrap required a year to complete, and resulted in a novel design that would not only be able to fit inside an enclosure of the required dimensions, but would also be relatively easy to manufacture and assemble. Different concepts to produce the proper trapping potentials with electrodes of various materials and methods were studied. One example includes producing the trapping potential by applying voltages to electrodes that could be coated on the inside of machined ceramic blocks. Another was injecting electrodes into glass blocks that had been etched out by micromachining. Other concepts and variations of these were explored, however, the following presentation concentrates on the details of the final design.

4.4.1 Trap Geometry and Factors Affecting Trap Dimensions

A variety of trap geometries and electrode configurations have been researched for use in FT-ICR mass spectrometry (see [99] for a review of trap geometries and electrode configurations).

Of these geometries the two most commonly used in high-precision PTMS are the hyperbolic and cylindrical ring geometries. To maximize the ease of manufacturing, a Penning trap with a cylindrical geometry was chosen. The two cylindrical geometries considered were the mechanically compensated and the electrically compensated cylindrical traps in either the open-ended or closed-ended configurations that are described in detail in Refs. [100] and [101]. The electrically compensated cylindrical trap in the open-ended configuration was chosen for ease of tuning and to allow injection of the electron beam in addition to providing increased gas conductance to achieve a lower background pressure.

Many factors were taken into consideration when designing the overall size of the Penning trap. Due to the annular geometry of the space available to locate the magnetometer, the electrode structure assembly should ideally fit within a hollow cylinder with an outer diameter of 2.5 cm, leading to a trap size with a radius no larger than 1 cm. There are more important factors, however, that must be analyzed to determine the proper trap radius and include effects due to special relativity, magnetic field inhomogeneity, electrostatic field imperfections, trap voltage stability, and image charge shifts.

The first major constraint on the trap radius arose from effects due to special relativity and magnetic field inhomogeneity. As detailed in [102], the effects due to special relativity can be seen by substituting γm for m in Eqn. 2.2 and expanding γ to lowest order in v/c . In the regime of $|\omega_c| \approx |\omega_+| \gg |\omega_z| \gg |\omega_-|$, the relativistic shift to the reduced cyclotron motion becomes:

$$\frac{\Delta\omega_+}{\omega_+} \approx -\frac{1}{2} \left(\frac{qB}{mc} \right)^2 \rho_+^2, \quad (4.5)$$

and by propagation of errors:

$$\delta\left(\frac{\Delta\omega_+}{\omega_+}\right) \approx -\left(\frac{qB}{mc}\right)^2 \rho_+ \sigma_{\rho_+}, \quad (4.6)$$

where c is the speed of light and ρ_+ (σ_{ρ_+}) is the radius (and its standard deviation) to which the ion cloud is excited with respect to the center of the trap. As we can see from Eqn. 4.6, the shot-to-shot variation in ω_+ is proportional to both the extent and the reproducibility of the radii to which the ions are excited, however, the mass of the ion plays a bigger role. For example, ionized water molecules, with a mass of 18 u, can be excited to $\rho_+ > 3$ mm with σ_{ρ_+} of a few percent with negligible shifts due to special relativity. However, for ionized diatomic hydrogen, with a mass of 2 u, the effects of special relativity become non-negligible at $\rho_+ > 1.5$ mm for σ_{ρ_+} of a few percent. A shift in ω_+ can also be caused by inhomogeneities in the magnetic field and can become non-negligible when exciting the ions to larger z and ρ_+ . Fortunately, the frequency shift due to magnetic field inhomogeneities caused by axial amplitudes averages out, and the variation of the magnetic field over such a small region of space causes a frequency shift that is negligible in comparison to the frequency shift caused by special relativity. Nevertheless, to limit contributions to the inhomogeneity of the magnetic field, care was taken to build the MiniTrap using the proper materials with low magnetic susceptibilities.

Ideally, the trap radius should be only slightly larger than ρ_+ to maximize the image current induced on the detection electrodes, but the effects of electrostatic field imperfections, trap voltage stability, and image charge shifts increase for traps with small radii. The trap radius must, therefore, be made as small as possible to maximize the image current for ions excited to a smaller ρ_+ (as necessitated by the effects of special relativity), but kept

large enough such that the effects of electrostatic field imperfections, trap voltage stability, and image charge shifts remain negligible. A careful analysis of the trapping potential was performed to determine the minimum trap size for an allowable range of electric field imperfections.

In a cylindrical Penning trap, the electrostatic potential produced is only approximately quadratic near the center of the trap. To quantify the anharmonicities present near the center of the trap it is useful to expand the electrostatic potential, V , as a series of Legendre polynomials:

$$V = \frac{V_o}{2} \sum_{n=0}^{\infty} C_n \left(\frac{r}{d}\right)^n P_n(\cos\theta), \quad (4.7)$$

where V_o is the potential difference between the ring and endcap electrodes and d is the characteristic trap parameter described in Eqn. 2.1. In Eqn. 4.7, the dimensionless coefficients, C_n , for $n = \text{even}$ combine with even powers, and $n = \text{odd}$ combine with odd powers of the normal-mode amplitudes, but due to the axial and cylindrical symmetry of the trap the $n = \text{odd}$ coefficients are expected to be zero. For a perfect quadrupole potential, the $n = 0$ term is just an overall constant, the $n = 2$ term is equal to 1, and all other coefficients are zero. Thus, the even C_n coefficients greater than 2 in the actual potential indicate the degree of anharmonicities present in the trapping potential. It is important to calculate and minimize these anharmonic terms for a given trap geometry since they produce shifts in the normal-mode frequencies of the trapped ions. Note that the equation for the axial eigenfrequency given in Eqn. 2.4 is actually a first order approximation and is only valid when $C_2 = 1$, and due to the geometry of an open-ended cylindrical trap $C_2 \neq 1$ in the MiniTrap. To

first order, the axial frequency can be represented by the equation:

$$\omega_z = \sqrt{\frac{qV_o}{md^2}} C_2. \quad (4.8)$$

The higher order coefficients of Eqn. 4.7 become less significant when ρ_+ is small compared to d . In this case, the lowest order coefficients contribute most to shifts in the normal-mode frequencies, and have been derived in [103]. The leading order terms (assuming negligible magnetron and axial normal-mode oscillation amplitudes) are:

$$\frac{\Delta\omega_+}{\omega_+} \approx \frac{3\omega_-}{2\omega_+} C_4 \left(\frac{\rho_+}{d}\right)^2 \text{ for } n = 4 \quad (4.9)$$

and

$$\frac{\Delta\omega_+}{\omega_+} \approx -\frac{15\omega_-}{8\omega_+} C_6 \left(\frac{\rho_+}{d}\right)^4 \text{ for } n = 6, \quad (4.10)$$

where the approximations $\omega_c \approx \omega_+$ and $\rho_c \approx \rho_+$ have been made. First of all, notice that the absolute shift in ω_+ is proportional to the C_n terms. In addition, Eqn. 4.9 and Eqn. 4.10 indicate that the overall shift in ω_+ can be reduced by implementing a trap with a larger characteristic trap parameter. These absolute frequency shifts, however, are unimportant so long as they are reproducible from one measurement to the next. From Eqns. 4.9 and 4.10, it can be shown that the reproducibility of ρ_+ minimizes the shot-to-shot variation in ω_+ for smaller characteristic trap parameters. Particularly, as long as the reproducibility of ρ_+ is kept to within a few percent, the shot-to-shot variation in ω_+ becomes negligible (at a relative precision of 1 part in 10^{-8}) with values of C_4 and C_6 smaller than 0.02 for characteristic trap parameters as small as 2.1 mm.

Not only do larger traps benefit from a reduced shift to ω_+ caused by trapping potential

anharmonicities, but the effects of trap voltage stability and image charge shifts are also reduced for larger values of d (at the cost of a reduced image current signal). Using Eqns. 2.2, 2.5, 2.6, and 4.8 together with the approximation that $\omega_+ \approx \omega_c$, it can be shown that the shift in ω_+ due to trap voltage fluctuations can be described as:

$$\frac{\Delta\omega_+}{\omega_+} \approx -\frac{1}{2} \frac{(m/q)C_2}{B^2 d^2} \Delta V. \quad (4.11)$$

As long as voltage fluctuations are kept below $500 \mu\text{V}$, the shift due to voltage fluctuations (at the desired level of precision) is negligible for characteristic trap parameters greater than 2.1 mm. In addition, image charge shifts also become negligible for an ion bunch with fewer than a thousand ions in a cylindrical trap of $d > 2.1 \text{ mm}$ (for ions excited to half the trap radius) [89]. To further minimize shifts due to image charges, it is necessary not only to provide a stable electron current (within a few percent) to minimize the variation in the number of ions produced from one measurement to the next, but to also trap and detect as few ions as possible.

In the end, a trap with a characteristic trap parameter of $\sim 2.2 \text{ mm}$ was chosen. A trap of this size should be small enough to allow the detection of ion clouds with small ρ_+ to reduce the shift caused by special relativity for lighter masses, such as H_2^+ . A d of 2.2 mm should also be large enough to limit the effects due to electrostatic field imperfections, trap voltage stability, and image charge shifts that would result in non-negligible shifts to ω_+ (provided that a trapping potential could be produced with C_4 and C_6 smaller than 0.02, σ_{ρ_+} could be limited to a few percent, the trapping potential stabilized to within $500 \mu\text{V}$, and the electron beam current stabilized to within a few percent).

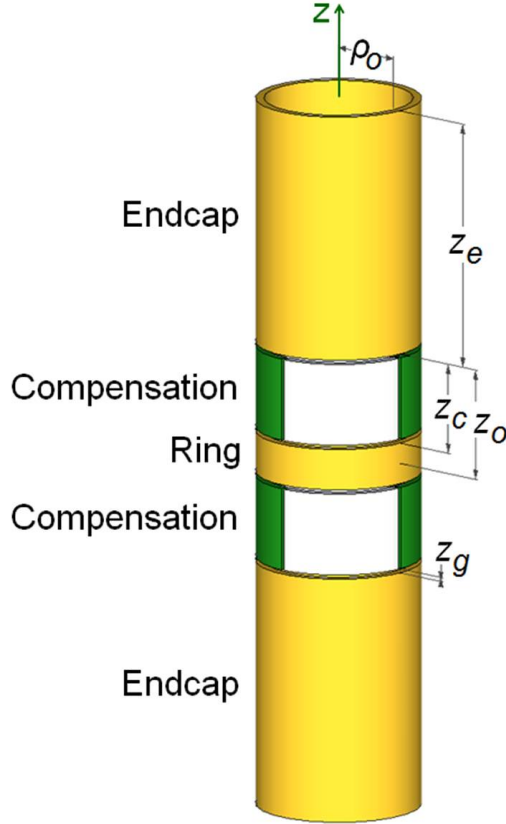


Figure 4.12: Cylindrical open-ended Penning trap electrode structure and dimensional nomenclature (see text). The compensation electrodes each have four-fold segmentation where the detection electrodes are shown in green and the excitation electrodes are shown in white.

4.4.2 Determination of Trap Dimensions

Analytical and numerical simulations were performed to determine the trap electrode dimensions and the allowable machining tolerances that would produce an electric quadrupole field with minimum contribution to higher order terms. In Fig. 4.12, the open-ended cylindrical trap dimensions are shown, where ρ_o and z_o are the characteristic trap radius and length, respectively, z_c and z_e are the lengths of the correction electrodes and the endcaps, respectively, and z_g is the gap size between the electrodes. (Using this nomenclature convention, z_c includes both gaps on either side of the correction electrodes.) The correction electrodes (instead of the ring) have a four-fold segmentation to maximize the surface area of the de-

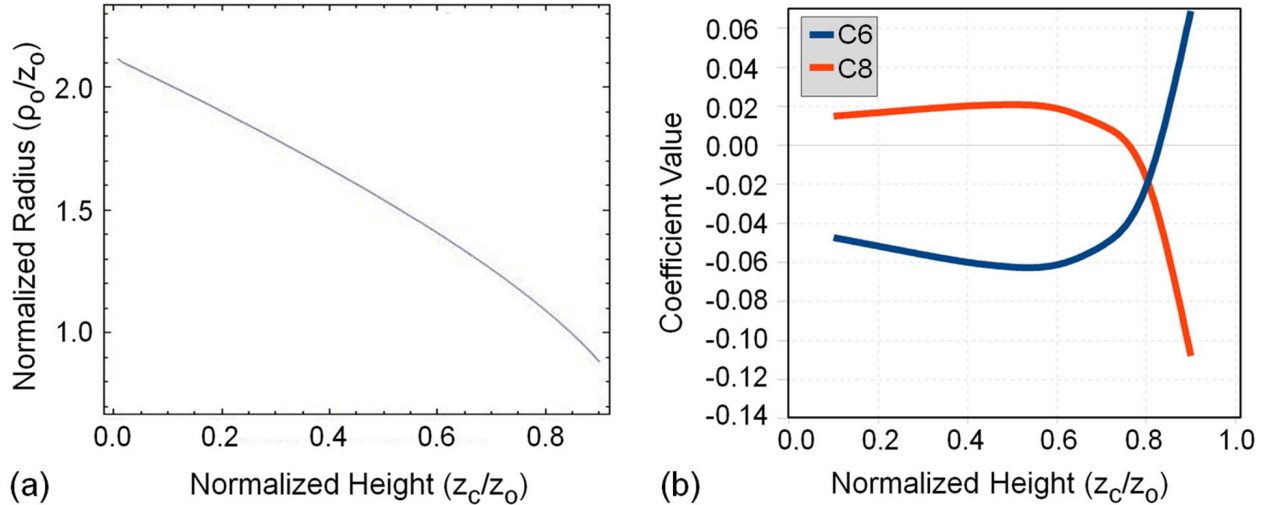


Figure 4.13: (a) The normalized radius vs normalized height necessary to orthogonalize a cylindrical trap with negligible gaps and infinite endcaps. (b) Variation of the coefficients, C_6 (in blue) and C_8 (in red), are shown with respect to normalized height for an orthogonalized trap tuned for $C_4 = 0$.

tection electrodes, resulting in an increased induced image current. The procedure utilized to optimize the trap dimensions closely followed that described in [101] and the reader is referred to that work for greater detail.

An orthogonalized trap geometry was implemented for the MiniTrap. This was accomplished by choosing the value of ρ_o/z_o that allows C_2 (and thus the axial frequency of the trapped ions) to become independent of the voltages applied to the correction electrodes [100]. This was not a requirement for the MiniTrap since the axial frequency would not be used to monitor or tune the trap, however, the radial eigenfrequencies also depend on C_2 . By using the orthogonalized geometry, shifts to the radial eigenfrequencies caused by tuning would thus be minimized. The normalized radii and compensation electrode heights to orthogonalize the open-ended trap of cylindrical geometry (without gaps) were found (using Mathematica) using the method of [101]. The results are shown in Fig. 4.13(a).

In an orthogonalized Penning trap, it is possible to tune the trapping potential such that the leading order anharmonic term of Eqn. 4.7, C_4 , can be set to zero for the proper relative

potential of the correction electrodes. However, C_6 and C_8 should also be minimized for high-precision measurements. Fig. 4.13(b) shows the values of C_6 and C_8 as a function of the normalized height for a trap geometry that has been both orthogonalized and tuned for $C_4 = 0$. As Gabrielse *et. al.* [101] pointed out, the normalized height of $z_c/z_o \approx 0.835$ is enticing, since here, both C_4 and C_6 are equal to zero. These results, however, are only valid for a trap with infinite endcap electrodes with negligible gap sizes. For a cylindrical trap with $z_e \geq 3\rho_o$, the coefficients, C_n , are within 1% of the infinite endcap electrode limit [101]. In larger traps, the effects due to the gaps are negligible, but for smaller trap sizes, they have to be taken into account. In addition, ground potential electrodes, located on either side of the trap (for electron beam extraction and electron beam measurements), needed to be taken into account. Therefore, many numerical simulations were carried out with SIMION to verify the analytical results and to determine the proper dimensions that would allow for realistic trapping potentials and achievable machining tolerances.

The simulations using the SIMION code provided trapping potentials created from electrode configurations that could realistically be manufactured. First, to extract the coefficients of the trapping potential, the electrostatic potential for a given electrode geometry was refined, as shown in Fig 4.14(a), and the value of the potential associated with each electrode along the z-axis of the trap in the trapping region the size of z_o was extracted. A Mathematica routine (based on the fit procedure described in [58]) was then used to adjust the ring and endcap electrode potentials as needed to provide an overall potential with $C_4 = 0$. The routine also performed a best fit to the overall potential created by SIMION, shown in Fig. 4.14(b), and calculated the relevant C_n terms. Following the procedure in [104], an F-test [105] on the fit of the overall on-axis potential indicated that including more than the first five even terms overconstrained the fit, therefore, only the first five even terms were

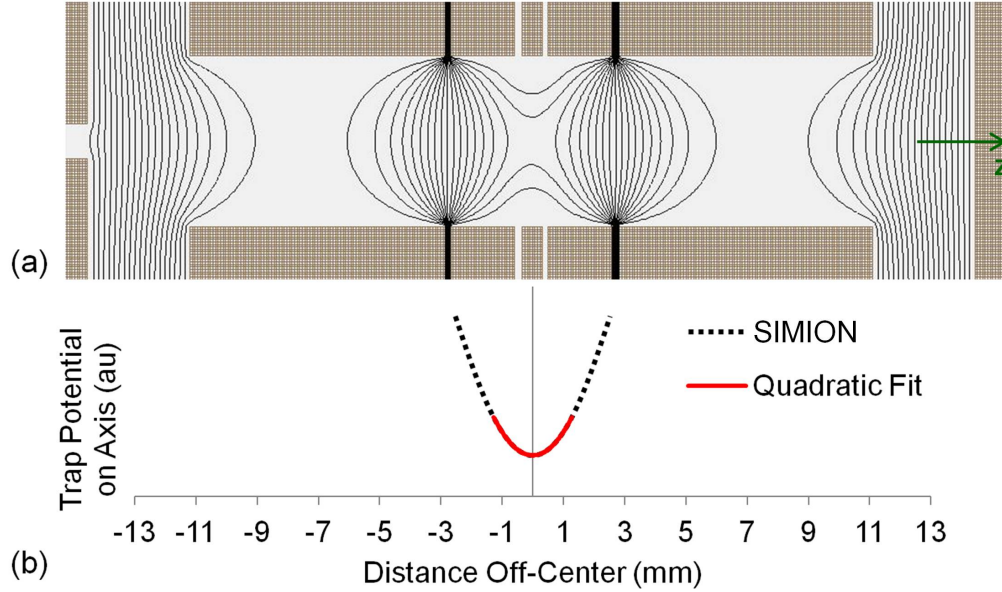


Figure 4.14: (a) A cross-sectional side view of the orthogonalized cylindrical, electrically compensated, open-ended configuration with grounding electrodes on either side created in SIMION, where the solid black lines represent equipotential lines. (b) A plot of the trapping potential along the z -axis in the trapping region where the dotted line is the on-axis potential extracted from SIMION when the electrode voltages are set to make $C_4 = 0$. The solid line (red) is the best quadratic fit to that potential in a trapping region of length z_0 .

used to describe the on-axis potential.

Many geometries were investigated to first orthogonalize the trap, tune for $C_4 = 0$, and minimize C_6 for different gap sizes, endcap electrode lengths, and distances between the grounded electrodes and the endcaps. The results of the optimal trap parameters from the analysis are given in Table 4.1, where the tolerances were determined by constraining C_6 to be no greater than ± 0.01 . The corresponding electrode voltages and the five resulting even C_n coefficients are given in Table 4.2. To achieve a C_6 within ± 0.01 , the electrodes needed to be machined with tolerances as low as 0.5 mil, or 0.0127 mm, which was achievable at the NSCL's machine shop.

Table 4.1: Dimensionless trap parameter ratios and the corresponding physical trap parameters (with $\rho_o = 2.5$ mm) for the optimized (minimized C_4 and C_6) open-ended, electrically compensated, cylindrical trap as determined through Mathematica analysis of SIMION potentials.

Parameter	Value
ρ_o/z_o	0.990(13)
z_c/z_o	0.867(13)
z_e/z_o	2.970(14)
z_g/z_o	0.0495(40)
ρ_o	2.500(29) mm
z_o	2.525(29) mm
z_c	2.190(29) mm
z_e	7.500(26) mm
z_g	0.125(10) mm

Table 4.2: Electrode voltages and the resulting C_n coefficients for the optimized trap using the dimensions given in Table 4.1. Note that the endcap and ring voltages are scalable (see text).

Parameter	Value
Endcaps	1.0 V
Correction Rings	0 V
Ring	(-) 0.14391 V
C_0	0.203750
C_2	0.559036
C_4	0.000005
C_6	-0.000046
C_8	-0.027249

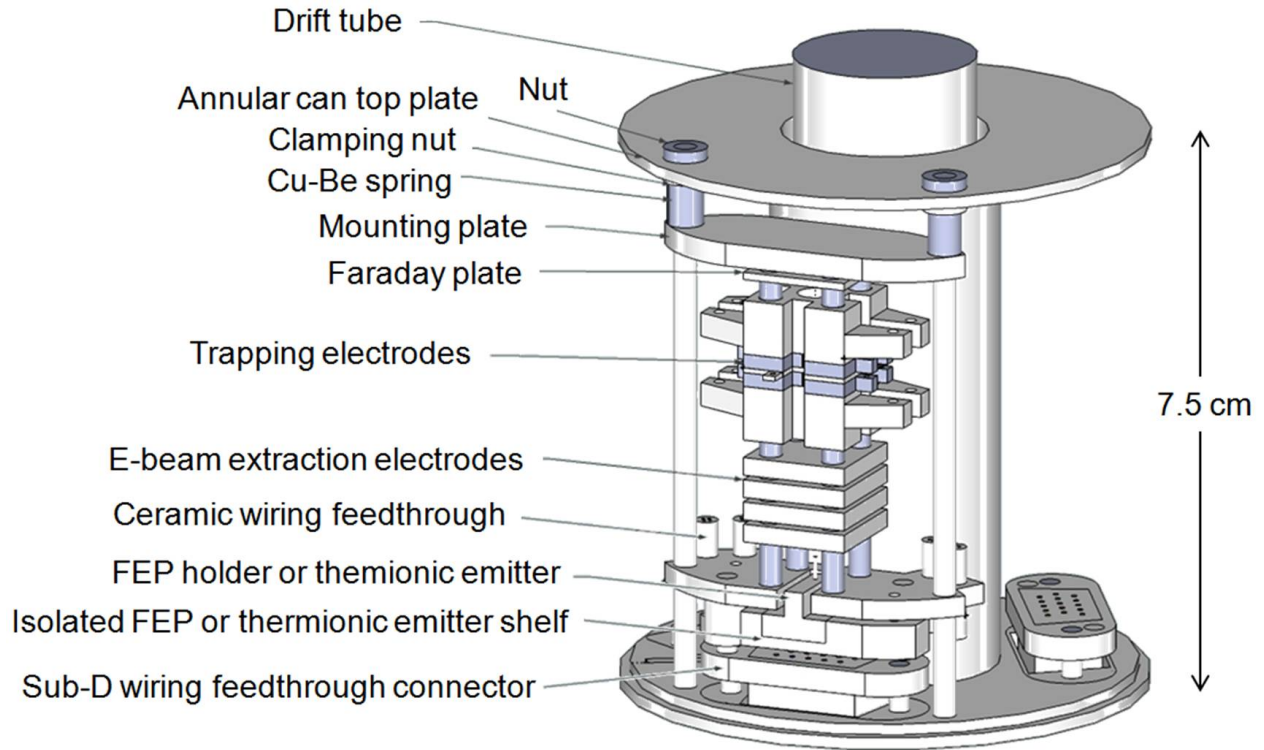


Figure 4.15: Screenshot of the Google SketchUp rendering of the MiniTrap assembly concept pointing out the various components. (Note that the outside of the enclosure is not shown.)

4.4.3 Design and Fabrication of the MiniTrap

The initial design of the MiniTrap was performed using Google SketchUp. For ease of assembly, maintenance, and mounting in the LEBIT magnet, one annular enclosure was utilized that could be mounted onto the ejection drift tube located just downstream of the hyperbolic trap. The Google SketchUp model shown in Fig. 4.15 shows the final design concept that was later detailed by the NSCL's Mechanical Engineering department in SolidWorks before being sent to the NSCL's machine shop for fabrication.

The MiniTrap assembly concept had an annular enclosure with an inner diameter of ~ 2.86 cm (only a couple millimeters greater than the diameter of the drift tube), an outer diameter of ~ 7.3 cm, and a length of ~ 7.5 cm. The assembly was designed such that all of the components could easily fit inside the enclosure and could be assembled without difficulty.

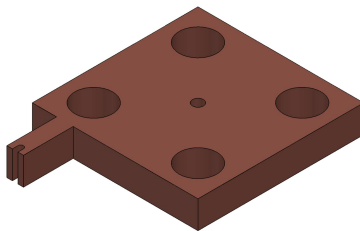


Figure 4.16: Isometric view of the copper electrodes utilized to extract the electron beam.

The design of the MiniTrap assembly was broken up into seven different components: 1. the electron beam emitter shelf, 2. the electron beam extraction electrodes, 3. the trap electrodes, 4. the Faraday plate, 5. the alignment and mounting for those four components, 6. the alignment and mounting for the entire structure, and 7. the wiring feedthroughs.

The MiniTrap required the mounting of an FEP or a thermionic emitter to provide a beam of electrons to ionize the background gas. For flexibility, an electron beam emitter shelf was designed to allow easy replacement of FEPs and thermionic emitters. The shelf was slotted to allow for installation of a thermionic emitter or an FEP (secured in an FEP holder) of the same dimensions as the thermionic emitter. During operation of an FEP, the entire shelf was negatively biased to provide the initial energy for the electron beam while the extraction electrode was positively biased to create the field necessary for field emission. On the other hand, only the filament of the thermionic emitter needed to be biased to give the electron beam an initial energy and was accomplished by biasing the power supply used to heat the filament.

The extraction electrodes shown in Fig. 4.16 were implemented to provide potentials that not only extract the beam from the FEP, but also to block or to pass the electron beam through to ionize the background gas without changing the beam's energy. This was accomplished with four Oxygen-Free Electronic (OFE) copper electrodes 3 mm in thickness with 1 mm diameter holes machined through center. (The ratio of thickness to diameter

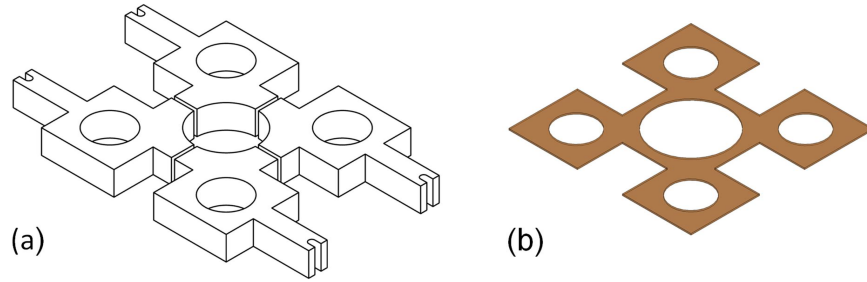


Figure 4.17: Isometric view of one (a) four-fold segmented correction electrode and (b) a kapton spacer.

was strategically chosen to prevent stray electric fields from passing through the electrodes.) The first electrode, the extraction electrode, had to be positively biased to a potential large enough to induce field emission from an FEP and produce a stable current (in the case of the thermionic emitter, this electrode would be grounded). The second electrode, permanently at ground potential, was necessary to bring the beam created by the FEP back to its initial energy. The third electrode could be set higher than the beam's initial energy to block the electron beam or could be lowered to allow the beam, or a portion of the beam, to pass. The fourth electrode was also permanently held at ground potential to bring the beam back to its initial energy after passing through the blocking electrode. This electrode also provided a ground reference for the trap. In the corner of each electrode, four holes were located to allow ceramic mounting rods to be inserted. For insulation, four #2 ceramic washers were placed between each electrode and aligned by the mounting rods.

The trap electrode structure was designed to provide proper electrode spacing and electrical isolation, while maintaining the alignment necessary to keep within the tolerance limits given in Table 4.1. To obtain the proper axial spacing and isolation, 125 μm thick kapton sheets, shown in Fig. 4.17(b)), were located between each electrode, perpendicular to the trap axis. To properly align each electrode (including the four-fold segmented correction ring

electrodes shown in Fig. 4.17(a)), a lengthwise groove along the outside of each of the trap electrodes was added for which a ceramic square rod with a small tolerance could be inserted during assembly. The groove was also beneficial for lowering the capacitance between the electrodes to promote a higher Q factor of the resonant circuit. The trap electrode structure was designed to be compressed into a single unit for ease of assembly and to fix the position of the trap electrodes. To mount the trap assembly, a hole was located in each corner of each electrode for the ceramic mounting rods to be inserted.

A Faraday plate, located just downstream of the trap electrodes, was used to measure the electron beam current that passed through the trap. Like the other electrodes it was composed of OFE copper and had holes in the corners to allow the ceramic mounting rods to be inserted through the otherwise solid Faraday plate. The Faraday plate was 1 mm thick and thinner than the extraction electrodes to conserve space.

The method by which wires could be attached to the extraction, trapping, and Faraday plate electrodes was also carefully considered. A crimping method was chosen in which 26 gauge wire was inserted into a groove in a tab projecting from each electrode and the tab crimped to secure the wire. The benefit of this technique was that the connection would be permanent and individual components would not come free due to vibration or expansion and contraction of the materials. The only electrodes not equipped with the crimping tabs were the endcaps for which wire could be secured by the clamping screws.

The electron beam emitter shelf, the extraction electrodes, the assembled trapping electrodes, and the Faraday plate were located with respect to one another with ceramic tubes placed on the four ceramic mounting rods that passed through each of the electrodes and terminated inside recessed holes in the lower and upper mounting plates. Axial alignment of the trap with respect to the whole enclosure was accomplished by mounting the structure

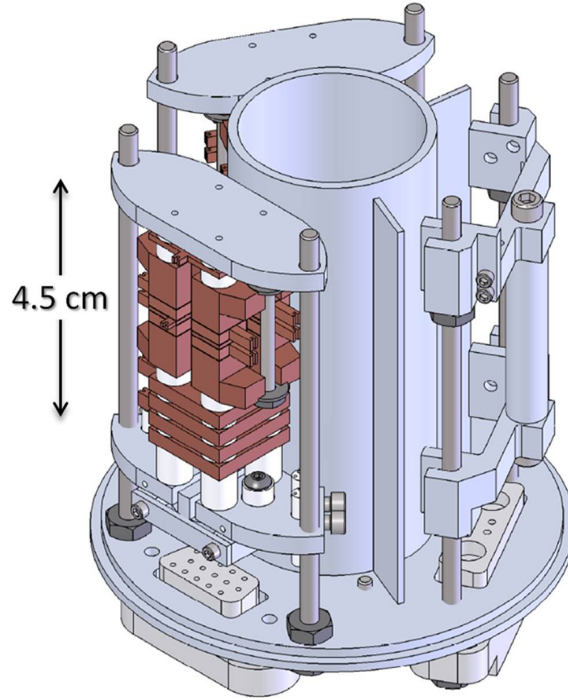


Figure 4.18: Isometric view of the MiniTrap assembly designed in SolidWorks. (Note that the top of the enclosure has been removed.)

onto two titanium 4-40 threaded rods that extended through the mounting plates and the annular enclosure which also provided the compression necessary, through the use of nuts and copper-beryllium springs, to hold the MiniTrap assembly together. A photograph of two completed trap assemblies is shown in Fig. 4.19(b).

Routing the wires through the enclosure for the detection signals and the application of voltages to the electrodes relied on UHV sub-D connectors by Accuglass. The wires crimped to the electrodes were fitted with pins and inserted into a 15-pin female connector inside the enclosure. Wire harnesses (secured to the 15-pin sub-D female connector) on the outside of the enclosure could be attached to two hermetic 9-pin sub-D connector conflat assemblies to route the wires out of the beam line.

Once the requirements of the MiniTrap had been worked out, the detailed design was taken to the Mechanical Engineering department at the NSCL. The final assembly drawing is

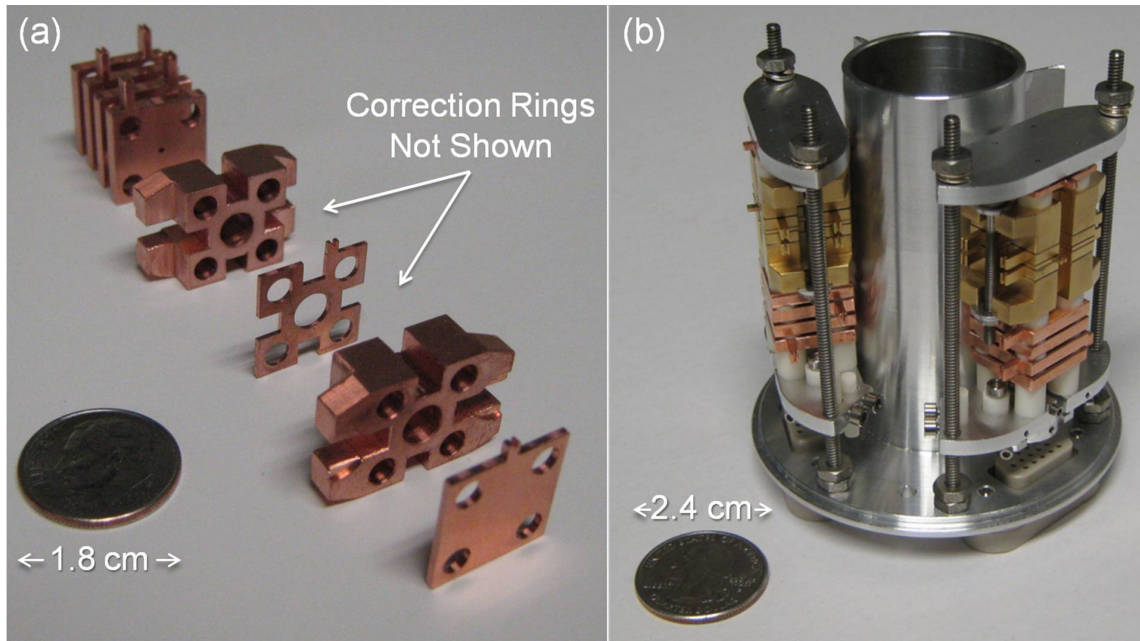


Figure 4.19: (a) Image of the extraction and trapping electrodes (before gold plating and without the correction rings) before assembly. (b) Image of the fully assembled MiniTrap with the top half of the annular enclosure removed before wiring the electrodes. (Note the difference in scale between the two images.)

shown in Fig. 4.18, with the top of the enclosure removed. Note that there are only two traps shown in the enclosure. A mounting structure and feedthrough for installing a getter pump using Non-Evaporable Getter (NEG) strips is shown in the space that would be taken by a third trap. Initially, it was thought that the getter could produce a background of hydrogen gas (hydrogen is released from NEG strips upon heating), in addition to being used to achieve a lower background pressure. However, activated NEG strips pump hydrogen better than any other molecule. After experimenting with the getter pump, it was determined that the constant background of hydrogen required by the MiniTrap could not be sustained. It was, therefore, decided that the MiniTrap would rely on the residual background gas in the enclosure. For implementation of the MiniTrap in the LEBIT magnet, a small hole was drilled in the bottom of the enclosure allowing the MiniTrap to share the UHV of the bore of the LEBIT facility's superconducting magnet.

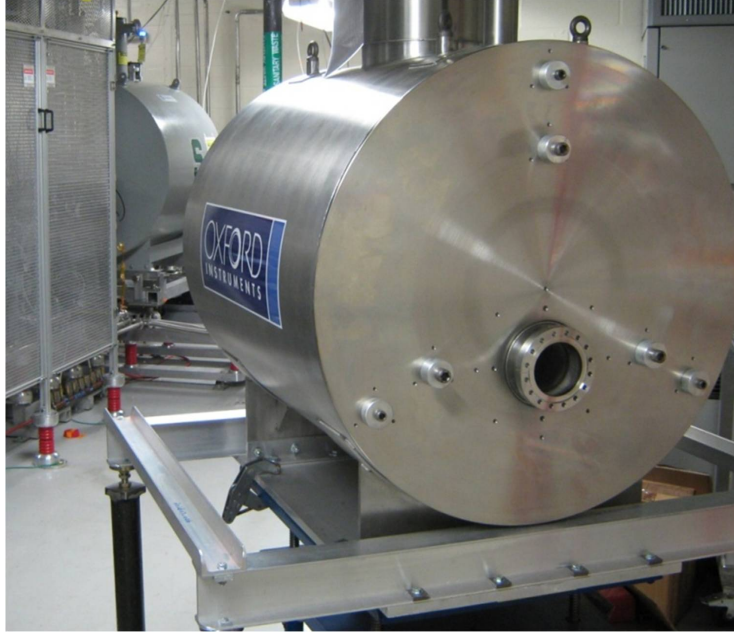


Figure 4.20: Image of the SIPT magnet before the beam line components for testing the MiniTrap had been installed.

After the extraction and trapping electrodes had been fabricated from OFE copper, as shown in Fig. 4.19(a), the trapping electrodes were gold plated to reduce possible patch effects that could produce an inhomogeneous surface charge distribution. The completely assembled MiniTrap is shown in Fig. 4.19(b) before installing the electrode wiring to connect the electrodes to the 15-pin sub-D female connector. All of the metallic components used in the assembly were either copper, aluminum, brass, or titanium with low magnetic susceptibilities to limit the production of magnetic field inhomogeneities.

4.5 Testing the MiniTrap Magnetometer

The test of the MiniTrap was performed in the 7 T superconducting magnet obtained for the SIPT facility [97] (shown in Fig. 4.20). On one end of the magnet a Leybold turbo pump capable of pumping 200 L/s, backed by a Varian TriScroll roughing pump, was connected

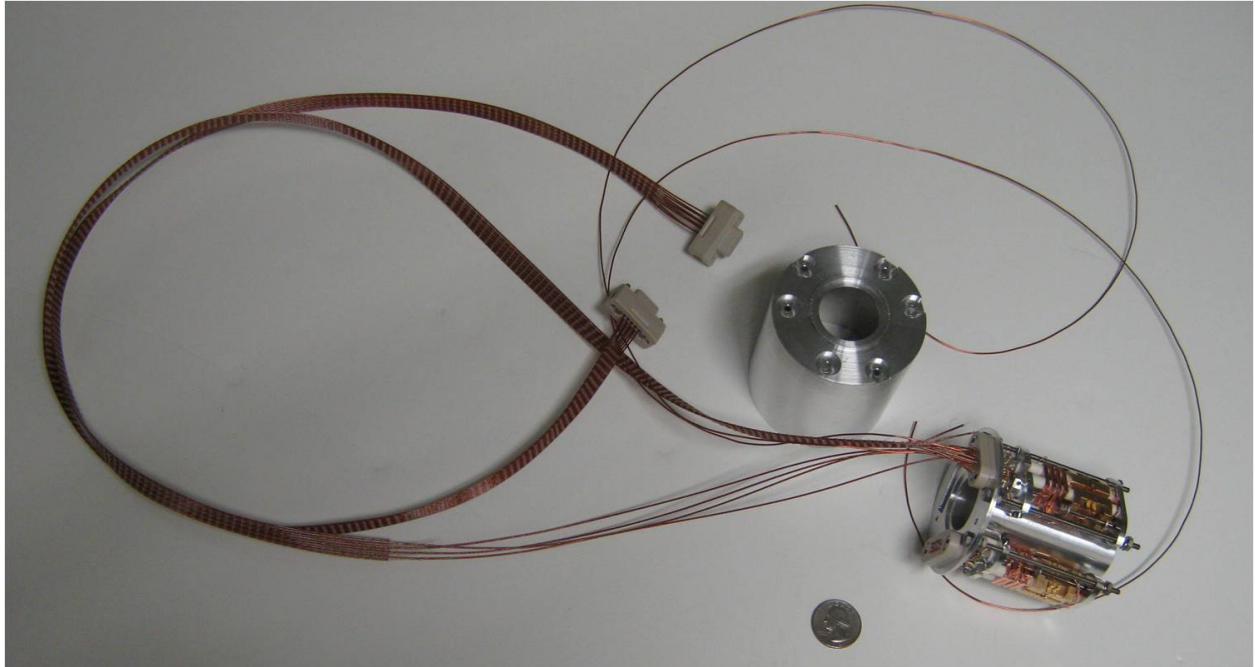


Figure 4.21: Image of the MiniTrap assembly fully wired (with the top of the enclosure removed and shown near the traps), ready to be mounted and inserted into the SIPT magnet. The two separate wires are of a larger gauge for supplying current to the thermionic emitter.

to the bore tube, in addition to an MKS Pirani gauge and a cold cathode Penning gauge capable of measuring pressures as low as 10^{-10} mbar. On the opposite side of the magnet a 6 inch conflat 6-way cross was attached. The MiniTrap assembly was supported by a 24 mm diameter aluminum rod attached to the center of a 6 inch conflat flange (secured to the 6-way cross) that held the MiniTrap assembly axis along the central axis of the magnet's bore.

A thermionic emitter was installed due to its proven reliability and stability. In addition, tests indicated that for electron beam currents of ~ 1 nA, the trap temperature was expected to only increase by a few degrees Celsius. The final MiniTrap assembly, shown in Fig. 4.21, was secured to the mounting rod which located the MiniTrap in the center of the magnet. Before being inserted into the magnet, the MiniTrap enclosure was wrapped with a solenoid by winding of 28 coils of 16 gauge wire around the MiniTrap enclosure. A direct current could be sent through the coil and thus change the magnetic field by a known amount.

(Using the infinite solenoid approximation, a current of 1 mA should change the magnetic field by $\sim 10^{-6}$ T, corresponding to a shift in the cyclotron frequency of ~ 0.6 Hz.) The two sub-d connectors (shown in Fig. 4.21), were connected to two sub-d conflat connector flanges attached to the 6-way cross. The two thermionic emitter wires and the two solenoid wires were attached to a four-connector current feedthrough that was also attached to the 6-way cross. (The reader is referred to Appendix A for a discussion of the setup and operation of the electronics.)

4.5.1 Detection of Ion Motion via FT-ICR

The first test was to detect the self-excited magnetron motion that was observed during the tests using the LEBIT magnet. Then, the excitation and detection parameters were determined for automated measurements of ω_- with the MTCS. The trap was first tuned by measuring ω_- as part of the process to determine the optimal trapping potential which minimized the shift to ω_- as a function of excitation radius, ρ_- . With the proper excitation parameters and tuned trapping potential, it was then possible to search for reduced cyclotron motion by utilizing the detection of the magnetron motion as a probe. After cyclotron motion was detected, the trapping potential was tuned to minimize shifts to ω_+ by measuring ω_+ as a function of ρ_+ . Finally, repeating excitation and detection of the reduced cyclotron motion was used to monitor relative changes in the magnetic field.

4.5.1.1 Magnetron Motion

In a background pressure of $\sim 10^{-7}$ mbar (as recorded by the Penning gauge attached to the beam line outside of the magnet), the thermionic emitter was biased to ~ -90 V and heated by supplying a current of ~ 2 A. With all of the extraction electrodes and trapping

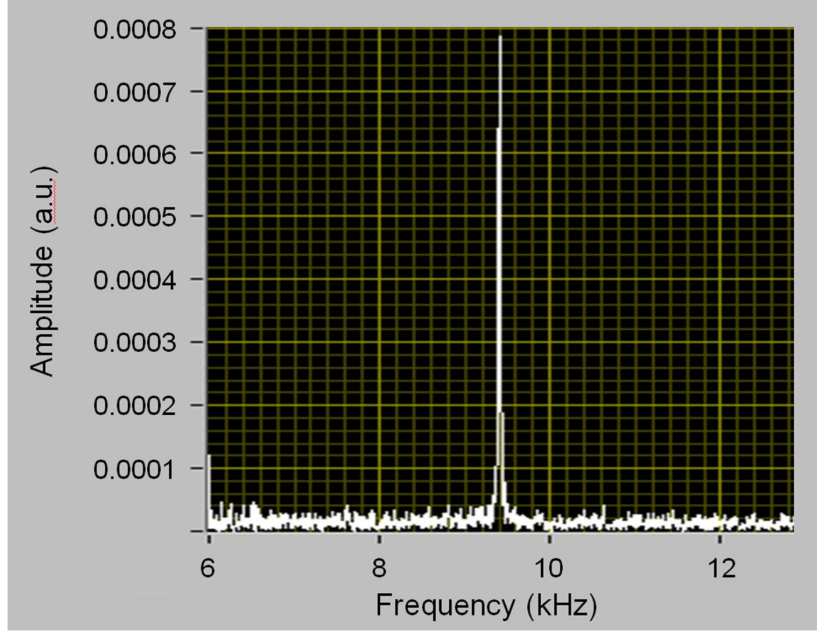


Figure 4.22: A LabVIEW screenshot of an FFT resonance of self-excited magnetron motion of trapped ions of unknown species in a 6.8 V potential well in the MiniTrap.

electrodes grounded, an electron beam current of several nA's was measured by a Keithley picoammeter attached to the Faraday plate. The trapping potential was then raised by setting the endcaps to 6 V and the ring electrode to -0.8 V to give an endcap-to-ring voltage ratio of 1 to 0.13 (approximately the same as that calculated in simulations using the values in Table 4.2). After ionizing the residual background gas for several seconds, the scope-card was triggered using the MTCS to acquire a signal for 80 ms at 25 megasamples per second (MS/s) from the differential pre-amplifier directly connected to two azimuthally opposing sets of correction electrodes (broadband dipole detection). The signal was analyzed using LabVIEW FFT analysis software, and resulted in the FFT resonance shown in Fig. 4.22. For the MiniTrap geometry and applied voltages a magnetron frequency, f_- , of ~ 9110 Hz would be expected, whereas in Fig. 4.22 $f_- \approx 9400$ Hz. The several hundred Hz shift was most likely due to image-charge shifts from the large number of ions being confined and self-excited in the trap.

Trap tuning scans of ω_- were performed with a fewer number of ions (at a lower electron beam current). A script was implemented in the MTCS that would first dump the trap for one second (then raise the trap), ionize the residual gas for 1 second with an electron beam current of 1 nA, then apply a sweep signal from 6 to 11 kHz on two sets of azimuthally opposing correction electrodes, 180 degrees out of phase, with a sweep cycle time of 5 ms. The MTCS would subsequently record the signal from the pre-amplifier (using broadband dipole detection) for 80 ms at 25 MS/s and analyze the resulting FFT resonance, and thus perform one magnetron frequency measurement. For trap tuning, 5 magnetron frequency measurements were performed each at a given sweep excitation amplitude beginning at 0.07 volts peak-to-peak (Vpp) and incrementing up to 0.28 Vpp in 0.015 Vpp steps. One of these more involved scans shows the shift in f_- as a function of ρ_- at a given endcap-to-ring voltage ratio.; for a perfectly tuned trap, the frequency would remain constant.

The f_- versus ρ_- scan was performed at various endcap-to-ring voltage ratios (while keeping the total trapping potential at 6 V) to determine the optimum trapping potential. The results of one of these f_- trap tuning scans is shown in Fig. 4.23 where the optimal endcap and ring voltages were 5.4 V and 0.6 V, respectively. Note that this ratio of endcap-to-ring voltage of 1 to 0.11 is only slightly larger than that determined from values obtained from the simulations given in Table 4.2, and is possibly due to imperfections in the trap geometry or alignment. Of greater importance is the ability to minimize shifts to f_- , indicating that anharmonicities in the trapping potential can indeed be tuned out as required for optimal performance of the MiniTrap. The tuning of the MiniTrap's trapping electrodes to minimize shifts in f_- thus provided optimal parameters for the detection of reduced cyclotron motion.

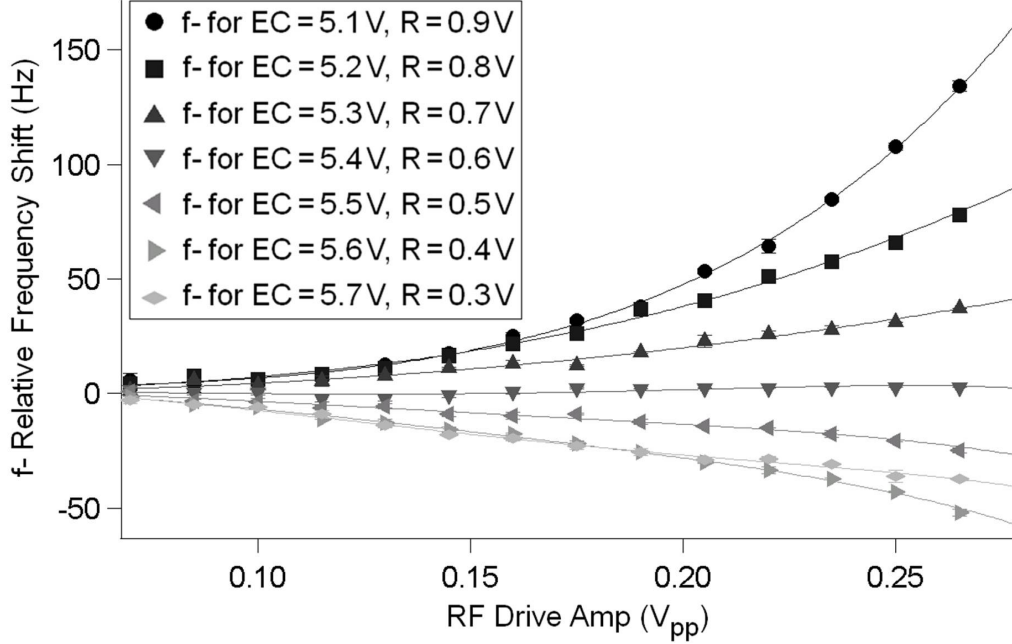


Figure 4.23: Results of trap tuning scans with the MiniTrap showing f_- versus the drive amplitude (proportional to ρ_-) for seven different endcap-to-ring voltage ratios for a 6 V potential well depth (the ring, by convention, is always negative). Note that the solid lines show polynomial fits (using only the first five even terms) to the data, where the error bars are shown, but are too small to be resolved in this image.

4.5.1.2 Reduced Cyclotron Motion

To identify the ion species in the trap, a magnetron frequency measurement was performed, however, prior to exciting the magnetron motion, the reduced cyclotron motion of the ions was excited (using dipole excitation) with a burst at a given frequency, f_{RF} , for $\sim 100 \mu\text{s}$ at 5 Vpp. Application of this signal was more than enough to drive any ions, whose reduced cyclotron frequency $\approx f_{RF}$, out of the trap. Subsequently, f_{RF} was scanned over a broad range, and when $f_{RF} \approx f_+$ (of an abundant ion species in the trap) the excited ions would no longer be in the trap resulting in a decreased magnetron FFT resonance amplitude.

A frequency range of 1 MHz was scanned, where 25 data points were obtained for each f_{RF} , in steps of 5 kHz, and required ~ 14 hours to complete. A portion of the results from a 5 MHz to 6 MHz scan using these parameters is shown in Fig. 4.24, where a minimum in the

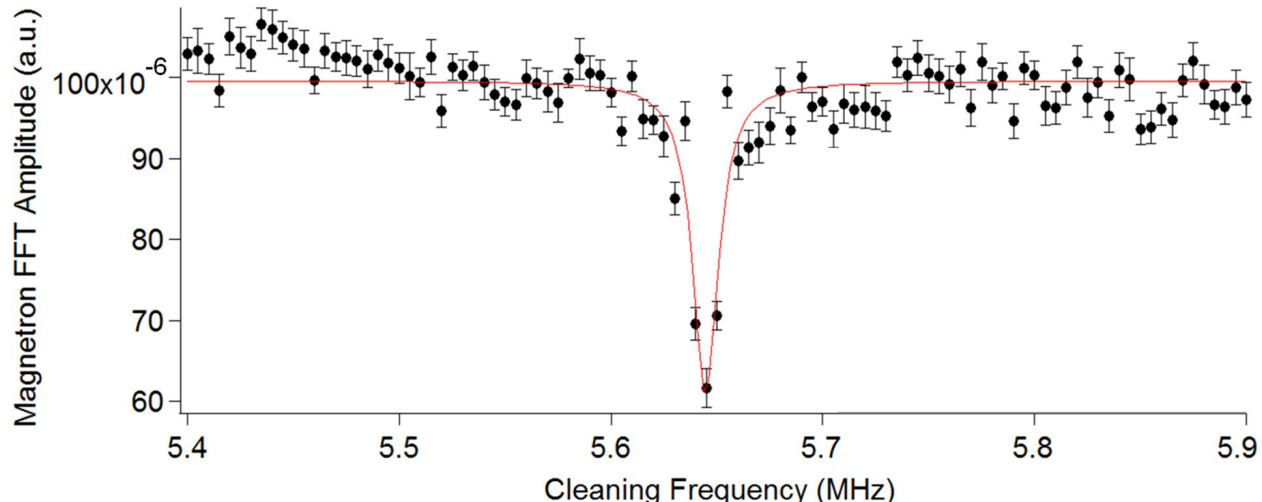


Figure 4.24: Example from the dipole cleaning technique utilized to determine the ion species in the MiniTrap. Each data point is the average of 25 magnetron excitation and detection measurements when the trap was first cleaned by applying a RF dipole electric field at 5 Vpp for $100\ \mu\text{s}$ at the cleaning frequency, f_{RF} . The Lorentzian fit to the data is represented by the solid line (red) where the fit results indicate $f_+ = 5.645(1)$ MHz.

magnetron FFT amplitude at ~ 5.645 MHz is clearly evident (corresponding to the reduced cyclotron frequency of the ions driven out of the trap). Using Eqns. 2.3 and 4.8 with the C_2 value listed in Table 4.2 and a magnetic field of 7 T, this frequency corresponds to a mass of ~ 19 u, the mass of H_3O^+ . It is also worth mentioning that the resonance did not completely disappear and that an additional magnetron “dipole” resonance was also seen at ~ 3.246 MHz, corresponding to a mass of 33 u, or HO_2^+ , the same ion species identified in the background gas during the tests in the LEBIT magnet using broadband axial detection. The HO_2^+ “dipole” resonance, however, was not nearly as pronounced, indicating that H_3O^+ was the most abundant ion species in the trap.

With H_3O^+ verified as the most abundant ion species in the trap, and the reduced cyclotron frequency determined for the operating parameters, reduced cyclotron motion was excited and detected. Excitation times of $T_{RF} \approx 100\ \mu\text{s}$ were used to excite reduced cyclotron motion. The excitation amplitude was varied until a resonance appeared; an example is

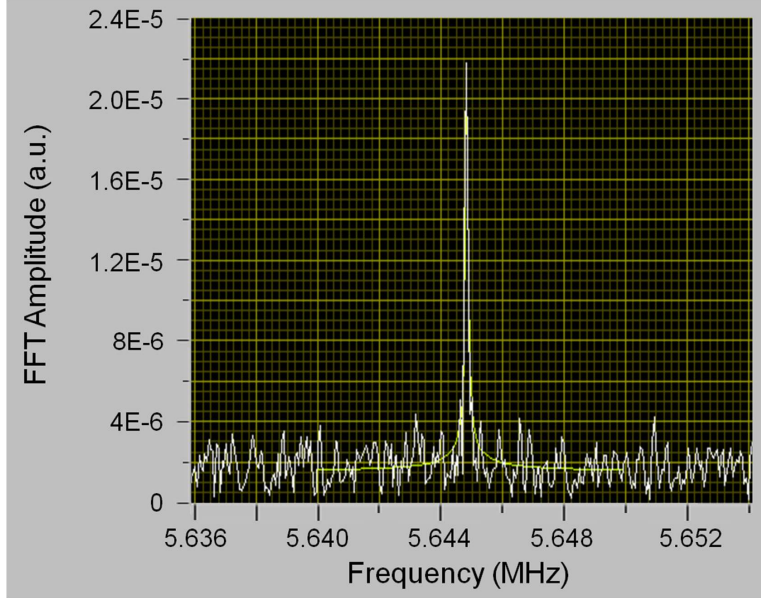


Figure 4.25: A LabVIEW screenshot of an FFT resonance of reduced cyclotron motion of H_3O^+ ions in a 6 V potential well in the MiniTrap using broadband FT-ICR detection. The faint solid yellow line represents the best Lorentzian fit produced by the LabVIEW program.

shown in Fig 4.25. Narrow-band FT-ICR detection was then implemented by installing an inductor with a Q value of ~ 280 in parallel to the detection electrodes in addition to a 5-25 pF air-core variable capacitor, from which the signal was transferred to the pre-amplifier via a secondary pickup coil as shown in Fig. 4.4. The detection circuit was carefully tuned to have a resonant frequency of 5.645 MHz and resulted in a Q -factor of ~ 250 .

To verify the parameters obtained from the trap tuning performed with magnetron motion, a trap tuning scan was performed by determining the shifts in the reduced cyclotron frequency utilizing the same procedure used to generate the graph shown in Fig. 4.23, exciting the ions at f_+ instead of f_- . The results of this second trap tuning procedure are shown in Fig. 4.26. An analysis of the even C_n coefficients indicates that the optimal endcap and ring voltages are 7.1 V and -0.9 V, respectively, resulting in an endcap-to-ring voltage ratio of 1 to 0.13. This value for the endcap-to-ring voltage ratio is in better agreement with the calculated endcap-to-ring voltage ratio found with simulations of 1 to 0.14, as compared to

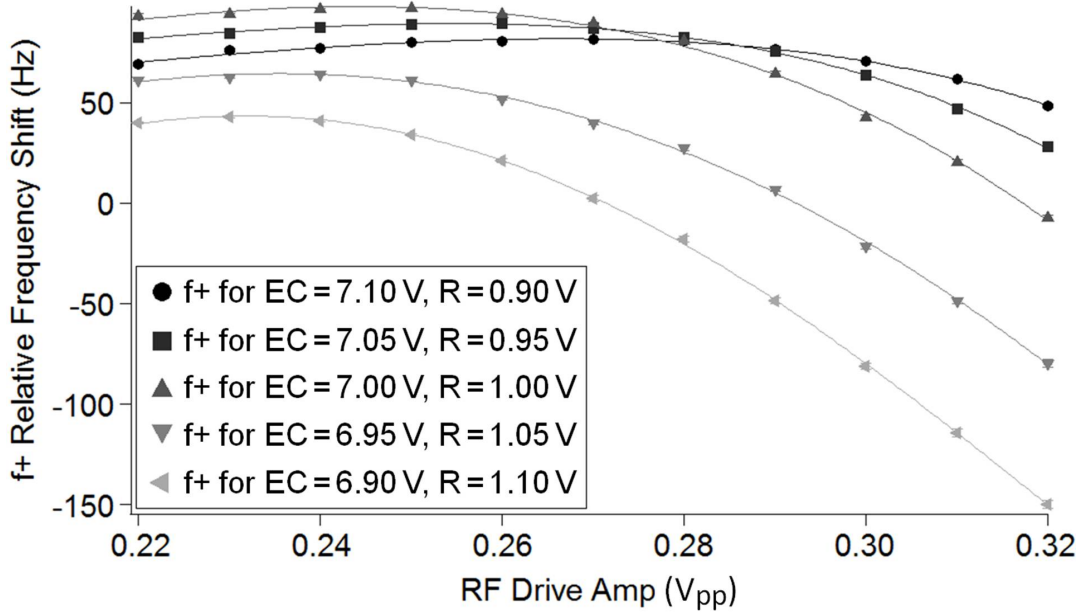


Figure 4.26: Results of trap tuning scans with the MiniTrap showing f_+ as a function of the drive amplitude (proportional to ρ_+) for five different endcap-to-ring voltage ratios for an 8 V potential well depth (the ring, by convention, is always negative). Note that the solid lines show the results of polynomial fits (using only the first five even terms) to the data, where the error bars are shown, but are too small to be resolved in this image.

that found with f_- versus ρ_- . Once the proper trap potential was found, an f_+ monitoring process was used to continuously cycle through measurements of f_+ to track changes in the magnetic field.

Before testing the f_+ monitoring process, an appropriate sample time to acquire the f_+ signal was determined. Longer sample times improved the resolution of the FFT, however, longer sample times resulted in the broadening of the FFT resonance linewidth together with a decrease in the FFT resonance amplitude, possibly due to loss of coherence of the ion cloud. At a pressure of $\sim 10^{-7}$ mbar (as measured near the turbo pump), linewidth broadening was noticeable with 50 ms long sample times. At a background pressure of $\sim 3 \times 10^{-8}$ mbar, a sample time of 100 ms resulted in reduced cyclotron FFT resonances with no indication of linewidth broadening. Therefore, to probe for longer periods of time, and thus increase the FFT frequency resolution, a lower background pressure would be necessary.

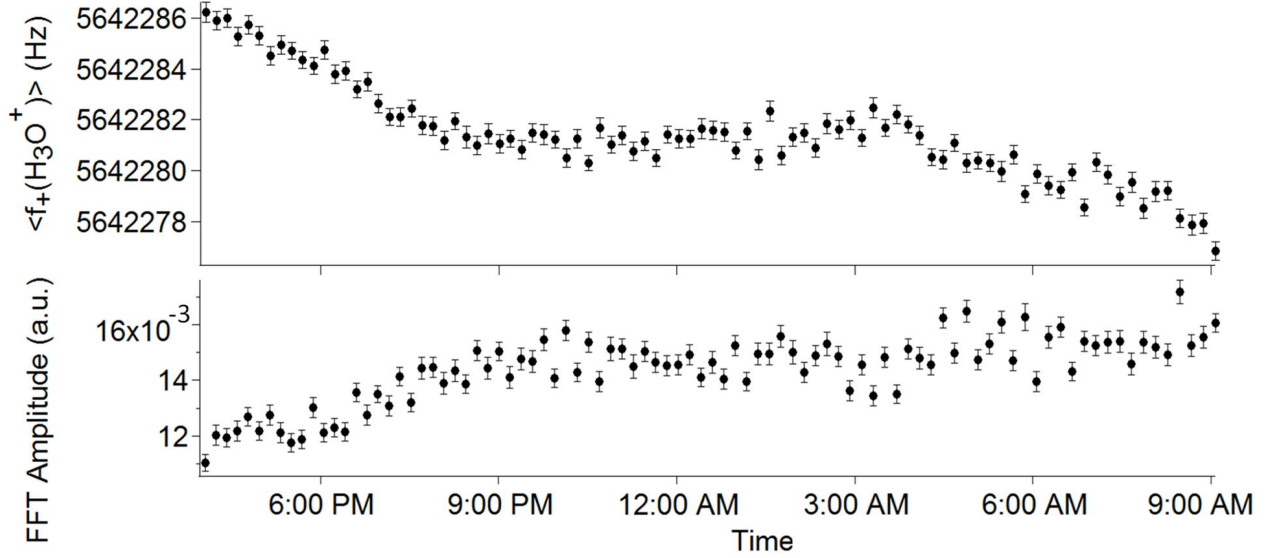


Figure 4.27: Results of the MiniTrap reduced cyclotron frequency monitoring process showing the average $f_+(H_3O^+)$ measurements and the average FFT amplitudes as a function of time recorded over a period of ~ 17 hours. Each data point is the average of 120 frequency measurements (requiring 10 minutes) where the error bars correspond to the 1σ uncertainty associated with the distribution of those 120 measurements. The average slope of the entire data set corresponds to a magnetic field decay rate of $-5.82(4) \times 10^{-8} \text{ hr}^{-1}$.

To monitor the drift in the magnetic field and to determine the precision of the magnetometer, an f_+ monitoring process recorded the reduced cyclotron frequency of H_3O^+ over the course of ~ 17 hours in the SIPT magnet. Each measurement consisted of ionizing the background gas with a steady (within a few percent) electron beam current of 0.2 nA for 1 second. The trapped ions were excited with a burst excitation at 5.642 MHz for $100 \mu\text{s}$ at 0.28 Vpp using dipole excitation. The signal was picked up using the narrow-band technique similar to that in the f_+ trap tuning. A 10 MHz custom bandpass filter, installed between the pre-amplifier and the scope-card used to record the signal, reduced the high-frequency background noise that was mixed down to lower frequencies. A small leak valve, mounted to the magnet bore, allowed a steady stream of air to be injected into the magnet bore to maintain a background pressure of $\sim 3.5 \times 10^{-8}$ mbar as measured by the Penning gauge near the turbo pump. Some of the results of the f_+ monitoring process are shown in Fig. 4.27.

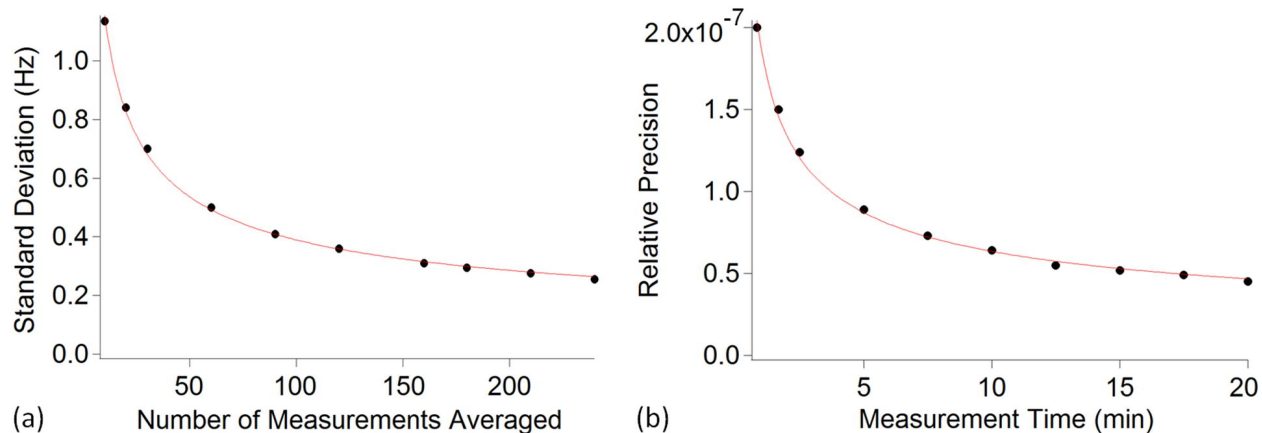


Figure 4.28: Results of the precision obtainable from the $f_+(\text{H}_3\text{O}^+)$ monitoring process with 10780 measurements. (a) The standard deviation of the data set is given when each frequency measurement is an average of a given number of measurements and (b) the measurement time necessary to achieve a given relative precision from the same data. The solid line (red) in each graph is the best fit to a square root power law. (Note that the time required for an individual measurement was ~ 6 seconds.)

The results of this monitoring process revealed two things: first, the number of resonances and thus amount of time required to perform an averaged measurement to achieve a given relative precision by monitoring f_+ (the results are shown in Fig. 4.28); second, a possible shift in frequency due to variations in the number of trapped ions. The possible frequency shift can be seen in the data of Fig. 4.27 where the average reduced cyclotron frequency seems to vary with the average FFT amplitude (and thus number of ions). The correlation between the average reduced cyclotron frequency measurement and the corresponding FFT amplitude is shown in Fig. 4.29. During this scan, the background pressure was not being monitored and had risen to just over 4×10^{-8} mbar by the end of the scan. It is likely that the correlation was caused by the increase in pressure and resulted in a greater number of ions being trapped.

To verify that changes in the background pressure were indeed responsible for shifting the $\langle f_+(\text{H}_3\text{O}^+) \rangle$ measurements, a pressure scan was performed using the same parameters

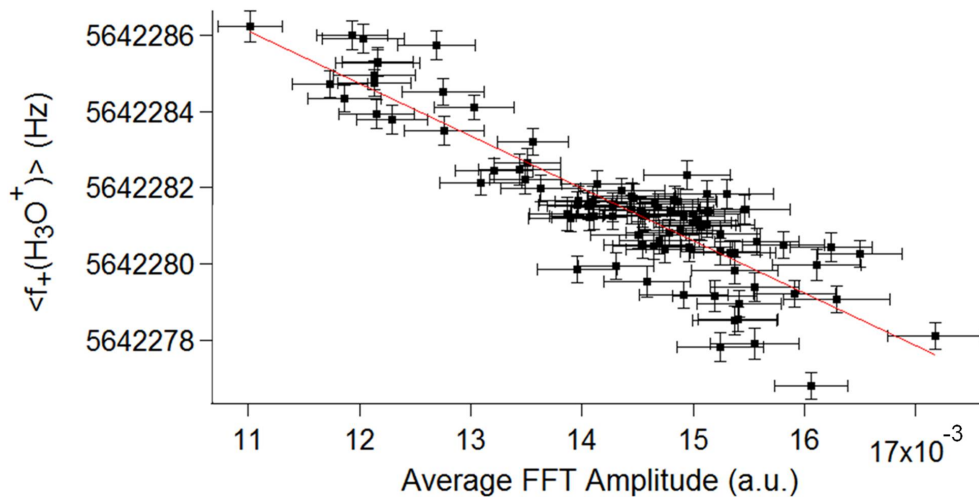


Figure 4.29: Average reduced cyclotron frequency as a function of average FFT amplitude from the f_+ monitoring process of H_3O^+ . Each data point represents one average measurement of 120 individual f_+ measurements. The solid line (red) is the best linear fit to the data and has a slope of $-1371(80)$ Hz/a.u.

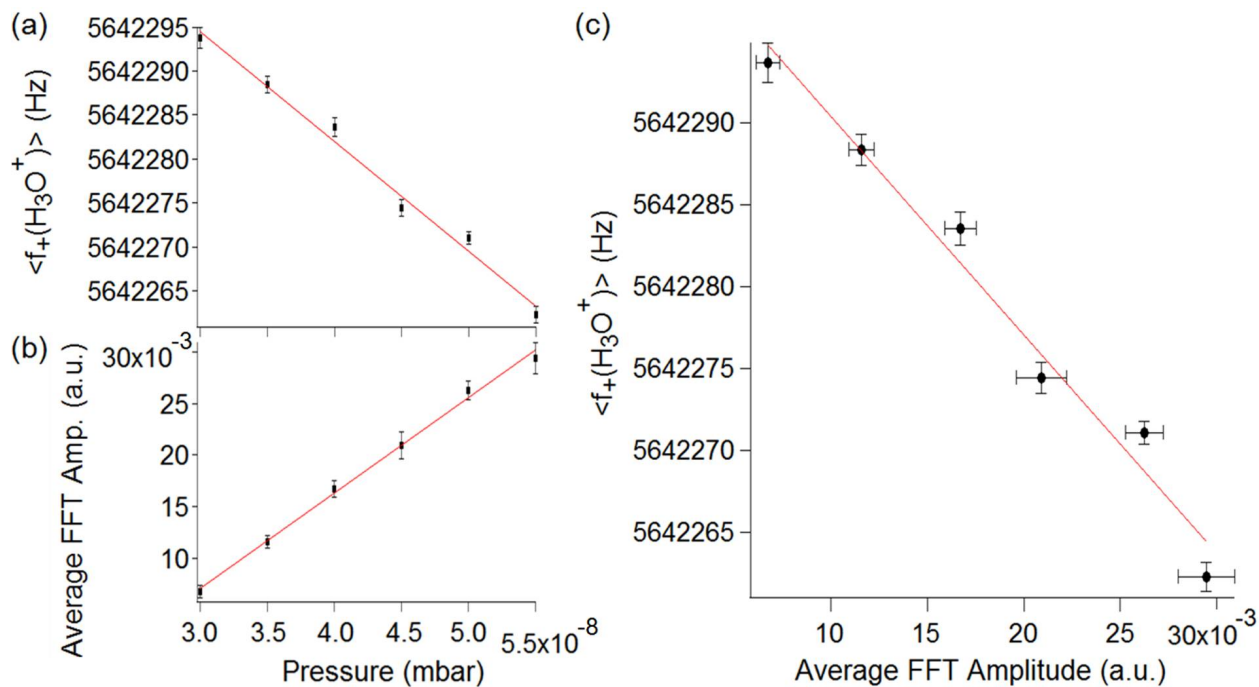


Figure 4.30: Results of the pressure scan showing (a) the average reduced cyclotron frequency of H_3O^+ and (b) the average FFT amplitude as a function of pressure, and (c) the average reduced cyclotron frequency as a function of the average FFT amplitude. Each data point represents the average of 20 individual f_+ measurements. The solid lines (red) are the best linear fits to the data. The fit results of (c) give a slope of $-1336(108)$ Hz/a.u.

as those used in the monitoring process, but the background pressure was increased from 3.0×10^{-8} mbar to 5.5×10^{-8} mbar in 0.5×10^{-8} mbar steps after every 20 measurements. The results of the pressure scan are shown in Fig. 4.30. A linear relationship between both shifts in $\langle f_+(\text{H}_3\text{O}^+) \rangle$ and the respective average FFT amplitudes was observed. More importantly, perfect agreement is seen between the slope of the fit in Fig. 4.29 and that in Fig. 4.30(c), indicating that the change in frequency observed during the f_+ monitoring process of H_3O^+ was caused by pressure fluctuations (and thus fluctuations in the number of trapped ions). With this information it is possible to correct for these shifts, however, the ideal scenario for monitoring the magnetic field should be insensitive to varying numbers of trapped ions.

4.5.2 True Cyclotron Frequency Determination

It is possible to detect not only the resonances of f_- , f_z , and f_+ , but also the $(f_+ + f_-)$ resonance which, for an ideal trap, is equal to f_c , the “true” cyclotron frequency (see Eqn. 2.5). Observation of the $(f_+ + f_-)$, or f_c , resonance, however, necessitates the implementation of the quadrupole detection scheme [60]. In this scheme, the image current is detected on two adjacent electrodes (rather than opposite electrodes in the dipole detection scheme). Exciting and detecting true cyclotron motion is advantageous since shifts in f_- and f_+ due to changes in number of ions and image charge shifts from space charge can cancel each other out [106]; also, f_c is independent of the trapping voltage. Detection of f_c has been carried out previously using FT-ICR techniques [107], and the reader is referred to this work for a more detailed description.

4.5.2.1 Quadrupole Pickup Detection Method

To pick up the image current induced by the motion of the ions at f_c , the $(f_+ + f_-)$ signal, the detection electrodes were connected in a quadrupole configuration which was easily accomplished by swapping one excitation electrode with one detection electrode. When changing to the quadrupole detection scheme, the resonant circuit was retuned, since the capacitance of the detection circuit changed. This time the detection circuit was tuned to $5.653 \text{ MHz} \approx f_c$ to maximize the amplification of the induced f_c signal.

To detect f_c , the trapped ion cloud must have some initial magnetron motion. This motion was induced by exciting the ions with a burst of RF power applied to one set of correction electrodes for $\sim 1.5 \text{ ms}$ at a frequency $\approx f_-$. (Various magnetron excitation amplitudes were investigated and optimized for different trapping potentials.) Then cyclotron motion was imparted to the ions already undergoing magnetron motion, by applying a burst of RF power to a different set of correction electrodes for $\sim 100 \mu\text{s}$ at a frequency $\approx f_+$. The cyclotron excitation amplitude was adjusted depending on the magnetron excitation amplitude and the trapping potential. Initially, both the excitation voltages and the trapping potential were adjusted manually to obtain the first f_c resonance, shown in Fig. 4.31, with the accompanying f_+ resonance. (In quadrupole detection utilizing only two adjacent electrodes, with the other two opposing electrodes grounded, both f_c and f_+ can be detected simultaneously. If all four electrodes were utilized in the quadrupole detection configuration, only the f_c resonance would have been observed [107].)

The parameter space was explored by adjusting the magnetron and cyclotron excitation amplitudes at various endcap-to-ring voltage ratios to maximize the FFT amplitude of the f_c resonance. However, optimizing for the largest f_c FFT amplitude did not seem to consistently

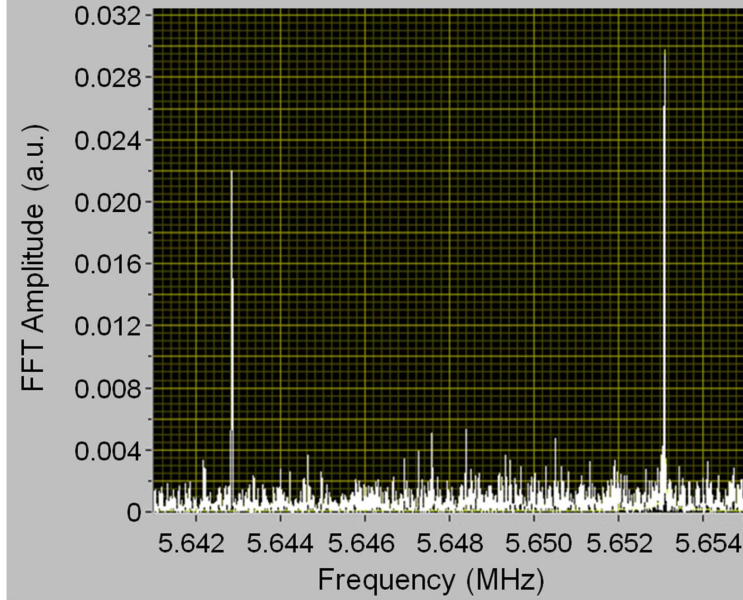


Figure 4.31: A LabVIEW screenshot of FFT resonances of both reduced cyclotron motion (left) and true cyclotron motion (right) of H_3O^+ ions in a 7.73 V potential well in the MiniTrap using the broadband FT-ICR quadrupole detection configuration.

decrease the shot-to-shot variations in f_c , i.e. didn't improve precision. In an attempt to increase precision, an automated 3-dimensional search probing for shifts in both f_c and f_+ was carried out by scanning ρ_- over a range of endcap-to-ring voltage ratios for different cyclotron excitation amplitudes. To minimize the frequency shift due to number of ions, this optimization scan was performed at a background pressure of a few 10^{-8} mbar and ionizing the background gas for 1 s with an electron beam current of ~ 0.065 nA, resulting in the fewest number of ions that could be detected with FFT resonance signal-to-noise ratios no smaller than 5.

The data from this optimization scan were analyzed to determine the best parameters that minimized shot-to-shot fluctuations while also minimizing shifts to f_+ and f_c as a function of magnetron drive amplitude. The optimum parameters are listed in Table 4.3, where it is important to recognize that the range of the optimized values lie within the precision of the function generator and the power supplies that generate the values of the respective

Table 4.3: Optimal excitation parameters identified by a 3-dimensional scan of ρ_- for a range of endcap-to-ring voltage ratios for different cyclotron excitation amplitudes. The magnetron and cyclotron excitation times and frequencies were held constant at 10.25 kHz for ~ 1.5 ms and 5.6428 MHz for ~ 100 μ s, respectively, within a potential well of 7.735 V. *A 10 dB attenuator was used to attenuate the cyclotron excitation.

Parameter	Value
Endcap	6.985 - 6.990 V
Ring	(-) 0.745 - 0.750 V
Magnetron Excitation	0.615 - 0.635 Vpp
Cyclotron Excitation	0.17 - 0.18 Vpp*

parameters. The optimized endcap-to-ring voltage ratio was ~ 1 to 0.11, in agreement with the magnetron tuning result, but larger than that from the reduced cyclotron tuning method. This discrepancy was most likely due to the increased radial extent that the ion cloud traversed as it executed the two radial normal-mode oscillations.

An electron beam current scan was performed to determine the frequency dependence on the number of ions by adjusting the current supplied to the thermionic emitter at a background pressure of a few 10^{-8} mbar (as read by the Penning gauge by the turbo pump). This scan was utilized to determine the electron beam current where frequency shifts due to a larger ion cloud begin to become non-negligible. The results are shown in Fig. 4.32, where the frequency shift due to the number of ions is shown for both f_c and f_+ . Only minimal shifts in f_c are present when using an electron beam current of ~ 0.04 nA to almost 0.085 nA, however, f_+ shifts down by ~ 10 Hz. These results clearly indicate both the acceptable operating currents (at the associated background pressure) for limiting shifts in f_c due to the number of ions and the benefits of measuring f_c instead of f_+ . Specifically, an electron beam current of ~ 0.06 nA is ideal for creating enough ions to consistently resolve frequency peaks with a signal-to-noise ratio greater than 5, while limiting the shift in f_c due to variations in the number of ions in the trap to a negligible level.

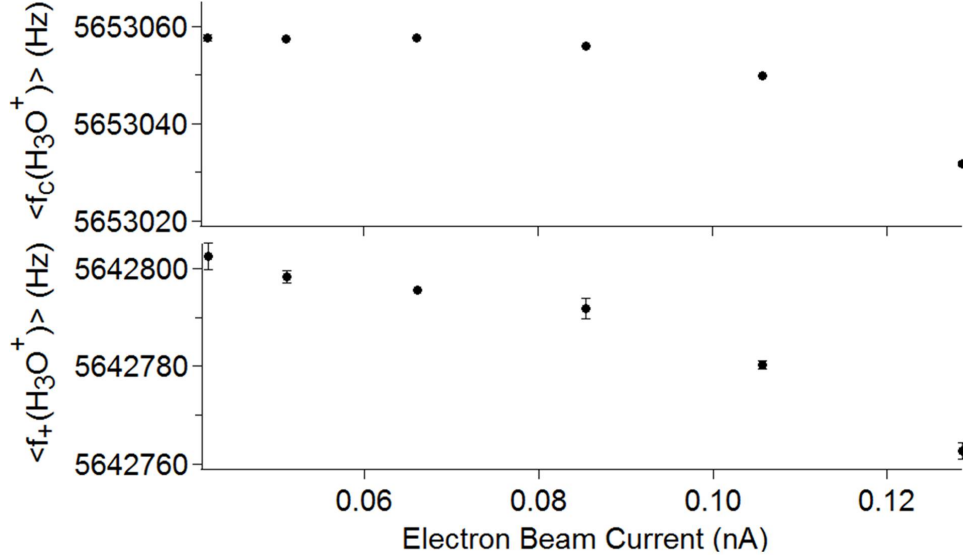


Figure 4.32: Results from the electron beam current scan of f_c and f_+ for H_3O^+ using the optimized parameters. Each data point is the average of 100 measurements where the error bars represent the standard deviation of the individual measurements (some of which cannot be resolved). (Note the difference between the frequency shift of f_c and f_+ as a function of electron beam current, especially at lower electron beam currents – the scales are equivalent).

Not only is the shift in f_c smaller than f_+ due to the number of ions, but a frequency shift to f_c due to variations in trap depth are almost eliminated. (A shift in f_c due to variations in trap depth vanish completely in a perfect trap.) A trap depth scan that monitored both f_c and f_+ was performed as the trap depth was varied from 7.631 V to 7.839 V in steps of 0.052 V, while maintaining a constant endcap-to-ring voltage ratio of ~ 1 to 0.11. The ions were excited using the optimal parameters listed in Table 4.3. The results of this scan are shown in Fig. 4.33, where f_c and f_+ were recorded simultaneously. A series expansion of Eqn. 2.3 to first order reveals a linear dependence of f_- and f_+ on the trap potential, V_o , where $\omega_- \approx V_o/(2d^2B)$ and $\omega_+ \approx \omega_c - V_o/(2d^2B)$ as is clearly displayed in the variation of $\langle f_+(\text{H}_3\text{O}^+) \rangle$ as a function of trapping potential shown in Fig. 4.33. The true cyclotron frequency, however, remains fairly constant for a change in trap depth of ~ 20 mV, whereas the reduced cyclotron frequency shifts by almost 300 Hz.

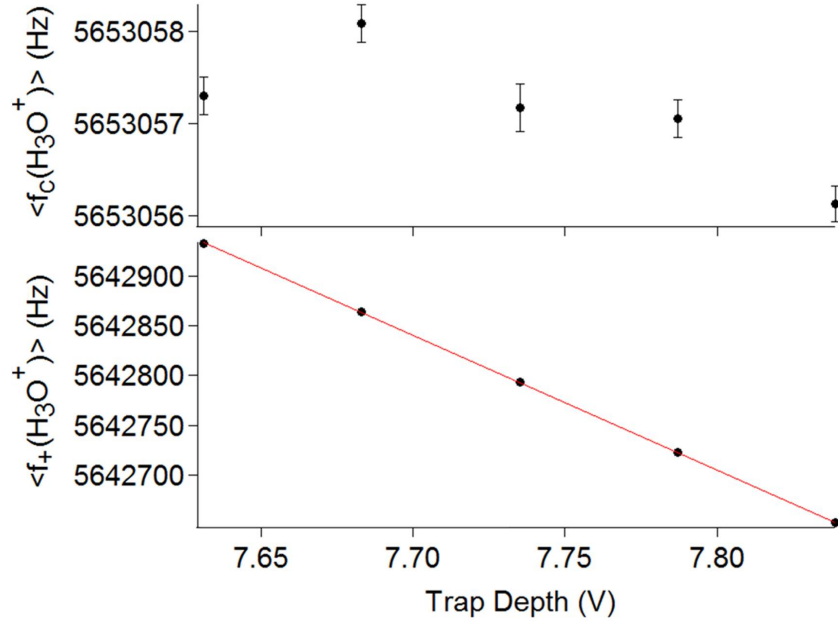


Figure 4.33: Results of the trap depth scan of f_c and f_+ of H_3O^+ . Each data point is an average of 30 measurements where the error bars represent the standard deviation of those measurements (the error bars in the plot of f_+ are too small to be resolved). The linear best fit of $\langle f_+(\text{H}_3\text{O}^+) \rangle$ as a function of trapping potential (solid red line) resulted in a slope of $-1350(3)$ Hz/V. (Note the change in vertical scales between the plot of f_c and f_+ .)

4.5.2.2 Precision of the MiniTrap Magnetometer

To probe the precision of the MiniTrap, known changes to the magnetic field were introduced. This was achieved by changing the magnetic field by a controlled amount to see if the change in the magnetic field could be resolved. The magnetic field was changed by passing a small current, of 1 to 10 mA, through the coil wrapped around the MiniTrap enclosure. A scan was set up to continuously monitor $f_+(\text{H}_3\text{O}^+)$ as a function of applied current to the coil to test the effectiveness of this method. The test consisted of ramping the current in the coil up from 2 mA to 11 mA and then back down from 11 mA to 2 mA in 1 mA steps, where 100 f_c measurements were performed at each current setting. This scan was repeated 5 times and the results are shown in Fig. 4.34.

This initial test of the precision of the magnetometer revealed that changes in the mag-

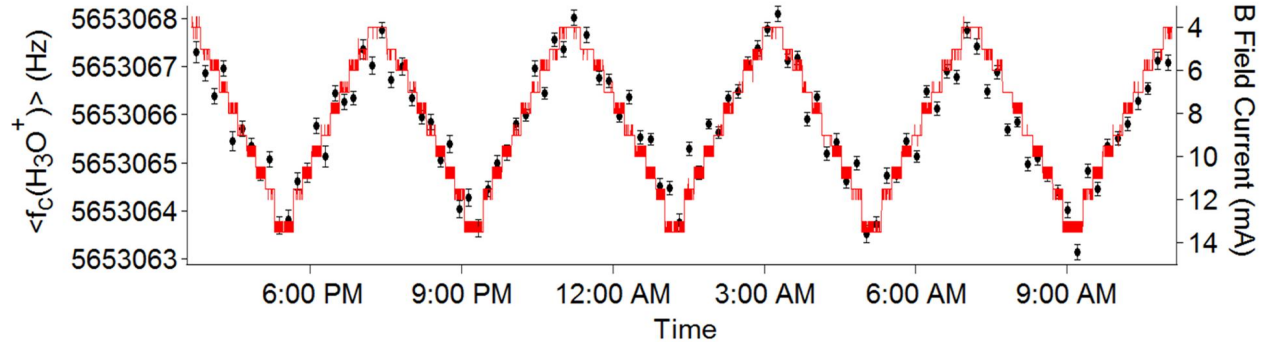


Figure 4.34: Results from the true cyclotron frequency monitoring process while ramping the current in the coil (wrapped around the MiniTrap enclosure) to produce changes in the total magnetic field. Each data point is an average of 100 measurements with the error bars representing the standard deviation of those measurements. The solid line (red) represents the variation of the current supplied by the power supply (values given on the right axis).

netic field corresponding to a relative precision of at least 10^{-7} could be achieved by averaging 100 individual f_c measurements over a period of 10 min. The resolution of this particular scan, however, was not extremely high and also neglected changes in the magnetic field during the ~ 3 hour long ramping period. To more accurately determine the precision that the MiniTrap could achieve, smaller changes in the magnetic field would have to be made. It would also be necessary to perform f_c measurements at a reference B field current after every few f_c measurements at a given B field scan current to eliminate the effects of the magnetic field changing on the few-minute time scale. (The power supply used to pass current through the coil had a precision of 0.5 mA, so a current divider circuit was installed to reduce the current by about a factor of 10 to allow for finer changes to the magnetic field.)

An alternating B field precision scan was performed to provide a more accurate test of the precision of the magnetometer. The scan consisted of operating the f_c monitoring process during which five f_c measurements were performed at a given B field reference current (for this scan 10 mA was the reference current), then five f_c measurements at a B field scan current. These 10 measurements were repeated 400 times to give 2000 f_c measurements at

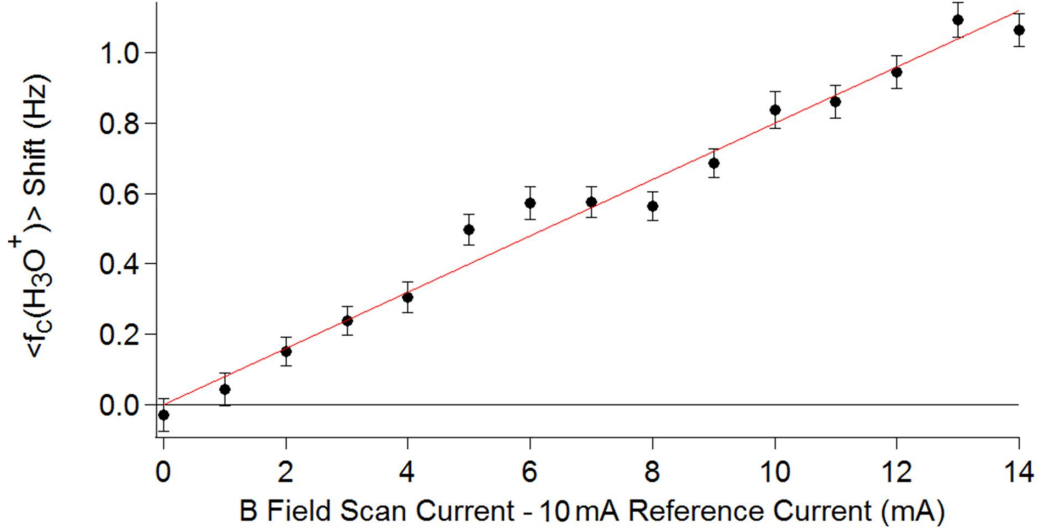


Figure 4.35: Results of the true cyclotron frequency monitor while alternating every five measurements between a B field scan current and a B field reference current of 10 mA to produce relative changes in the magnetic field. Each data point represents 4000 f_c measurements where the error bars represent the standard deviation of those measurements (see text). The solid red line is the linear best fit to the data and the solid black line is the zero-shift reference. The linear best fit resulted in a slope of 0.080(3) Hz/mA.

each B field current, resulting in a total of 4000 f_c measurements for one B field scan current setting. Data was taken for 15 different B field scan current settings in 1 mA steps, including a control setting where 4000 f_c measurements were taken at the B field reference current of 10 mA. Each set of 2000 f_c measurements were averaged and assigned an uncertainty equal to the standard deviation of those measurements divided by the square root of the number of measurements. The observed shift in $\langle f_c(\text{H}_3\text{O}^+) \rangle$ was then calculated as the difference between the average of the 2000 f_c measurements at the 10 mA reference current and the B field scan current. The uncertainty in $\langle f_c(\text{H}_3\text{O}^+) \rangle$ was calculated by adding the uncertainties of the average f_c measurements at the 10 mA reference current and the B field scan current in quadrature. The results of this analysis are presented in Figure 4.35. Note that the fit indicates that a change in the magnetic field from applying a 1 mA current (which was subsequently divided down by a factor of ~ 10) shifted f_c by 0.08 Hz.

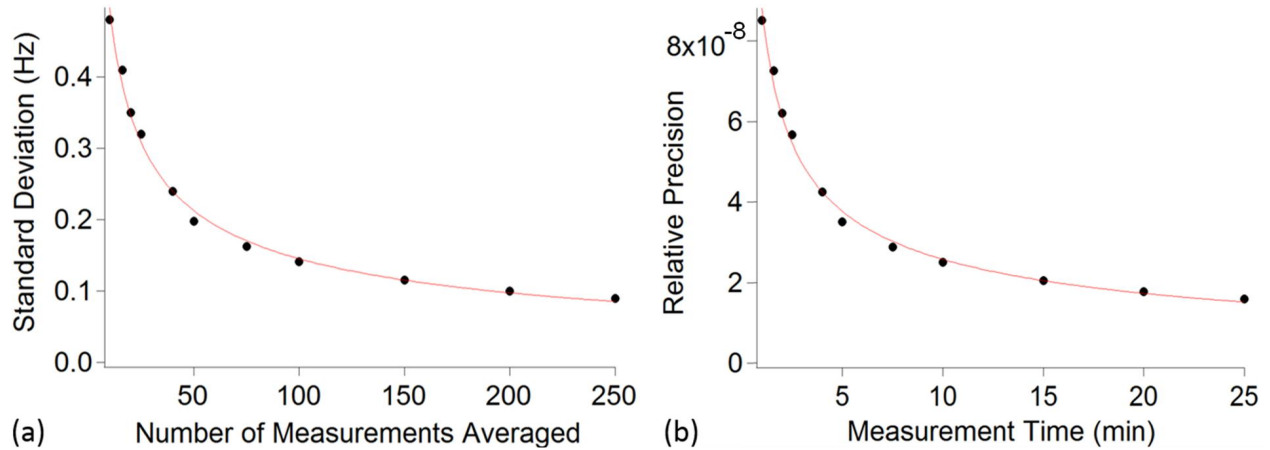


Figure 4.36: Illustration of the precision obtained from the alternating B field scan where (a) the standard deviation of the data is given when each frequency measurement was an average of a given number of measurements and (b) the measurement time necessary to achieve a given relative precision from the same data. The solid line (red) in each graph is the best fit to a square root power law fit.

The data from the alternating B field measurement was analyzed to obtain the average experimental precision for a given number of measurements averaged and for averaging measurements over a given period of time. The standard deviation was calculated for the data set when broken up into average measurements composed of various numbers of individual measurements to obtain the relative precision as a function of the number of measurements, or measurement time (the period of each individual measurement was 6 seconds). The results, shown in Fig. 4.36, indicate that a relative precision of $< 4 \times 10^{-8}$ can be achieved by averaging fifty individual measurements, or a relative precision of $< 3 \times 10^{-8}$ for one hundred measurements, or a relative precision of $< 2 \times 10^{-8}$ for two hundred measurements (all at the 1σ level). Note that this is the relative precision of an individual averaged measurement, and to obtain the uncertainty associated with the difference between two averaged values (and to obtain the corresponding uncertainties for the data shown in Fig. 4.35), the uncertainties associated with these relative precisions would need to be multiplied by $\sqrt{2}$.

The MiniTrap has thus demonstrated that it can achieve the required relative precision

but at the cost of temporal resolution. However, the six second individual measurement time was not fully optimized, and it is conceivable that individual measurement times of two seconds could be possible, which would result in both better relative precision and temporal resolution. For two second measurement times, a relative precision of $< 2 \times 10^{-8}$ could be achieved by averaging individual measurements over a period of seven minutes. However, there is another trick that one can play to further increase the relative precision of the MiniTrap that will be discussed in a following section.

4.5.2.3 Tracking the B Field Using the True Cyclotron Frequency

A long-term $\langle f_c(\text{H}_3\text{O}^+) \rangle$ monitoring process was performed to track the drift of the 7 T SIPT superconducting magnet and to verify the performance of the MiniTrap. To verify the accuracy and precision of the function generator used to apply RF power to the ions, a reference frequency from an additional function generator, at 5.648 MHz, was added on top of the signal recorded by the scope-card. The reference signal was attenuated to result in an FFT amplitude about a factor of ten larger than that of the cyclotron frequency peaks. Fig. 4.37 depicts an FFT spectrum of one individual measurement with the monitor showing the f_+ , f_{Ref} , and f_c resonances on the left, middle, and right of the spectrum, respectively. The monitoring process ran continuously for eleven days and nine hours. The results of the long-term monitoring process are shown in Fig. 4.38 where each data point represents the average of 100 individual measurements. (Analysis of the monitor data for the reference frequency signal indicated that the observed changes in the cyclotron frequency were real.)

There are two features of the results of the long-term monitoring process that require explanation. The first feature to note is the momentary increase in both f_c and f_+ that occurred just after the start of the monitor and once again near the end. These shifts in

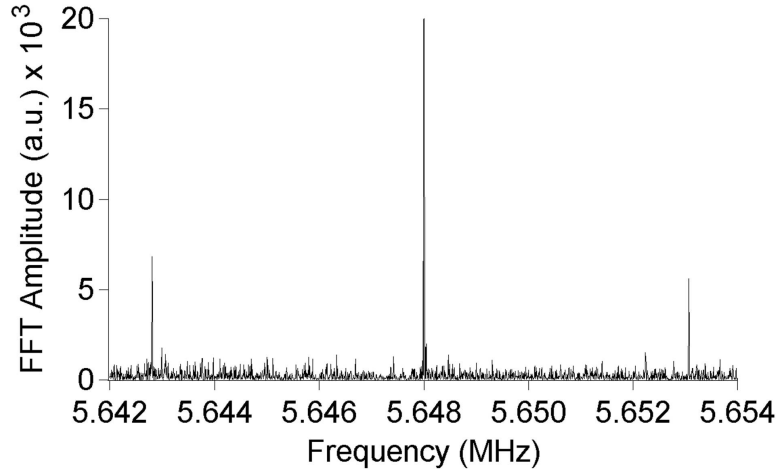


Figure 4.37: An FFT spectrum showing the resonances from the reduced cyclotron motion (left), the reference signal (middle), and the true cyclotron motion (right) from an individual measurement of H_3O^+ in the MiniTrap. (The height of the f_{Ref} resonance peak has been truncated to clearly show the f_+ and f_c resonance peaks.)

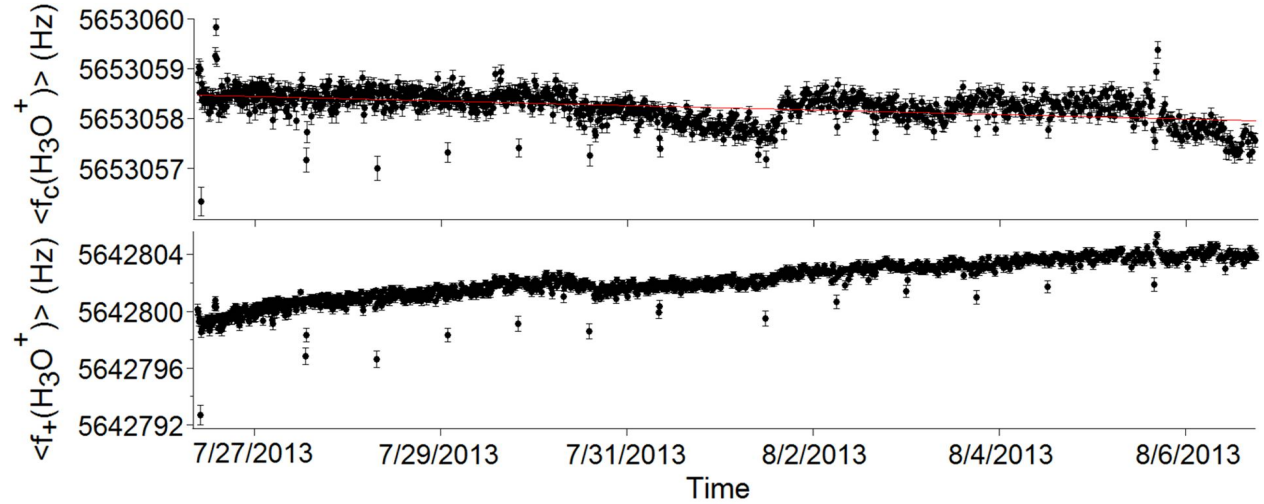


Figure 4.38: Results of the long-term MiniTrap monitoring process showing the $\langle f_c(\text{H}_3\text{O}^+) \rangle$ and associated $\langle f_+(\text{H}_3\text{O}^+) \rangle$ measurements over the course of ~ 11 days and 9 hours. Each data point is the average of 100 frequency measurements (10 minutes each) where the error bars correspond to the 1σ uncertainty associated with the distribution of those 100 measurements. The linear best fit of the f_c data (shown in red) corresponds to a magnetic field decay rate of $-3.3(2) \times 10^{-10} \text{ hr}^{-1}$. (Note that the difference in scales between the two graphs is \sim a factor of four.)

frequency occurred during the LN2 fill of the SIPT magnet and were exactly correlated with the duration of the fill. This was a good indication that the MiniTrap was functioning properly and able to track short-term changes in the magnetic field.

The second feature of the data from the long-term monitoring process is the occasional momentary negative shift in both f_c and f_+ that occurred throughout the data set, and requires further investigation. The duration of the temporary shift ranged from 5 to 15 minutes, and the extent of the shift ranged from 0.5 to 2 Hz for $\langle f_c(\text{H}_3\text{O}^+) \rangle$ and from 1 to 7 Hz for $\langle f_+(\text{H}_3\text{O}^+) \rangle$. The data was further analyzed for correlations in amplitude. No correlation could be found with respect to the FFT amplitude of $\langle f_c(\text{H}_3\text{O}^+) \rangle$, however, the decreases were associated with minor increases in the FFT amplitude of $\langle f_+(\text{H}_3\text{O}^+) \rangle$. Drifts in the FFT amplitude by the same amount throughout the monitoring process, however, did not result in changing the frequency by the amount observed during these short-term shifts.

One possible explanation for these infrequent events are momentary changes in the excitation amplitudes produced by the function generators. Another possible explanation is a momentary change in the trapping potential or number of ions produced in the trap. Verification of these scenarios would require further investigation. It is unlikely that the magnetic field was changing and that these shifts were actually caused by shifts in the magnetic field, however, verifying this scenario would require the simultaneous operation of a secondary monitoring device. It would thus be beneficial to operate both traps simultaneously with independent power supplies, function generators, and ancillary electronics. This would not only help determine the cause of the short-term systematic shifts to the true cyclotron frequency, but would also identify any systematic long-term drifts while increasing the confidence in the reliability, as well as precision, of the magnetometer.

Note the generally positive drift of $\langle f_+(\text{H}_3\text{O}^+) \rangle$ seen in Fig. 4.38. To look for correla-

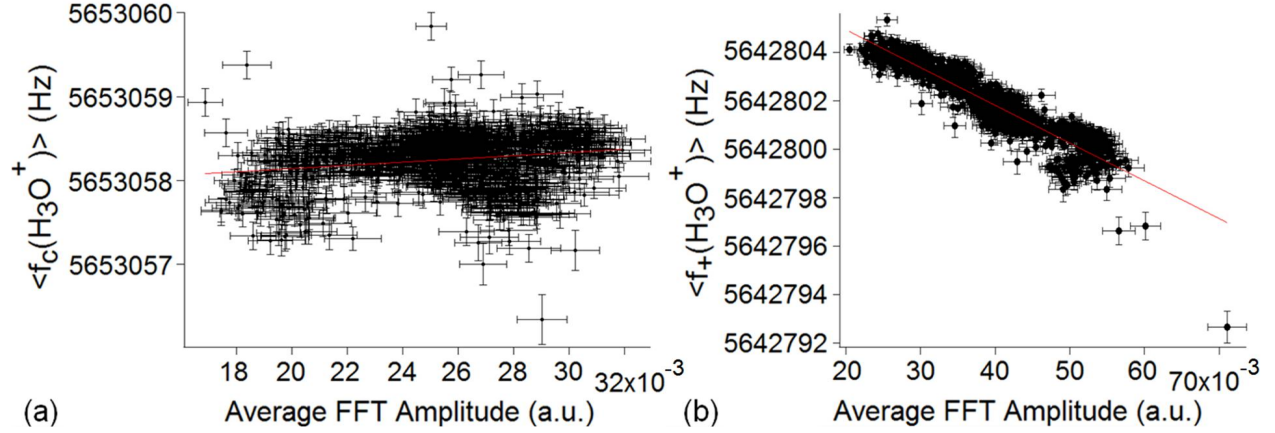


Figure 4.39: Frequency correlation with FFT amplitude from the long-term monitoring process for (a) $\langle f_c(\text{H}_3\text{O}^+) \rangle$ and (b) $\langle f_+(\text{H}_3\text{O}^+) \rangle$. Each data point represents an average of 100 individual measurements. The linear best fits to the data (solid red lines) for (a) and (b) resulted in slopes of 20(3) Hz/a.u. and -156(2) Hz/a.u., respectively.

tions, both $\langle f_c(\text{H}_3\text{O}^+) \rangle$ and $\langle f_+(\text{H}_3\text{O}^+) \rangle$ were plotted as a function of their respective amplitudes. The results are shown in Fig. 4.39, where a correlation of $\langle f_+(\text{H}_3\text{O}^+) \rangle$ with amplitude was present, indicating that the upward trend of $\langle f_+(\text{H}_3\text{O}^+) \rangle$ throughout the long-term monitoring process was the result of the number of trapped ions slowly decreasing. As expected, the dependence of $\langle f_c(\text{H}_3\text{O}^+) \rangle$ on FFT amplitude is much smaller (by an order of magnitude) than that of $\langle f_+(\text{H}_3\text{O}^+) \rangle$, and gives rise to a slope (in this range of amplitudes) corresponding to a frequency shift on the order of the precision of the MiniTrap. The extent of the scatter in the $\langle f_c(\text{H}_3\text{O}^+) \rangle$ data seen in Fig. 4.39(a) suggests that the frequency shift in f_c is either not associated with the FFT amplitude or that the shift was within the uncertainty of the measurements.

4.5.2.4 Improving the Precision of the MiniTrap

Some improvements can be made to the MiniTrap system to further increase the relative precision of the magnetometer while also improving the temporal resolution. One fairly straightforward technique was already mentioned briefly, and relies on decreasing the time

required to perform a single f_c measurement. For example, ten second cycle times were used for the tests with the LEBIT magnet which was decreased to six seconds for the tests with the SIPT magnet. For the tests in the SIPT magnet, one second ionization times were used. It may be possible to decrease the ionization time by increasing the electron beam current and produce the same number of ions. In addition, one second trap dumping times were used. This could be drastically shortened (to sub-ms) especially if carried out with a fast switch to reverse the polarity of the trapping potential. Finally, a script in the MTCS was used to control the measurement process in a step-wise procedure. The measurement routine could be completely streamlined and controlled with a single instance of a LabVIEW Field-Programmable Gate Array (FPGA) module. (For the measurement process used in the measurements in this work, the LabVIEW FPGA module was used for timing the ionization cycle and controlling the trapping electrodes, but not simultaneously.) Streamlining the measurement process would allow parallel operations of recording data and controlling voltages and currents, thus eliminating dead time during the measurement process. The measurement cycle time would then be mainly limited by electron beam ionization times plus excitation and detection times. Two second measurement times are conceivable, however, this optimization procedure was outside the scope of this project.

Another increase in precision could come from measuring a lighter mass, such as He^+ or H_2^+ , instead of H_3O^+ . This would, in principle, increase the precision of the MiniTrap by up to a factor of 10 as the frequency and its resolution are inversely proportional to mass as indicated by Eqns. 2.2 and 4.4. An improvement in precision by this amount would allow a relative precision of 10^{-8} to be reached within 10 cyclotron frequency measurements and, with optimized cycle times, in 20 seconds. However, using H_2^+ as a reference ion species to monitor changes in the magnetic field is not so trivial. This is because one

would prefer the majority of the ionized background gas to be H_2^+ , since frequency shifts due to any contaminant ions are known to occur [84]. It would be possible, though, to remove known contaminants from the trap, e.g. H_3O^+ , by exciting them to large radii with a strong dipole pulse, thus driving them out of the trap before performing a cyclotron frequency measurement of H_2^+ . Another option would be to increase the ratio of H_2 in the background gas by installing a leak valve and tube connecting the MiniTrap to a source of hydrogen outside the magnet, however, this is not an ideal situation for a variety of reasons. Alternatively, leaking in He is also possible and would provide about a factor of 5 increase in precision. Monitoring lighter ions together with shorter measurement cycle times suggests that the demonstrated relative precision by monitoring H_3O^+ is not the lower limit, and should be viewed as an upper limit to the precision obtainable by the MiniTrap.

4.5.3 Summary of Results

The test of electron beam production in the LEBIT magnet demonstrated the ability to ionize the residual gas using electron-impact ionization. This test also indicated the feasibility of performing FT-ICR cyclotron frequency measurements of a reference ion to obtain a relative precision of the change in the magnetic field at the level of 1 part in 10^8 . The analytical and numerical simulations performed identified the optimal trap geometry parameters to maximize the precision of the MiniTrap. The MiniTrap was successfully fabricated and assembled with minimal difficulties. Finally, tests in the 7 T superconducting SIPT magnet demonstrated that the MiniTrap could detect changes in strong magnetic fields with a relative precision of nearly 1 part in 10^8 , with a temporal resolution of ~ 30 minutes, by monitoring the cyclotron frequency of H_3O^+ . A threefold increase in temporal resolution should be relatively easy to achieve by streamlining the measurement process. In addition, the overall

precision of the MiniTrap could be increased by a factor of 5 to 10 by monitoring the cyclotron frequency of lighter masses such as H_2^+ or He^+ .

Chapter 5

Summary and Outlook

The current efforts to perform next-generation experiments to discover $0\nu\beta\beta$ decay highlights the importance of neutrino physics and the implications that such a discovery would have, such as leading to new physics beyond the Standard Model. Even if $0\nu\beta\beta$ decay is not observed at the limits of sensitivity strived for by these experiments, the nature of the neutrino will have been further constrained and would further contribute to the success of the Standard Model.

In light of the current efforts to build a next-generation experiment, SuperNEMO, and future experiments to discover $0\nu\beta\beta$ decay by observing ^{82}Se , the first direct $\beta\beta$ decay Q -value measurement of ^{82}Se was performed. This measurement was necessary to not only precisely determine the energy of the single peak in the electron sum-energy spectrum with an uncertainty below the keV level, but also to improve the accuracy in the estimation of the half-life sensitivity required to detect a given effective neutrino mass, or conversely, to improve the precision of the effective neutrino mass if the half-life is measured.

The direct $Q_{\beta\beta}$ measurement of ^{82}Se was performed at the LEBIT facility using the TOF-ICR technique to determine the cyclotron frequency ratio between $^{82}\text{Se}^+$ and $^{82}\text{Kr}^+$ ions.

The measured ratio resulted in a $\beta\beta$ decay Q -value of $Q_{\beta\beta} = 2997.9(3)$ keV, which is nearly an order of magnitude more precise than the previous literature value [75] and is sufficient for locating the $0\nu\beta\beta$ decay peak in future experiments utilizing large mass bolometers. In addition, the uncertainty in the half-life or the effective neutrino mass due to a Q -value of this precision is negligible compared to the uncertainty in the NME. By calculating an improved PSF, using a NME from a corrected shell model calculation [73], and the current upper limits for the effective neutrino mass from the EXO-200 experiment [87], a lower limit range for the ^{82}Se $0\nu\beta\beta$ decay half-life of 5.0×10^{24} - 3.7×10^{25} years was obtained. This indicates that if SuperNEMO is able to achieve its projected sensitivity, an effective neutrino mass as low as 60-85 meV could be detected and may allow identification of the neutrino mass hierarchy.

To enhance the high-precision mass measurement program at the LEBIT facility, a miniature Penning trap magnetometer has been developed to increase precision and maximize scientific output with increased efficiency by continuously monitoring the drift of the LEBIT facility's 9.4 T superconducting magnet. The development of the MiniTrap magnetometer resulted in the successful development of FEP production methods and the demonstration of the FT-ICR technique in the LEBIT magnet. After carefully optimizing the dimensions of a miniature Penning trap for detecting light ions using the FT-ICR technique, the MiniTrap was successfully designed, fabricated, and assembled. Finally, the stand-alone high-precision MiniTrap magnetometer was tested in the 7 T superconducting SIPT magnet. The results of monitoring the true cyclotron frequency of H_3O^+ indicated that the desired relative precision in the change of the magnetic field on the order of 1 part in 10^8 was achieved.

The next step is to install the MiniTrap in the LEBIT facility's 9.4 T superconducting magnet to monitor short-term fluctuations in the magnetic field during rare isotope mea-

surements. In addition, improvements can be made to improve temporal resolution and increase the MiniTrap's absolute precision. Finally, the MiniTrap could be redesigned and repackaged to monitor drifts in other magnets with strong magnetic fields to high precision or for applications where high-level ionizing radiation prevents the use of conventional NMR probes.

APPENDICES

Appendix A

MiniTrap Electronics

A National Instruments (NI) Peripheral component interconnect eXtensions for Instrumentation (PXI), model PXI-1042, was the main hub for communicating between the components of the MTCS composed of LabVIEW programming software and all of the electronic devices needed to control the MiniTrap. The PXI-1042 was equipped with a NI PXI-4110 power supply, NI PXI-5114 scope card, NI-6229 Data AcQuisition (DAQ) card, NI PXI-7811R FPGA timing module, a NI PXI General Purpose Interface Bus (GPIB) controller, and a NI PXI-8336 interface to directly communicate with a server Personal Computer (PC) through a fiber optic link. Other electronics utilized for the MiniTrap include: NF Corporation (NF) SA-420F5 low noise Field-Effect Transistor (FET) differential amplifier with a 15 V Direct Current (DC) power supply, Symmetricom 8040 rubidium frequency standard, Tektronix Arbitrary Function Generator (AFG) 3252 dual channel arbitrary function generator, Agilent 33500B waveform generator, Keithley 6485 picoammeter, B&K Precision 9123A single output programmable DC power supply, GwInstek PSM-2010 programmable power supply, Stanford Research Systems (SRS) PS350 high-voltage (HV) power supply, Keithley 2000-20 multimeter, custom-made bipolar switching power supply, custom-made phase splitter,

custom-made RF switch, custom-made filters, and attenuators.

The National Instruments (NI) PXI-1042 was equipped with a NI PXI-4110 power supply, a NI PXI-5114 scope card, a NI-6229 DAQ card, a NI PXI-7811R FPGA timing module, and a NI PXI-GPIB controller. The NI PXI-4110 power supply was controlled by the MTCS and was used to set the ring and endcap voltages. Due to high-frequency noise from the electronics, the voltages were filtered through a DC low-pass filter before being routed to the MiniTrap.

The NI PXI-5114 scope card recorded the output from the NF SA-420F5 low noise FET differential amplifier after high-frequency noise was attenuated using a low-pass filter. The scope card required a frequency reference (supplied by a Symmetricom 8040 rubidium frequency standard), because the internal onboard clock was observed to shift by several Hz with single degree temperature fluctuations.

The -10 V to +10 V analog outputs of the NI-6229 DAQ card were used to provide scaled voltages for setting the FEP/thermionic emitter bias voltage, the electron beam energy set voltage, the electron beam blocking voltage, and the FEP extraction voltage. The analog inputs of the NI-6229 DAQ card were used to monitor the FEP/thermionic emitter bias voltage, the electron beam energy set voltage, and the electron beam current output from the Keithley 6485 picoammeter.

A NI PXI-7811R FPGA timing module was used to provide Transistor-Transistor Logic (TTL) signals that were used to time events during a cyclotron frequency measurement such as triggering the function generator, switching the electron beam blocking voltage, and triggering an RF switch to block leakage signals from the AFG when applying a sweep excitation. Reconfiguring the FPGA timing generator would be the key to streamlining the entire measurement process by triggering each measurement operation with a single FPGA

routine in the MTCS. (The outputs from the timing card were first buffered through line drivers composed of op-amps before supplying the TLL voltages to the respective devices.)

Finally, the NI PXI-GPIB controller allowed communication with all devices equipped with a GPIB interface and included the function generators, Keithley 6485 picoammeter, B&K Precision and GwInstek power supplies, and the SRS HV power supply. This communication was critical to allow the MTCS to control each device remotely.

The NF SA-420F5 low noise FET differential amplifier was used to amplify the signal from the secondary pickup coil of the FT-ICR detection circuit. To avoid high-frequency background noise from being mixed down into the frequency range of interest, the signal passed through a low-pass filter before being delivered to the NI PXI-5114 scope card. (In the case of H_3O^+ , a 10 MHz low-pass filter was used). A bandpass filter could be installed which would also attenuate low-frequency noise to eliminate higher order harmonics, however, this was not an issue when detecting $f_c(\text{H}_3\text{O}^+)$. The NF SA-420F5 low-noise FET differential amplifier was powered by a 15 V DC power supply built by the NSCL electronics shop.

A Tektronix AFG 3252 dual channel arbitrary function generator was used to provide the excitation signals that were directly routed to the excitation electrodes of the MiniTrap. During a cyclotron frequency measurement the Tektronix AFG 3252 was triggered by the FPGA timing module and the trigger delay times were set accordingly for each channel to provide excitations from both channels at arbitrary times. Conveniently, all of the functions can be controlled via the MTCS through GPIB communication. In addition to providing a reference clock to the PXI-5114 scope card, the Tektronix AFG 3252, as well as the Agilent 33500B were also locked to the 10 MHz signal from the Symmetricom 8040 rubidium frequency standard. The Agilent 33500B waveform generator was used to provide the reference signal to verify that the devices were all locked during cyclotron frequency measurements.

The electron beam current was measured by directly connecting the MiniTrap Faraday plate to the Keithley 6485 picoammeter. The picoammeter was controlled via GPIB and can also record the current through GPIB as well. However, when implementing the PID loop (needed to stabilize the electron beam current from FEPs) the GPIB current readback was too slow. When using the PID loop, the 0 to 2 V analog output was used to provide a scaled electron beam current to an analog input of the NI-6229 DAQ card which allowed the electron beam current to be recorded at a much faster rate.

The B&K Precision 9123A single output programmable DC power supply provided the current necessary to power the thermionic emitter. The power supply was completely controlled by the MTCS via GPIB and was usually operated in constant current mode. To bias the emitter, a bias voltage was applied to the positive output of the B&K Precision 9123A power supply while the ground output of both power supplies were connected together. This allowed for the energy of the electron beam to be defined with respect to the common ground of the system. A shielded (and grounded) cable was used to route the wires to the power feedthrough located on the 6-way conflat cross.

For testing the precision of the MiniTrap in the SIPT magnet, the magnetic field needed to be varied and was accomplished by supplying a current by the GwInstek PSM-2010 programmable power supply to a coil wrapped around the MiniTrap enclosure. Again, this power supply was completely controlled by the MTCS via GPIB. This power supply could also be used to provide the current necessary to heat the NEG pump that could potentially be installed in the MiniTrap.

To operate FEPs, high voltages needed to be applied to the electron beam extraction electrode. This potential was created by a Stanford Research Systems (SRS) PS350 high-voltage (HV) power supply. The SRS HV power supply provided voltages up to 5 kV and

was controlled remotely via GPIB. This power supply was only used when creating an electron beam from an FEP and during the FT-ICR test in the LEBIT magnet. When using thermionic emitters this power supply was not utilized and instead the first electron beam extraction electrode was grounded.

The Keithley 2000-20 multimeter was used to measure the ambient room temperature by measuring the resistance of a thermistor attached to the bore of the SIPT magnet. A cold cathode penning gauge together with an MKS pressure controller was used to monitor the pressure in the bore of the SIPT magnet and was recorded by the LEBIT control system. Monitoring the background pressure together with the ambient room temperature is important to determine if there were any correlations to changes in the cyclotron frequency.

Many custom-made electronics were utilized in the MiniTrap setup. First, the LEBIT bipolar switching power supply was implemented to provide two independent outputs capable of supplying between -120 V and $+120\text{ V}$. Each channel had three separate set voltages that were internally set to accept between -10 V to $+10\text{ V}$, and would correspond to an output voltage scaled by a factor of 12. Two TTL inputs were used to select one of the three set voltages referenced to determine the output voltage. One channel of this power supply was used to provide the bias voltage for thermionic emitter and was never switched. The second channel supplied the voltage to the electron beam blocking electrode and switched between two different voltages to either block the electron beam or allow it to pass. The switching of the second channel was performed by supplying a TTL signal from the timing generator.

A custom-made RF phase splitter was implemented to produce two signals, 180 degrees out of phase, from a single output from a function generator. This was accomplished quite simply through a set of RF inverting op-amp circuits with a gain equal to 1. The phase splitter was used to provide dipole excitation when the dipole detection configuration of FT-

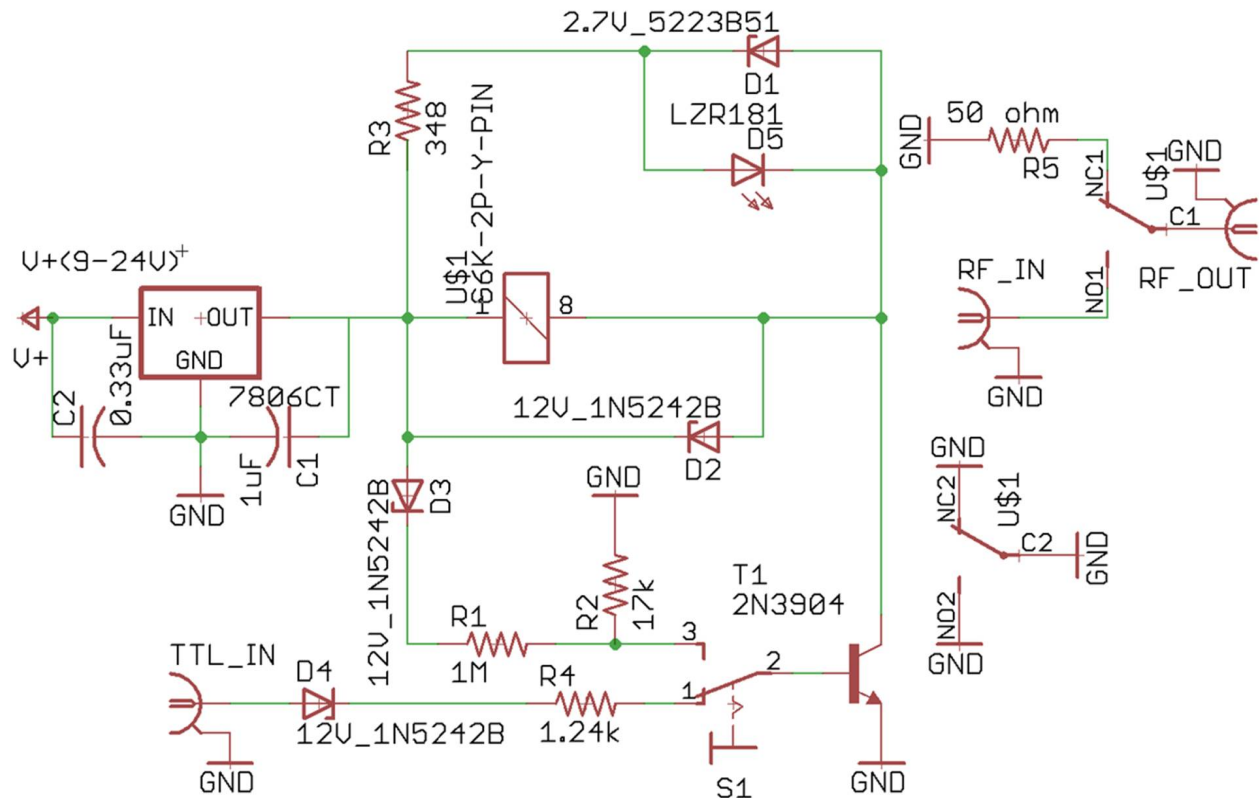


Figure A.1: Schematic of the RF switch used to eliminate leakage output from the function generator.

ICR was used (in the FT-ICR quadrupole detection configuration, the phase splitter was not utilized).

When using the sweep excitation to excite magnetron and axial motion, the AFG output a small leakage signal at the stop frequency defined by the sweep range. To eliminate the leakage signal an RF switch was built to that was triggered by a TTL signal (provided by the FPGA timing module) to block the signal during a cyclotron frequency measurement. The schematic of the switch is shown in Fig. A.1. The switch operated on the basis of an NPN transistor switch that controlled an RF relay. The RF switch was powered by a DC power supply of 9 to 24 V. The RF switch had three modes which were selected via switch, S1: on mode, off mode, or automatic mode. When in either on mode or auto mode and the TTL is high, the RF switch allowed the RF input to be transmitted to the output and the

Light-Emitting Diode (LED) indicator light was on. When the switch, S1, was off or when the TTL was low in auto mode, the relay grounds the RF output and the LED indicator light was off. The RF switch could be easily modified and reproduced to allow switching between two different voltages of a power supply and could be controlled remotely from the FPGA timing generator to help streamline the measurement process, for example to eject ions from the trap.

MiniCircuits attenuators were used for various reasons throughout the MiniTrap experiment, but in the end only one 10 dB attenuator was used to attenuate the reduced cyclotron excitation signal from the AFG. However, various other passive filters were custom built, such as low-pass filters and band-pass filters, which were all designed using Almost All Digital Electronics (AADE) Filter Design and Analysis software.

Appendix B

MiniTrap Control System

The MTCS was developed in LabVIEW as a means to completely control all of the MiniTrap electronics remotely and to automate the cyclotron frequency measurement process. The front panel of the MTCS is shown in Fig. B.1. The first set of tabs on in the upper left portion of the MTCS front panel provided the basic set-up and addressing of each device. The graphing tabs allowed the depiction of the acquired signal to be viewed in either the time domain or frequency domain. A fitting procedure programmed in LabView located and produced the best Lorentzian fit to a peak and recorded the fit data. The excitation and acquisition control tabs were located just below the graphing tabs. Here the type of excitation could be chosen and the relevant parameters could be adjusted. Finally, there were a set of tabs on the right portion of the MTCS front panel and include the Frequencies and Voltages tab, the FEP (Manual Mode) tab, FEP PID tab, W thermal emitter tab, Data Save Settings tab, Script tab, Script Array tab, and the FFT Data tab.

The Frequencies and Voltages tab also includes the three sub-tabs (the Voltages, e-beam Bias/Blocker, and Getter Pump tabs). In this tab the excitation modes, frequencies, and amplitudes, the trap voltages, the electron beam bias and extraction voltages, electron beam

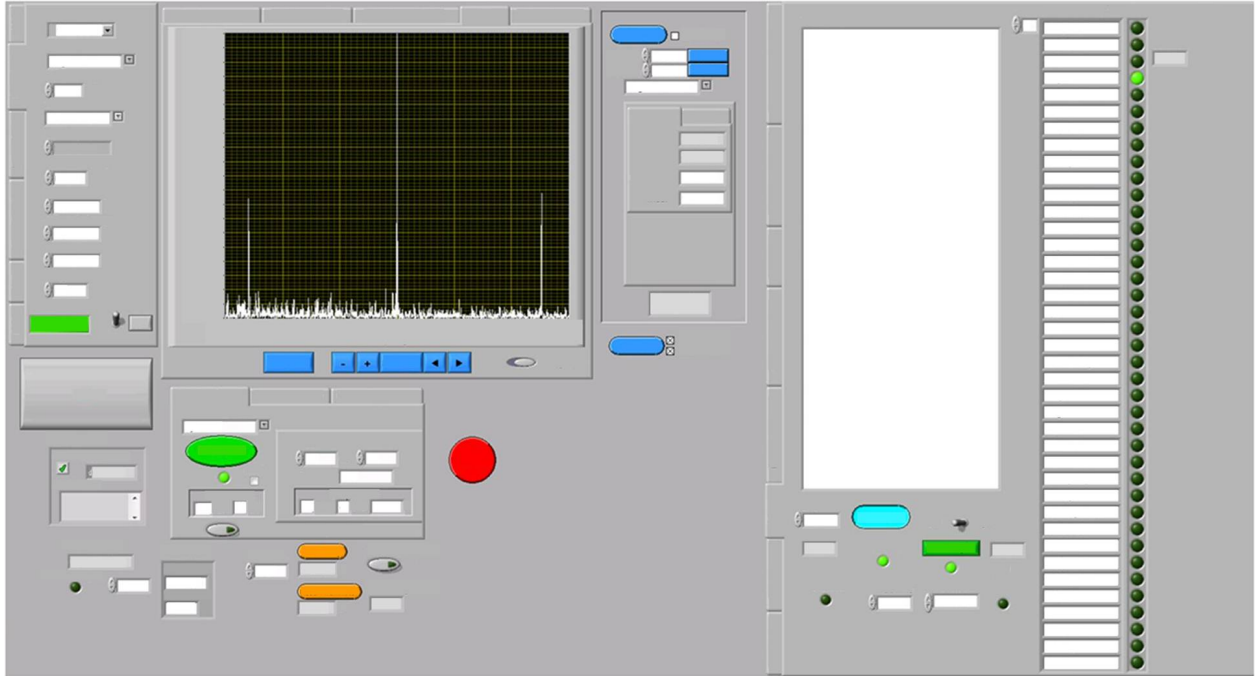


Figure B.1: Screenshot of the MiniTrap control system (MTCS) front panel (with text removed to conform to thesis submission guidelines).

ionization times, and finally the getter pump power supply can all be controlled. (The getter pump power supply was actually used to control the current passing through the coil wound around the MiniTrap enclosure to cause small changes in the strength of the magnetic field.) The three tabs directly under the Frequencies and Voltages tab were responsible for controlling the electron beam current. The two basic modes for operating the electron beam were the constant applied current mode and the conditioning mode. The constant applied current mode was used when the emitted electron beam current was stable and the current that passed through the emitter was held constant (or extraction voltage is held constant in the case of an FEP). In conditioning mode the MTCS adjusted the applied current (or voltage) to maintain the electron beam current within a specified range. The FEP PID tab also included a PID loop that could be activated to maintain a constant electron beam current when ionizing the residual gas. (The PID loop was not implemented for the thermal

emitter because the stability of the current did not necessitate the use of the PID loop.)

The Data Save Settings tab, directly under the three electron beam control tabs, was where the location of a respective data set could be saved. This tab was necessary because the MTCS allowed all of the relevant data to be recorded and saved in an appropriate file in a specified folder. The MTCS was able to save all FEP electron beam current data, all relevant cyclotron measurement parameters, each FFT resonance, and all power supply monitor data. The MTCS was set up to save the data in a dated folder created by the program, and the user had the capability to change the individual file names to which the data was saved.

One of the most important tabs was the Script tab, directly under the Data Save Settings tab, and was where the automation of the measurement process was handled. The script language was programmed from scratch in LabVIEW and required that the script start with the "Begin" command and finish with the "End" command. There was also a "Repeat" command that allowed a certain portion of the script to be repeated a given number of times. The command array was filled with many different commands that executed various functions and set various values. The commands could be programmed by the user, however, most of the possible commands that would ever be needed had already been created. The user could also step through various values by adding "(Array1)" or "(Step1)" to any command which sets a numerical value, such as a voltage or frequency, to automate scans of various parameters. The values listed in the Script Array tab would then be called upon as indexed by the scan number in the script. (Note that if nested repeats are utilized with the array or step command, the "ZeroScanNum" command must be called upon first to reset the scan number back to 0.) An example of a script string used to control a continuous monitoring process of ten thousand cyclotron frequency measurements of $f_c(\text{H}_3\text{O}^+)$ is given in Table B.1.

Table B.1: An example of a script string used in the Script tab of the MTCS to control a continuous monitoring process of ten thousand cyclotron frequency measurements of $f_c(\text{H}_3\text{O}^+)$.

```

*Begin
UpdateFileName()
AutoFitPeak(Off)
AutoSave(On)
SaveFFT(On)
SaveEBeamData(Off)
ThermalEmitter(Off)
FireTime(1000)
//
SetOutput1(On)
SetFreq1(5642800)
SetAmp1(0.625)
ModeChan1(Burst)
UpdateChan1()
SetOutput2(On)
SetAmp2(0.175)
SetFreq2(10250)
UpdateChan2()
Conditioning(Off)
Blocker(On)
//
Ring(0.745)
ECap(6.990)
@Top1
Trap(Open)
ReadTemp()
Wait(0.7)
Trap(Set)
Wait(0.1)
FireEBeam
Wait(1.3)
Acquire()
Repeat(Top1,10000;10000)
//
Trap(Open)
Blocker(On)
Conditioning(Off)
AutoFitPeak(Off)
AutoSave(Off)
SaveFFT(Off)
SaveEBeamData(Off)
End

```

Finally, the FFT Data tab recorded and graphed in real time the fit results of each cyclotron frequency measurement. This tab was very useful to observe short-term trends in the cyclotron frequency when scanning parameters by hand. For long-term measurements, this function tended to increase the cycle time of the MTCS, therefore, a switch in the Script tab could turn the graphing function on or off, and was generally left in the off position except for short-term scans and monitoring processes.

The MTCS went through many revisions and was the end result of much development work, however, there is much room for improvement. First of all, if FEPs will no longer be used, the FEP tabs should be eliminated. Also the scripting array should be modified and incorporated into a single FPGA timing routine to streamline the measurement process. This would require some development work, but by decreasing the cycle time of a cyclotron frequency measurement the precision of the MiniTrap could be increased and its temporal resolution could be improved.

BIBLIOGRAPHY

BIBLIOGRAPHY

- [1] T. Otto *et al.*, Nucl. Phys. A **567**, 281 (1994).
- [2] F. Herfurth *et al.*, J. Phys. B - At. Mol. Opt. **36**, 391 (2003).
- [3] C. Guénaut *et al.*, Phys. Rev. C **75**, 044303 (2007).
- [4] M. Smith *et al.*, Phys. Rev. Lett. **101**, 202501 (2008).
- [5] M. Brodeur *et al.*, Phys. Rev. Lett. **108**, 052504 (2012).
- [6] H. Schatz, Int. J. Mass Spectrom., **251**, 293 (2006).
- [7] C. Weber *et al.*, Phys. Rev. C **78**, 054310 (2008).
- [8] E. Haettner *et al.*, Phys. Rev. Lett. **106**, 122501 (2011).
- [9] K. Blaum, G. Audi, D. Beck, B. Bollen, F. Herfurth, A. Kellerbauer, H.-J. Kluge, E. Sauvan, and S. Schwarz, Phys. Rev. Lett. **91**, 260801 (2003).
- [10] S. Ettenauer *et al.*, Phys. Rev. C **81**, 024313 (2010).
- [11] G. Savard *et al.*, Nucl. Phys. A **654**, 961c (1999).
- [12] S. Rainville *et al.*, Nature **438**, 1096 (2005).
- [13] R. Schuch, I. Bergström, K. Blaum, T. Fritioff, Sz. Nagy, A. Solders, M. Suhonen, Hyperfine Interact. **173**, 73 (2006).
- [14] G. Bollen *et al.*, Phys. Rev. Lett. **96**, 152501 (2006).
- [15] R. Ringle *et al.*, Phys. Rev. C **75**, 055503 (2007).
- [16] D. Lunney, J. M. Pearson, and C. Thibault, Rev. Mod. Phys. **75**, 1021 (2003).

- [17] L. M. Brown, *Physics Today*, September, 23 (1978).
- [18] C. L. Cowan, Jr., R. Reines, F. B. Harrison, H. W. Kruse, and A. D. McGuire, *Science* **124**, 3212 (1956).
- [19] S. Abe *et al.* (KamLAND Collaboration), *Phys. Rev. Lett.* **100**, 221803 (2008).
- [20] P. Adamson *et al.* (MINOS Collaboration), *Phys. Rev. Lett.* **101**, 131802 (2008).
- [21] B. Aharmim *et al.* (SNO Collaboration), *Phys. Rev. C* **81**, 055504 (2010).
- [22] F. T. Avignone, III, S. R. Elliott, and J. Engel, *Rev. Mod. Phys.* **80**, 481 (2008).
- [23] D. Fink *et al.*, *Phys. Rev. Lett.* **108**, 062502 (2012).
- [24] G. Douysset, T. Fritioff, and C. Carlberg, *Phys. Rev. Lett.* **86**, 19 (2001).
- [25] S. Rahaman *et al.*, *Phys. Lett. B* **662**, 111 (2008).
- [26] B. J. Mount, M. Redshaw, and E. G. Myers, *Phys. Rev. C* **81**, 032501(R) (2010).
- [27] C. Smorra *et al.*, *Phys. Rev. C* **85**, 027601 (2012).
- [28] S. Rahaman *et al.*, *Phys. Lett. B* **703**, 412 (2011).
- [29] N. D. Scielzo *et al.*, *Phys. Rev. C* **80**, 025501 (2009).
- [30] M. Redshaw, B. J. Mount, E. G. Myers, and F. T. Avignone III, *Phys. Rev. Lett.* **102**, 212502 (2009).
- [31] M. Redshaw, E. Wingfield, J. McDaniel, and E. G. Myers, *Phys. Rev. Lett.* **98**, 053003 (2007).
- [32] V. S. Kolhinen *et al.*, *Phys. Lett. B* **697**, 116 (2011).
- [33] V. S. Kolhinen *et al.*, *Phys. Rev. C* **82**, 022501(R) (2010).
- [34] M. Block *et al.*, *Phys. Rev. Lett.* **100**, 132501 (2008).

- [35] R. Ferrer *et al.*, Phys. Rev. C **81**, 044318 (2010).
- [36] A. A. Kwiatkowski *et al.*, Phys. Rev. C **80**, 051302(R) (2009).
- [37] A. A. Kwiatkowski, submitted to Int. J. Mass Spectrom.
- [38] M. Redshaw, G. Bollen, S. Bustabad, A. A. Kwiatkowski, D. L. Lincoln, S. J. Novario, R. Ringle, S. Schwarz, and A. A. Valverde, Nucl. Instrum. Meth. B, in press.
- [39] D. J. Morrissey, B. M. Sherrill, M. Steiner, *et al.*, Nucl. Instr. and Meth. B, 204:90 (2003).
- [40] H. Weick, H. Geissel, C. Scheidenberger, *et al.*. Nucl. Instr. and Meth. B, 164-165:168 (2000).
- [41] L. Weissman, D. A. Davies, P. A. Lofy, and D. J. Morrissey, Nucl. Instr. and Meth. A, 531:416 (2004).
- [42] S. Schwarz, G. Bollen, D. Lawton, A. Neudert, R. Ringle, P. Schury, and T. Sun, Nucl. Instrum. Meth. B **204**, 474 (2003).
- [43] P. Schury *et al.*, Phys. Rev. C **75**, 055801, (2007).
- [44] J. Savory *et al.*, Phys. Rev. Lett. **102**, 132501 (2009).
- [45] S. Naimi *et al.*, Phys. Rev. C **86**, 014325 (2012).
- [46] M. Redshaw, G. Bollen, M. Brodeur, S. Bustabad, D. L. Lincoln, S. J. Novario, R. Ringle, and S. Schwarz, Phys. Rev. C **86**, 041306(R) (2012).
- [47] S. Bustabad, G. Bollen, M. Brodeur, D. L. Lincoln, S. J. Novario, M. Redshaw, R. Ringle, and S. Schwarz, Phys. Rev. C **88**, 035502 (2013).
- [48] S. Bustabad, G. Bollen, M. Brodeur, D. L. Lincoln, S. J. Novario, M. Redshaw, R. Ringle, S. Schwarz, and A. A. Valverde, Phys. Rev. C **88**, 022501(R) (2013).
- [49] S. Novario *et al.*, in preparation.
- [50] T. Sun, Ph.D. thesis, Michigan State University (2006).

- [51] M. Thoennessen, Nucl. Phys. A **834**, 688c (2010).
- [52] T. Sun, S. Schwarz, G. Bollen, D. Lawton, R. Ringle, and P. Schury, Eur. Phys. J. A **25**, s01, 61-62 (2005).
- [53] G. Gabrielse and J. Tan. J. Appl. Phys., **63**, 5143 (1988).
- [54] G. Bollen, S. Schwarz, D. Davies, P. Lofy, D. Morrissey, R. Ringle, P. Schury, T. Sun, and L. Weissman, Nucl. Instr. and Meth. A, 532:203 (2004).
- [55] H. G. Dehmelt. Advan. At. Mol. Phys., 3:53 (1967).
- [56] P. Schury, Ph.D. thesis, Michigan State University (2007).
- [57] J. Savory, Ph.D. thesis, Michigan State University (2009).
- [58] R. Ringle, Ph.D. thesis, Michigans State University (2006).
- [59] R. Ringle *et al.*, Int. J. Mass Spectrom., **251**, 300 (2006).
- [60] G. Bollen, R. B. Moore, G. Savard, and H. Stolzenberg, J. Appl. Phys. **68**, 4355 (1990).
- [61] M. König, G. Bollen, H.-J. Kluge, T. Otto, and J. Szerypo, Int. J. Mass Spectrom. Ion Processes **142**, 95 (1995).
- [62] R. Ringle, G. Bollen, A. Prinke, J. Savory, P. Schury, S. Schwarz, and T. Sun, Int. J. Mass Spectrom. **263**, 38 (2007).
- [63] G. Gräff, H. Kalinowsky, and J. Traut, Z. Phys. A **297**, 35 (1980).
- [64] P. McIntyre, Y. Wu, G. Liang, C. Meitzler, IEEE Trans. Appl. Supercond., **5**, 238 (1995).
- [65] R. Ringle, G. Bollen, A. Prinke, J. Savory, P. Schury, S. Schwarz, and T. Sun, Nucl. Instrum. Meth. A **604**, 536 (2009).
- [66] R.S. VanDyck Jr., D. L. Farnham, S. L. Zafonte, P. B. Schwinberg, Rev. Sci. Instr., **70**, 1665 (1999).
- [67] S. R. Elliott, A. A. Hahn, and M. K. Moe, Phys. Rev. Lett. **59**, 2020 (1987).

- [68] A. S. Barabash, Phys. At. Nucl. **73**, 162 (2010).
- [69] N. Ackerman *et al.* (EXO Collaboration), Phys. Rev. Lett. **107**, 212501 (2011).
- [70] H. V. Klapdor-Kleingrothaus, A. Dietz, H. L. Harney, and I. V. Krivosheina, Mod. Phys. Lett. A **16**, 2409 (2001).
- [71] A. S. Barabash, Phys. Part. Nuclei **42**, 613 (2011).
- [72] R. Saakyan (NEMO3 and SuperNEMO Collaborations), J. Phys. Conf. Ser. **179**, 012006 (2009).
- [73] D. L. Lincoln, J. D. Holt, G. Bollen, M. Brodeur, S. Bustabad, J. Engel, S. J. Novario, M. Redshaw, R. Ringle, and S. Schwarz, Phys. Rev. Lett **110**, 012501 (2013).
- [74] D. A. Nesterenko *et al.*, Phys. Rev. C **86**, 044313 (2012).
- [75] G. Audi, A. H. Wapstra, and C. Thibault, Nucl. Phys. A **729**, 337 (2003).
- [76] J. N. Nxumalo, J. G. Hykawy, P. P. Unger, C. A. Lander, R. C. Barber, K. S. Sharma, and H. E. Duckworth, Phys. Lett. B **302**, 13 (1993).
- [77] R. J. Ellis, R. C. Barber, G. R. Dyck, B. J. Hall, K. S. Sharma, C. A. Lander, and H. E. Duckworth, Nucl. Phys. A **435**, 34 (1985).
- [78] J. D. Zumbro, A. A. Rollefson, R. W. Tarara, and C. P. Browne, Phys. Rev. C **26**, 2668 (1982).
- [79] F. Herfurth *et al.*, Eur. Phys. J. A **15**, 17 (2002).
- [80] R. C. Waddell and E. N. Jensen, Phys. Rev. **102**, 816 (1956).
- [81] J. W. Beeman *et al.*, J. Instrum. **8**, P05021 (2013).
- [82] P. Schury, G. Bollen, M. Block, D. J. Morrissey, R. Ringle, A. Prinke, J. Savory, S. Schwarz, and T. Sun, Hyperfine Interact. **173**, 165 (2006).
- [83] M. Brodeur *et al.*, Int. J. Mass Spectrom. **310**, 20 (2012).

- [84] G. Bollen, H.-J. Kluge, M. König, T. Otto, G. Savard, H. Stolzenberg, R. B. Moore, G. Rouleau, G. Audi, (ISOLDE Collaboration), *Phys. Rev. C* **46**, R2140 (1992).
- [85] R.T. Birge, *Phys. Rev.* **40**, 207 (1932).
- [86] J. Suhonen and O. Civitarese, *Phys. Rep.* **300**, 123 (1998).
- [87] M. Auger *et al.* (EXO Collaboration), *Phys. Rev. Lett.* **109**, 032505 (2012).
- [88] A. G. Marshall, C. L. Hendrickson, and G. S. Jackson, *Mass Spectrom. Rev.* **17**, 1 (1998).
- [89] X. Xiang, P. B. Grosshans, and A. G. Marshall, *Int. J. Mass Spectrom. Ion Processes* **125**, 33 (1993).
- [90] J. Repp, Diploma thesis, Johannes Gutenberg-Universität Mainz (2008).
- [91] R. O. Jenkins, *Rep. Prog. Phys.* **9**, 177 (1942).
- [92] A. J. Melmed, *J. Vac. Sci. Technol. B* **9**, 601 (1991).
- [93] M. Klein and G. Schwitzgebel, *Rev. Sci. Instrum.* **68**, 3099 (1997).
- [94] S. Kerfriden, A. H. Nahlé, S. A. Campbell, F. C. Walsh, and J. R. Smith, *Electrochimica Acta*, **43**, 1939 (1998).
- [95] H. Lemke, T. Göddenhenrich, H. P. Bochem, U. Hartmann, and C. Heiden, *Rev. Sci. Instrum.* **61**, 2538 (1990).
- [96] J. P. Song, N. H. Pryds, K. Glejbøl, K. A. Mørch, A. R. Thölén, and L. N. Christensen, *Rev. Sci. Instrum.* **64**, 900 (1993).
- [97] M. Redshaw, D. L. Lincoln, A. Benjamin, G. Bollen, R. Ferrer, R. Ringle, S. Schwarz, and A. Valdez, in preparation.
- [98] G. Bollen, S. Becker, H.-J. Kluge, M. König, R. B. Moore, T. Otto, H. Raimbault-Hartmann, G. Savard, L. Schweikhard, H. Stolzenberg, (ISOLDE Collaboration), *Nucl. Instr. and Meth. A*, **368**, 675 (1996).

- [99] S. Guan and A. G. Marshall, *Int. J. Mass Spectrom. Ion Processes* **146/147**, 261 (1995).
- [100] G. Gabrielse F. C. Mackintosh, *Int. J. Mass Spectrom. Ion Processes* **57**, 1 (1984).
- [101] G. Gabrielse, L. Haarsma, and S. L. Rolston, *Int. J. Mass Spectrom. Ion Processes* **88**, 319 (1989).
- [102] J. Ketter, T. Eronen, M. Höcker, M. Schuh, S. Streubel, K. Blaum, arXiv:1310.4463.
- [103] S. Rainville, Ph.D. thesis, Massachusetts Institute of Technology, (2003).
- [104] M. Redshaw, Ph.D. thesis, Florida State University, (2008).
- [105] P. R. Bevington and D. K. Robinson, *Data Reduction and Error Analysis for the Physical Sciences* (McGraw-Hill, New York, 2003), 3rd Edition.
- [106] J. B. Jeffries, S. E. Barlow, and G. H. Dunn, *Int. J. Mass Spectrom. Ion Processes* **54**, 169 (1983).
- [107] L. Schweikhard, M. Lindinger, and H.-J. Kluge, *Int. J. Mass Spectrom. Ion Processes* **98**, 25 (1990).